Sede Amministrativa: Università degli Studi di Padova

Dipartimento di: INGEGNERIA DELL'INFORMAZIONE (DEI)

_____

SCUOLA DI DOTTORATO DI RICERCA IN: INGEGNERIA DELL'INFORMAZIONE

INDIRIZZO: SCIENZA E TECNOLOGIA DELL'INFORMAZIONE

CICLO: XXVII

CHARACTERIZATION OF PLASMONIC SURFACES FOR SENSING APPLICATIONS

Direttore della Scuola: Ch.mo Prof. Matteo Bertocco

Coordinatore d'indirizzo: Ch.mo Prof. Carlo Ferrari

Supervisore: Ch.mo Prof. Alessandro Paccagnella

Dottorando: Mauro Perino

"From a long view of the history of mankind - seen from, say, ten thousand years from now - there can be little doubt that the most significant event of the 19th century will be judged as Maxwell's discovery of the laws of electrodynamics. The American Civil War will pale into provincial insignificance in comparison with this important scientific event of the same decade"

Richard Phillips Feynman

Table of Contents:

Abstract (italiano)

Durante il mio periodo di dottorato in Scienza e Tecnologia dell'Informazione l'attività di ricerca principale è stata focalizzata sulla caratterizzazione, simulativa e sperimentale, dei plasmoni di superficie.

I plasmoni di superficie sono onde elettromagnetiche evanescenti che si propagano all'interfaccia tra un mezzo metallico ed un mezzo dielettrico. Il loro vettore d'onda è più elevato rispetto a quello della luce nel mezzo dielettrico. Per poter quindi generare l'eccitazione si devono utilizzare particolari tecniche di accoppiamento. I due metodi più diffusi sono l'accoppiamento Kretschmann e l'accoppiamento tramite reticolo.

Una volta raggiunte le condizioni di accoppiamento dei plasmoni di superficie, si realizza il fenomeno della risonanza plasmonica, la quale si manifesta attraverso brusche variazioni nelle componenti della luce riflessa o trasmessa dalla superficie. Tipicamente si può registrare un minimo della riflettanza in funzione dell'angolo di incidenza della luce sulla superficie. Esistono, tuttavia, anche altre modalità per registrare e misurare queste risonanze, come ad esempio monitorando intensità, polarizzazione o fase della luce trasmessa e riflessa dalla superficie, in funzione della sua lunghezza d'onda o dei sui angoli di incidenza.

Le variazioni chimico/fisiche che avvengono all'interfaccia metallo/dielettrico, modificando la costante di accoppiamento plasmonica, cambiano le condizioni di risonanza. Nel caso in cui le variazioni all'interfaccia siano dovute ad un processo di riconoscimento molecolare è possibile rilevare le molecole d'interesse valutando i cambiamenti della risonanza plasmonica, fornendo così l'opportunità per l'implementazione di sensori specifici.

L'attività di dottorato è stata focalizzata innanzitutto sullo studio teorico del comportamento della risonanza plasmonica, utilizzando varie tecniche di simulazione numerica: il metodo RCWA (Rigorous Coupled Wave Analysis), Il metodo di Chandezon ed il metodo agli elementi finiti, implementato tramite Comsol v3.5.

Ho poi affrontato lo studio, tramite simulazioni, delle risonanze di superficie in configurazione Kretschmann, sia per interfacce metallo/dielettrico piane sia per interfacce nano-strutturate. Considerando una configurazione conica, ho simulato le risonanze di superficie per nano-strutture reticolari e per nano-strutture bi-dimensionali periodiche. Inoltre ho analizzato il legame tra le modalità di accoppiamento grating e Kretschmann.

Tramite queste simulazioni mi è stato possibile valutare e studiare la sensibilità delle varie risonanze plasmoniche alla variazione di indice di rifrazione, quando essa avviene all'interfaccia metallo/dielettrico. È stato così possibile identificare un nuovo parametro per descrivere la risonanza plasmonica e la sua sensibilità, ossia l'angolo azimutale, definito come l'angolo tra il vettore del grating ed il piano di scattering della luce. Considerando questo particolare angolo, la sensibilità del sensore può essere controllata con un'opportuna regolazione degli altri parametri coinvolti nell'eccitazione plasmonica, consentendole di raggiungere valori molto elevati.

Successivamente, grazie all'utilizzo di due banchi, uno per la configurazione Kretschmann ed uno per la misura di reticoli nano-strutturati in configurazione conica, ho realizzato delle campagne

di misure sperimentali. E' stato così possibile confrontare i risultati sperimentali con le simulazioni numeriche per le seguenti condizioni:

- Interfaccia piana, configurazione Kretschmann
- reticolo nano-strutturato, configurazione Kretschmann
- reticolo nano-strutturato, configurazione conica

L'attività sperimentale si è particolarmente focalizzata sul reticolo nano-strutturato, sia per l'innovativa modalità di caratterizzazione delle sue risonanze plasmoniche (valutazione del segnale trasmesso in funzione dell'angolo di incidenza e dell'angolo azimutale), sia per l'elevata sensibilità ottenuta valutando la variazione dell'angolo azimutale. La caratterizzazione è stata effettuata sia per il reticolo esposto all'aria che per il reticolo immerso in un liquido (tipicamente acqua).

Per poter verificare il comportamento della sensibilità azimutale ho variato l'indice di rifrazione del liquido in contatto con la superficie utilizzando soluzioni miste di acqua e glicerolo. Inoltre, tramite tecniche di funzionalizzazione della superficie, ovvero applicando delle molecole thiolate che vengono adsorbite sulla parte metallica dell'interfaccia, mi è stato possibile variare le costanti di accoppiamento plasmonico, in modo da verificare la capacità del dispositivo di rilevare l'avvenuta creazione di uno strato molecolare sulla superficie. Inoltre ho positivamente verificato la capacità di immobilizzare uno strato di anticorpi sulla superficie plasmonica.

Tutte le misure sperimentali che ho svolto in questa tesi sono state effettuate su sensori con superfici piane o nano-strutturate prodotte dallo spin-off universitario Next Step Engineering, con il quale ho collaborato durante il percorso di ricerca.

Abstract (English)

My research activity during the Ph. D. period has been focused on the simulation and the experimental characterization of Surface Plasmon Polaritons (SPP).

Surface Plasmon Polaritons are evanescent electromagnetic waves that propagate along a metal/dielectric interface. Since their excitation momentum is higher than that of the photons inside the dielectric medium, they cannot be excited just by lighting the interface, but they need some particular coupling configurations. Among all the possible configurations the Kretschmann and the grating are those largely widespread.

When the SPP coupling conditions are reached, abrupt changes of some components of the light reflected or transmitted at the metal/dielectric interface appear. Usually this resonances are characterized by a minimum of the reflectance acquired as a function of the incident angle or light wavelength. Several experimental methods are available to detect these SPP resonances, for instance by monitoring the light intensity, its polarization or its phase.

Changes in the physical conditions of the metal/dielectric interface produce some changes of the SPP coupling constant, and consequently a shift in the resonance position. If these changes

derive from a molecular detection process, it is possible to correlate the presence of the target molecules to the resonance variations, thus obtaining a dedicated SPP sensor.

I focused the first part of my Ph.D. activity on the simulation of SPP resonances by using several numerical techniques, such as the Rigorous Coupled Wave Analysis method, the Chandezon method, and the Finite Element Method implemented through Comsol v3.5.

I simulated the SPP resonance in the Kretschmann coupling configuration for plane and nano-grating structured metal/dielectric interfaces. Afterward, I calculated the SPP resonance behaviour for grating and bi-dimensional periodic structures lighted in the conical configuration. Furthermore, I analysed the correlations between the grating coupling method and the Kretschamann coupling method.

Through all these simulations, I studied the sensitivity of the different SPP resonances to the refractive index variation of the dielectric in contact with the metal. In this way, I was able to find a new parameter suitable for describing the SPP resonance, i.e., the azimuthal angle. By considering this particular angle, the sensitivity of the SPP resonances could be properly set according to the experimental needs and, even more important, noticeably increased to high values.

Experimentally I used two opto-electronic benches, one for the Kretschmann configuration and one for the conical mounting configuration. I have performed experimental measurements, in order to compare the experimental data with the simulations. In particular the following conditions were tested:

- Plane interface, Kretschmann configuration
- Nanostructured grating, Kretschmann configuration
- Nanostructured grating, Conical configuration

I focused my attention on the nano-structured grating in conical mounting configuration. I found an innovative way to characterize its SPP resonances, by measuring the transmitted signal as a function of the incident and azimuthal angles. The transmittance and the azimuthal sensitivities were characterized with the gratings in both air and water.

In order to study the experimental azimuthal sensitivity, I changed the liquid refractive index in contact with the grating by using different water/glycerol solutions. Moreover, I functionalized the surface by using thiolated molecules that form Self Assembled Monolayer onto the metallic layer. In this way, I was able to change the SPP coupling constants and detect the corresponding azimuthal resonance shifts. I also detected the immobilization of an antibody layer onto the metallic surface of the plasmonic interface.

All the devices I used in the experimental measurements were produced by the University spin off Next Step Engineering.

Introduction

In the last three decades we witness to a growing interest in the biosensor field since methods for fast accurate and reliable detection of analytes, such as biological molecules, pathogens, toxins, and chemicals, are highly desired especially for applications such as medical diagnostic, drug discovery, food safety and environmental monitoring.

Among all the possible sensors types, one attracts more interest, i.e. the affinity sensor. This sensor is characterized by the presence of a molecular recognition element, which is able to selectively bind a target analyte, affecting the sensors output. Affinity sensor could be based on different transducing principles. They could be summarized in electrochemical, piezoelectric, fluorescence, and optical sensors.

Among the optical transducing techniques, Surface Plasmon Resonance (SPR) achieved, over the years, a growing use and interest. This technique exploits the excitation of Surface Plasmon Polaritons (SPP) which are charge density waves travelling along a metal/dielectric interface. The electric field associated with these waves decays exponentially in the direction perpendicular to the propagation one. Most of the energy is then confined to the metal surface which explains the remarkable sensitivity of SPR to changes in optical parameters at the metal/dielectric interface.

Even if the early pioneering works on the SPP excitation through the Total Internal Reflection (TIR) method dates back to the '60s, and the first applications to gas sensing and organic monolayer assemblies detection appears between the '70s and '80s, the interest in this research field is still considerably high and involves different groups all around the world. The main features currently under improvement regard three main themes: reaching high throughput analysis, enhancing the method sensitivity, and simplifying the SPP coupling scheme.

Since the SPPs momentum is greater than the light one in the dielectric medium, it is not possible to excite them by simply lighting the metal/dielectric interface. In order to overcome this problem different coupling configurations techniques were developed over the years. The most used one is the Kretschmann configuration, where the light passes through an high refraction index prism increasing in this way its incident momentum and allowing its coupling with the SPPs. A similar method where the increasing in the light momentum is performed taking advantage of an high refractive index medium is the waveguide one. The last main method is called Grating Coupling SPR (GCSPR). In this configuration the difference between SPP momentum and the light one is provide by exploiting the grating periodic momentum.

Even if the fabrication of a nanostructured surface is more challenging respect to the fabrication of a flat surface required in the Kretschmann configurations, GCSPR configuration has one more degrees of freedom i.e. the azimuthal angle (ϕ). ϕ is defined as the angle between the light scattering plane and the grating momentum.

In this work we will analyse, by means of simulations, how ϕ affects the SPR excitation in one-dimensional and two-dimensional periodic structures. Then by using a silver unidimensional

grating, provided by Next Step Engineering s.r.l., we will prove that the sensitivity of the method could be enhanced by a factor of 20 respect to the Kretschmann configuration. We will also consider the Figure of Merit (FOM) of this detection method and we will compare it to the Kretschmann one.

The work is organized as follow:

Chapter 1 Surface Plasmon Polaritons. First we derive the expression for the SPP momentum by using the Maxwell's equations, supposing that the electromagnetic wave is confined at the metal/dielectric interface and propagates along the surface. Then we analyse the SPP polarization mode, propagation length, and its penetration depth. Furthermore we illustrate what happens to these parameters if different metals are used in the interface. Then we introduce the Kretschmann and the Grating coupling configuration methods. Finally we describe the main feature of a SPR sensing system; we illustrate the main analyte detection method and some applications of these technologies.

Chapter 2 Surface Simulation methods. In this chapter we depict three different simulation methods that could be used to simulate the light diffracted by a periodical structured surface. The first method we describe is the Rigorous Coupled Wave Analysis (RCWA). The second one is the differential or Chandezon Method (CM). The last one is the Finite Element Method (FEM) implemented through *Comsol Multiphysics®* version 3.5a. We use these methods to calculate the diffraction efficiencies of a unidimensional grating in conical mounting configuration with null azimuthal angle. The simulation results will be compared as well as the pros and cons of the methods. Finally we generalize the simpler vector model method in order to apply it to the calculations of the resonance in the two dimensional case.

Chapter 3 Simulation Results. In this chapter the grating total transmittance T_{tot} and zero order reflectance R_0 for the grating in conical mounting configuration will be simulated through the RCWA method. Moreover we perform the same study by using bidimensional periodic structures simulated through the FEM method. In both cases the resonances we found are well reproduced by the vector model calculations. After this we simulate the response of a flat and nanostructured surface lighted in the Kretschmann configurations. We also depict the link between the Kretschmann and grating configuration when the SPP are excited. Finally the sensitivity for both configurations are extensively studied through RCWA method. For the Kretschmann configuration we analyse the incident angle and wavelength sensitivity meanwhile for the grating configuration we also analyse the polarization and the azimuthal angle sensitivity. Finally we describe in detail this new sensing method i.e. the azimuthal one, and we notice that the sensitivity enhancement obtained is due to an almost parabolic shape of the plasmonic resonance.

Chapter 4 Experimental Results. In this chapter we describe the optical benches we used to evaluate the SPR in grating and Kretschmann configurations and a brief description of the developed software will be reported. After this we show our experimental results regarding the characterization of the Grating transmittance. We also report the order zero reflectance in the Kretschmann configurations we found by using flat and unidimensional grating surfaces. Then we characterize the sensitivity and FOM of the azimuthal detection method by changing the buffer refractive index. We achieve this goals by using a custom microfluidic cell where different

glycerol/water solutions were flushed. We also check the ability of the method to detect the presence of Self Assmbled Monlayer (SAM) of different thickness and we monitor the adsorption kinetic of these molecules onto the silver metal surface. Finally, we compare the resonance shifts caused by the immobilization of an antibody layer onto the silver flat and nanostructured surfaces. The flat one are evaluated in the Kretschmann configurations meanwhile the nanostructured one are measured by using the azimuthal method.

1 Surface Plasmon Polaritons

The first observation of Surface Plasmon Polaritons was performed by Wood [1] in 1902, who reported anomalies in the spectrum of light diffracted on a metallic diffraction grating. But only in 1941 Fano [2] proved that these anomalies are associated with the excitation of electromagnetic surface waves on the surface of the diffraction grating. Later, in 1968, the work of Otto [3] demonstrated that the drop in reflectivity in the attenuated total reflection method is due to the excitation of SPPs. In the same year, Kretschmann and Raether [4] observed excitation of SPPs in another configuration of the attenuated total reflection method. These pioneering works established a convenient method for the excitation and investigation of SPP, before modern nanofabrication technique allowed nanostructured gratings realization.

The first application of the SPR as a sensing tool was performed in 1974 by Reather. He monitored the surface roughness of thin films [5].A few years later in 1977 Gordon detect a SPR shift induced by the formation of an organic monolayer films onto the metallic layer [6]. Later in 1980, the group headed by Lundstrom reported the detection of gaseous analyte and biomolecules and stared the new era of this label free techniques [7], [8]. Starting from these pioneering works, a lot of studies have been done in order to improve both the excitation and detection method of the plasmonic resonance as well as its sensitivity, resolution, and reliability. Thanks to all these efforts SPR sensors are currently used in the analytical chemistry, material science and biological fields. The great impact of this field is also attested by several reviews and books [9]–[17] that describe the advance in the SPR sensor as well as the existence of commercial instruments already available since the early '90s [18], [19].

In this chapter we will describe the main features of SPP starting from Maxwell's equations. We will derive the SPP dispersion law, which shows the typical non radiative character of these surface waves. The evanescent nature of SPPs will be then highlighted together with their surface propagation characteristics. We will then describe how to excite SPP by means of light. Finally we will introduce some basic features of a biosensor device.

1.1   Theory of Surface Plasmon Polaritons

In order to achieve the condition for the SPP wave excitation we can start from Maxwell's equations in a continuous media without charge or current sources [15]:

$$\nabla \boldsymbol{D} = 0 \tag{1.1}$$

$$\nabla \times \boldsymbol{E} = -\frac{\partial \boldsymbol{B}}{\partial t} \tag{1.2}$$

$$\nabla \boldsymbol{B} = 0 \tag{1.3}$$

$$\nabla \times \boldsymbol{H} = \frac{\partial \boldsymbol{D}}{\partial t} \tag{1.4}$$

We considered also these constitutive relations:

$$\boldsymbol{D} = \varepsilon(\boldsymbol{r})\boldsymbol{E} \tag{1.5}$$

$$\boldsymbol{B} = \mu(\boldsymbol{r})\boldsymbol{H} \tag{1.6}$$

where $\varepsilon(\boldsymbol{r}) = \varepsilon_0\,\varepsilon(\boldsymbol{r})$ and, $\mu(\boldsymbol{r}) = \mu_0\,\mu(\boldsymbol{r})$, ε, μ are respectively the relative dielectric permittivity and the relative magnetic permeability of the medium meanwhile ε_0, μ_0 refers to

their values in vacuum, respectively. In this specific case, since we are interested in study time harmonic wave propagation, the fields can be written as follow:

$$E(x, y, z, t) = E(x, y, z)e^{-i\omega t} \quad (1.7)$$
$$H(x, y, z, t) = H(x, y, z)e^{-i\omega t} \quad (1.8)$$

For simplicity and practical purposes (since we will use Silver as metal) we will consider only non-magnetic material. This implies that $\mu = 1$ in all our domains.

Taking the curl of (1.2) and using (1.4) and (1.2) we obtain this equation:

$$\nabla^2 E - \varepsilon(r)\mu \frac{\partial^2 E}{\partial t^2} = \nabla \left(-\frac{1}{\varepsilon(r)} E \cdot \nabla \varepsilon(r) \right) \quad (1.9)$$

In a similar way, for the magnetic field:

$$\nabla^2 H - \varepsilon(r)\mu \frac{\partial^2 H}{\partial t^2} = (\nabla \times H) \times \left(\frac{\nabla \varepsilon(r)}{\varepsilon(r)} \right) \quad (1.10)$$
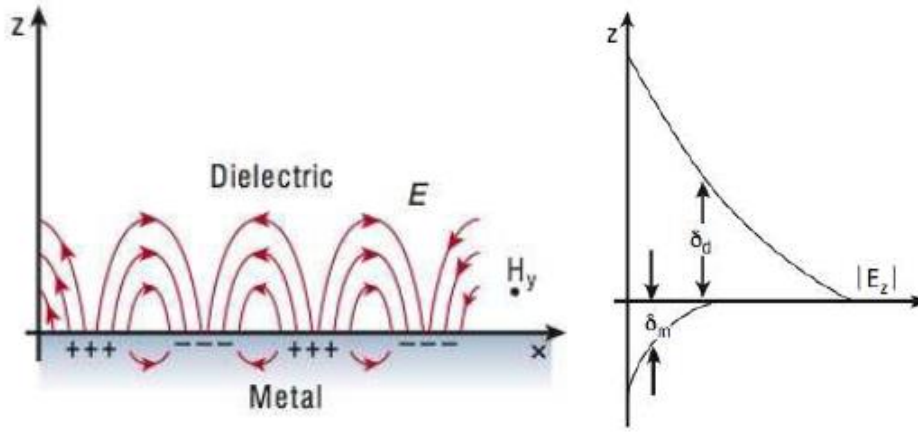
Figure 1.1 Surface Plasmon Polaritons fields at the metal/dielectric interface.

Figure 1.1 schematically shows the system under analysis. We have a metal/dielectric interface along the $z=0$ plane. The uniform metal region is confined in the $z<0$ region meanwhile the uniform dielectric one is defined by the $z>0$ region. In each one of these two regions the value of the dielectric permittivity is constant and uniform therefore in equations 1.9 and 1.10 can be simplified becoming two typical Helmholtz equations:

$$\nabla^2 E + \varepsilon k_0^2 E = 0 \quad (1.11)$$
$$\nabla^2 H + \varepsilon k_0^2 H = 0 \quad (1.12)$$

where we have extracted the time harmonic propagation term and define $k_0 = \omega/c$.

Since we want the wave to be guided along the interface, we can assume that the wave is travelling in the x-direction since the system is symmetric for z-axis rotation. Finally taking into account that the system is also symmetric for y-axis translations we can assume that the general form of the magnetic fields is described by:

$$E(x, y, z) = E(z)e^{ik_x x}$$
$$H(x, y, z) = H(z)e^{ik_x x} \quad (1.13)$$

Applying this field assumptions into the Helmholtz equations (1.11) and (1.12) we obtain:

$$\frac{\partial^2 \boldsymbol{H}(z)}{\partial z^2} + (\varepsilon k_0^2 - k_x^2)\boldsymbol{H}(z) = 0 \tag{1.14}$$

$$\frac{\partial^2 \boldsymbol{E}(z)}{\partial z^2} + (\varepsilon k_0^2 - k_x^2)\boldsymbol{E}(z) = 0 \tag{1.15}$$

These equations are the starting point for the study of electromagnetic modes in waveguides, and more specifically for the analysis of SPP' dispersion relation.

If we try to solve the above equations with the constraints coming from the Maxwell equations 1.2 and 1.4 we will find two independent solutions: the Transverse Magnetic (TM) propagation mode, where only the y-component of magnetic field is present, and the Transverse Electric (TE) propagation mode where only the y-component of electric field is present.

Both the dielectric and metallic medium can be described by a dielectric constant $\varepsilon_d = \epsilon_d' + i\epsilon_d''$ and $\varepsilon_m = \epsilon_m' + i\epsilon_m''$, respectively. As we can see in this case we separate the real and imaginary part of the dielectric constant. Now with these definition we can write the matching conditions at the interface:

$$\boldsymbol{E}_d^{\parallel} = \boldsymbol{E}_m^{\parallel}$$
$$\varepsilon_d \boldsymbol{E}_d^{\perp} = \varepsilon_m \boldsymbol{E}_m^{\perp} \tag{1.16}$$

$$\boldsymbol{H}_d^{\parallel} = \boldsymbol{H}_m^{\parallel}$$
$$\mu_d \boldsymbol{H}_d^{\perp} = \mu_m \boldsymbol{H}_m^{\perp} \tag{1.17}$$

If we assume that a possible solution for the Maxwell's equations in the TM mode has this form

$$\boldsymbol{H}_j = (0, H_j^y, 0)\, e^{i(k_{x,j}x \pm k_{z,j}z)}$$
$$\boldsymbol{E}_j = (E_j^x, 0, E_j^z)\, e^{i(k_{x,j}x \pm k_{z,j}z)} \tag{1.18}$$

Where j stands for dielectric (d) or metal (m) part of the wave guide.

In this case if we want to find a solution confined at the interface we have to assume $k_{z,j}$ purely imaginary and so we have to take the plus sign if z > 0 and the minus sign for z < 0 .

Immediately the boundary conditions 1.16 and 1.17 implies that

$$k_{x,d} = k_{x,m} = k_x \tag{1.19}$$

Inserting these fields in equation 1.14 we obtain the following algebraic relations:

$$k_{z,d}^2 = k_x^2 - k_0^2 \varepsilon_d$$
$$k_{z,m}^2 = k_x^2 - k_0^2 \varepsilon_m \tag{1.20}$$

Taking the curl relationship (1.4) for the TM case we found other conditions that has to be satisfied

$$\nabla \times \boldsymbol{H}_j = \begin{pmatrix} \mp H_j^y ik_{z,j} e^{i(k_x x \pm k_{z,j} z - \omega t)} \\ 0 \\ H_j^y ik_x e^{i(k_x x \pm k_{z,j} z - \omega t)} \end{pmatrix} = \varepsilon_j \frac{\partial \boldsymbol{E}}{\partial t}$$

$$= \begin{pmatrix} -i\varepsilon_j \omega E_j^x e^{i(k_x x \pm k_{z,j} z - \omega t)} \\ 0 \\ -i\varepsilon_j \omega E_j^z e^{i(k_x x \pm k_{z,j} z - \omega t)} \end{pmatrix}$$

(1.21)

Considering the x-component and applying the boundary conditions 1.16 and 1.17 we obtain the system:

$$\begin{cases} \dfrac{k_{z,d}}{\epsilon_d} H_d^y + \dfrac{k_{z,m}}{\epsilon_m} H_m^y = 0 \\ H_d^y - H_m^y = 0 \end{cases}$$

(1.22)

Which admits solution only if its determinant vanishes:

$$\frac{k_{z,d}}{\varepsilon_d} + \frac{k_{z,m}}{\varepsilon_m} = 0$$

(1.23)

If we now consider the case $\epsilon_d'' \approx \epsilon_m'' \approx 0$ we can see that in order to solve the equation the metallic nature of the lower part of the wave guide is crucial for the existence of surface waves. In fact for a metallic material $Re(\varepsilon_m) < 0$ hence 1.23 has solution.

Inserting this equation into (1.20) we obtain the *Surface Plasmon Polaritons dispersion relation*

$$k_x = \frac{\omega}{c} \sqrt{\frac{\epsilon_d' \epsilon_m'}{\epsilon_d' + \epsilon_m'}}$$

(1.24)

SPP can exist only if we consider the incident light in TM mode. If the TE mode is considered the previous calculations get the following equation instead of the 1.23:

$$(k_{z,d} + k_{z,m})E_j^y = 0$$

(1.25)

But in order to have a confined solution $\mathrm{Re}[k_{z,j}] = 0$ and $\mathrm{Im}[k_{z,j}] > 0$, this implies that the only solution for equations 1.25 is $E_j^y = 0$; hence no SPP propagates in TE mode.

We will now analyse the propagation length and the penetration depth of the SPPs. The propagation length can be derived by considering the SPP propagation constant we found in 1.24. Taking into account the complete metal dielectric constant the modulus of its real part is much larger than its imaginary part $|\epsilon_m'| \gg \epsilon_m''$ and the expression can be developed in a Taylor series:

$$k_x = \beta = \beta' + i\beta'' = \frac{\omega}{c} \sqrt{\frac{\epsilon_d' \epsilon_m'}{\epsilon_d' + \epsilon_m'}} + i \frac{\epsilon_m''}{2(\epsilon_m')^2} \frac{\omega}{c} \left(\frac{\epsilon_d' \epsilon_m'}{\epsilon_d' + \epsilon_m'} \right)^{3/2}$$

(1.26)

The imaginary part of the propagation constant represents the SPP wave attenuation by the metal adsorption. This Implies that the field intensity decays with a characteristic length of $L = 1/2\beta''$.

Metal:	$\varepsilon_m @ \lambda = 635\,nm$	$L_{air}[\mu m];\ \varepsilon_d = 1$	$L_{water}\ [\mu m];\ \varepsilon_d = 1.78$
Gold	-10.7 + i1.3	7.8	2.9
Silver	-17.0 + i0.7	3.8	1.5
Aluminium	-51.7 + i18.6	14.1	5.8

Table 1.1: Values of SPP propagation length calculated for three different metals both in air and in water obtained by stimulating the surface with a light having a 635 nm wavelength.

In Table 1.1 we report the different values of the of SPP propagation length calculated for three different metals: gold, silver, and aluminium. The calculations were performed for both air and water dielectric. A 635 nm wavelength was supposed to excite the SPP. As we can see in air we obtain a decay length between 3.8 µm and 14.1 µm meanwhile this range is almost halved if water is considered as the dielectric medium.

Another important physical factor is the penetration length of the SPP inside the metal and dielectric domain. These spatial extension is due to the fact that the electric field exponentially decreases in the direction perpendicular to the interface plane $E = E_0 \exp(-|k_{z,j} z|)$, see equation 1.18. The penetration length is defined as the value of z where the electric field intensity decays of a factor $1/e$:

$$d_{z,j} = \frac{1}{k_{z,j}} = \frac{\lambda_0}{2\pi} \sqrt{\left| \frac{\epsilon'_d + \epsilon'_m}{\left(\epsilon'_j\right)^2} \right|} \qquad (1.27)$$

Where λ_0 is the vacuum wavelength of the light used for excite the SPP, and the subscripts $j = d$ or m stand for the quantities calculated in the dielectric and metallic medium, respectively. This parameter gives a geometrical idea of the region where the SPP energy is confined. The following table 1.2 reports these quantities for some special cases:

Metal:	$\varepsilon_m @ \lambda = 635\,nm$	$d_{z,\ air}\ [nm];\ \varepsilon_d = 1$		$d_{z,\ water}\ [nm];\ \varepsilon_d = 1.78$	
		dielectric	metal	dielectric	metal
Gold	-10.7 + i1.3	314	29	169	28
Silver	-17.0 + i0.7	404	23	221	23
Aluminium	-51.7 + i18.6	719	13	402	13

Table 1.2 Values of fields penetration deep calculated for three different metals both in air and in water obtained by stimulating the surface with a light having a 635 nm wavelength

As we can see inside the metal layer the electric field rapidly decays having a penetration depth ranging from 30nm and 10 nm. On the contrary, the SPP penetration depth is always higher than 314 nm for the air case and 169 nm for the water case. We will see in section 3.4.1 how this penetration depth can be used in order to predict the effect of a thin dielectric films onto the metal layer as proposed by Jung [20] in the Effective Medium Approximation (EMA).

1.2   Excitation of Surface Plasmon Polaritons

In the previous sections we saw how to retrieve the SPP coupling constant but we did not explain how to excite these electromagnetic guided modes. The excitation problems arise from the fact that the light momentum in the dielectric is always lower than the SPP one, hence these modes cannot be excite just by lighting the metal/dielectric interface.

In order to calculate the SPP dispersion relation an expression for the metal dielectric constant has to be found. The simpler model for its the description is the *plasma model*. In this model the free electrons of the metal are described as a gas of free electron that moves around a fixed background of positive ion cores. The effect of the metallic lattice influences this model by modifying the effective electron mass used and its validity extends until the lowest visible frequencies. Below these wavelengths some interactions between the atom bounded electrons and the light appear. We can consider that the electron gas responds to an applied electric field following the sequent equation:

$$m\ddot{x} = -m\gamma\dot{x} - e\mathbf{E}$$ (1.28)

Where x is the displacement from the equilibrium position, γ represents a damping contribution, m and e are the electron effective mass and charge.

Assuming now an harmonic time dependency the equation 1.28 can be algebraic solved and the displacement becomes:

$$x(t) = \frac{e}{m(\omega^2 + i\gamma\omega)}\mathbf{E}(t)$$ (1.29)

Subsequently the polarization of the metal atoms becomes:

$$\mathbf{P} = -en\mathbf{x} = -\frac{ne^2}{m(\omega^2 + i\gamma\omega)}\mathbf{E}$$ (1.30)

Where n is the density of the free electrons.

Relating this polarization filed with the relative dielectric constant, we obtain:

$$\varepsilon(\omega) = 1 - \frac{\omega_p^2}{\omega^2 + i\gamma\omega}$$ (1.31)

In this equation $\omega_p = \frac{ne^2}{\epsilon_0 m}$ is the plasma frequency for the free electron gas and it is related to the frequency of the longitudinal oscillations of the free electron gas.

The dielectric function can be divided into its real and imaginary part as follow:

$$\epsilon'(\omega) = 1 - \frac{\omega_p^2\tau^2}{1 + \omega^2\tau^2}; \; \epsilon''(\omega) = \frac{\omega_p^2\tau}{\omega(1 + \omega^2\tau^2)}$$ (1.31)

Here $\tau = \frac{1}{\gamma}$ represents the time occurring between dumping collisions, and it is known as the relaxation time; γ represents therefore the collision frequency.

Typical value for gold are $\omega_p = 12.1 \times 10^{15}$ sec[-1] (corresponding to a photon of 8 eV or 155 nm) and $\tau = 2.7 \times 10^{-14}$ sec (corresponding to a photon of 25 meV or 49 μm if the corresponding frequency γ is considered) [21].

If we consider $\omega\tau \gg 1$ for (635 nm $\omega \sim 3\ 10^{15}$ Hz) the damping is negligible and the dielectric function is predominantly real:

$$\epsilon(\omega) = 1 - \frac{\omega_p^2}{\omega^2} \qquad (1.32)$$

Inserting the above expression for the metal dielectric function in the SPP momentum (eq 1.24) we obtain the dispersion curves plotted in figure 1.2.
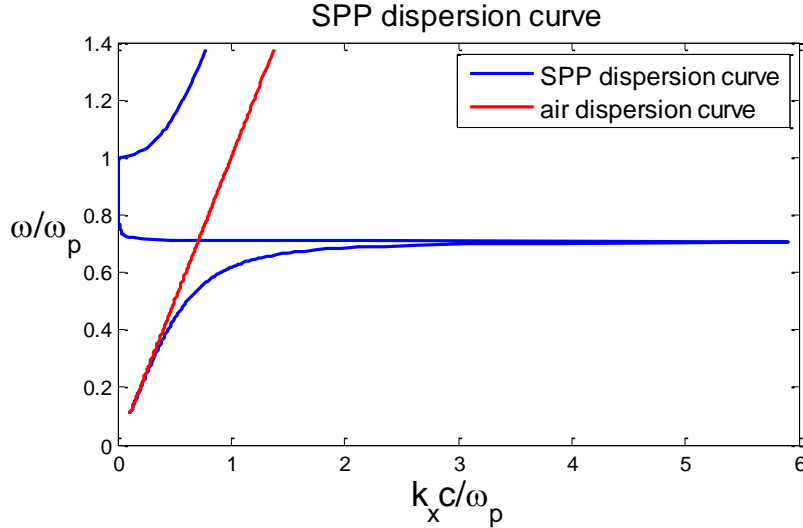

Figure 1.2 dispersion curves for the SPP propagating between air and a metal having the dielectric constant obtained from the plasma model (blue curve) and the light one in air (red curves).

We see that the dispersion curve of a SPP lies always on the right side of the dispersion relation of light in vacuum. This implies that SPP cannot be directly excited by lighting the surface but and additional momentum to the incoming photon must be added.

The coupling of the SPP at a metal dielectric interface is substantially determined by the morphology of the metal dielectric interface. If the surface is flat the coupling method requires to enhance the momentum of the coupling photon. Meanwhile if the surface is nanostructured the photon momentum is enhanced by exploiting the grating momentum. We will describe in detail the two cases in the following section.

1.2.1 Flat Surfaces

The most used method for the excitation of SPP along a flat metal/dielectric interface is the Attenuated Total Internal Reflection (ATR). A typical scheme for ATR method is a three layers system consisting on a thin metal film sandwiched between two dielectric media, for instance a glass prism and air or water, with their dielectric constant respectively ϵ_p, ϵ_d where the relation $\epsilon_p > \epsilon_d$ must be satisfied. The x-component of the light momentum on the metal/glass interface is $k_x = k_0\sqrt{\epsilon_p} \sin\theta$ where θ is the incident angle. This momentum is not sufficient to excite SPP at the metal/glass interface. Nevertheless if we are in Total Internal Reflection (TIR) condition an evanescent wave propagates parallel to the glass interface and if the metal film has the correct thickness (~ 50 nm) this wave excite the SPP at the metal/air interface

In this case the condition that must be satisfied is:

$$k_0\sqrt{\epsilon_p}\ \sin\vartheta = \ k_0\sqrt{\frac{\varepsilon_d\varepsilon_m}{\varepsilon_d+\varepsilon_m}} \qquad (1.33)$$

This relation tells us that there is a cross point between the curve of light dispersion in prism and the curve of SPP dispersion at metal/air interface.

This idea has been implemented into two different excitation configurations: the Kretschmann and the Otto one[3], [4].
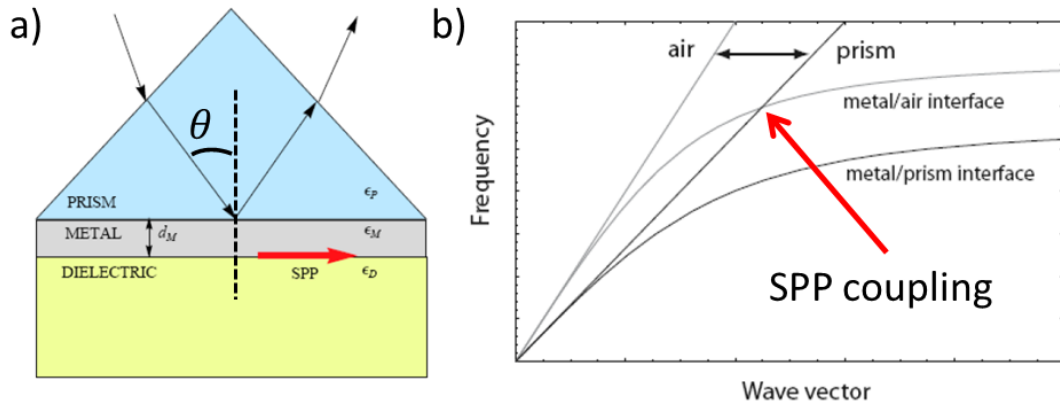

Figure 1.3 a) Schematic of the Kretschmann coupling method b) dispersion curves of the methods

In figure 1.3a we report the typical Kretschmann configuration. The light incoming from the prism impinges the metal films with an angle θ. Then when the correct incident angle is reached, SPP is excited at the metal/dielectric interface. If the intensity of the reflected ray is plotted as a function of θ a minimum appears when the SPP is excited. In figure 1.3b we report the dispersion curves of this system. As we can see the curve that represented the SPP at the metal/air interface is intersected by the dispersion relation of light inside the prism. This intersection point represents the SPP excitation. This is allowed by the fact that for the same frequency the photon momentum inside the prism is higher by factor $\sqrt{\varepsilon_p}$ reducing the slope of the dispersion relation respect to the one in air, and intersecting, in this way the SPP curve.

The Otto configuration (Figure 1.4a) is similar to the Kretschmann one but in this case the metal layer is not in contact with the prism and there is a thin dielectric air layer between the prism and the metal layer. As well as the previous case the SPP excitation happens when the system is in TIR condition and the excitation manifest as a reflectance minimum. Obviously the gap between the prism and the metal must be correctly set in order to obtain a good coupling.
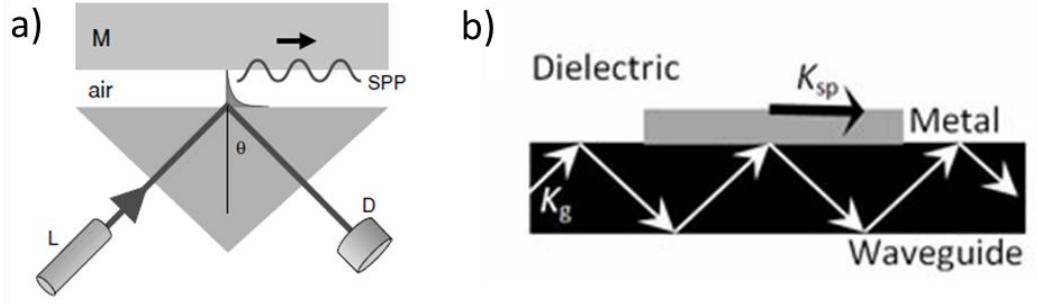
Figure 1.4 a) Otto configuration, b) waveguide confguration

The last method that could be used for the excitation of the SPP on flat surfaces is the waveguide method [22] shown in Figure 1.4b. In this case a region of the waveguide is modified by inserting a finite metal film between the waveguide core and the dielectric medium. When the light passes through the modified part of the waveguide, it can excite SPP causing a drop in the waveguide transmittance.

Nowadays the Kretschmann configuration is the most used for the SPP excitation and study. This is due to the fact that the flat metal/dielectric interface is easy to fabricate, and this methodology is the one implemented in the most SPR commercial instruments.

1.2.2 Nanostructured surfaces

In Order to excite the SPP a nanostructured surface can also be used. In these structures the ability to control the light and the SPP at the nanoscale offered a new kind of prospective such as plasmonic lens, and vortex [23], [24].

Nevertheless we are interested here in periodic nano-structures where the grating momentum can be described by a vector $\boldsymbol{G}$ constant in all the space. Hence the missing momentum for the excitation of the SPP is supplied by the grating itself (See Figure 1.5), satisfying this simple vector equation:

$$\boldsymbol{k}_{SPP} = \boldsymbol{k}_{\parallel}^{(in)} + m\boldsymbol{G} \tag{1.33}$$

where $\boldsymbol{k}_{SPP}$ is the plasmonic momentum, $\boldsymbol{k}_{\parallel}^{(in)}$ is the projection onto the grating plane of the incoming light momentum and $m \in \mathbb{Z}$ is the grating diffraction order that allow the coupling. This equation can be simplified to a scalar form if all the three vectors are aligned:

$$k_{SPP} = k_0\sqrt{\epsilon_d}\,\sin\theta + m|\boldsymbol{G}| = k_{x,n} \tag{1.34}$$

where $|\boldsymbol{G}| = \frac{2\pi}{\Lambda}$ is the modulus of the grating momentum and Λ is the grating period.

When this resonance condition is satisfied by the n-th diffraction order the diffraction the input light power is delivered to the SPP and experimentally a minimum in the reflectance or a maximum in the grating transmittance are observed.
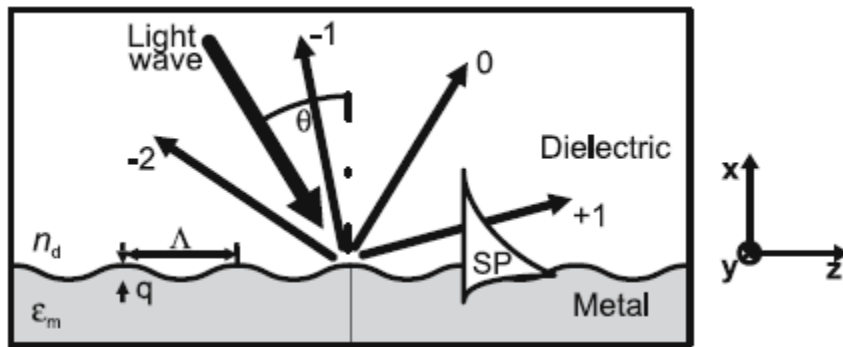
Figure 1.5.Grating coupling scheme.

Figure 1.5 reports the simplified version of the grating coupling mode. In this case $k_{\parallel}^{(in)}$ reduces to $k_{i,x}$ and the momentum of the diffracted rays differs from the incoming light momentum by multiples of the grating coupling momentum.

In section 2.4 we will analysed more in details the Grating coupling configurations applying it to the more general case of two-dimensional periodic structures in conical mounting configurations. Moreover we will see in chapter 3 how this method, based on a vector equation, correctly predicts the SPR position.

1.3   Surface plasmon resonance sensors

Surface Plasmon Resonance sensors can measure small changes in the refractive index occurring at a metal/dielectric interface thanks to their evanescent field that penetrates in the dielectric medium [12], [16]. A change in the dielectric refractive index configuration gives rise to a change in the propagation constant of the SPP condition. These variations modify measurable quantities like resonance angles, coupling wavelength, phase or intensity of the light reflected or transmitted by the interface as reported in Figure 1.6.

Figure 1.6: Concept of surface plasmon resonance sensor

The core of SPP resonance biosensor is composed by a bio-recognition layer, an analyte target molecule, and a transducer. The bio-recog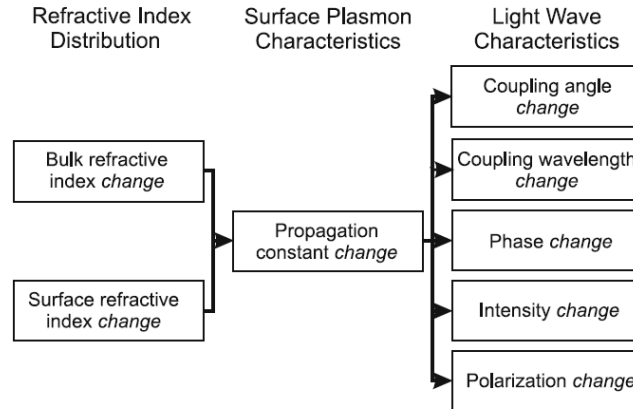nition layer is immobilized over the metal film supporting the SPP and it is able to recognize and bind some selected analytes. These analytes are usually immersed in a liquid buffer solution that flows over the bio-recognition layer. The binding of the analytes to the bio recognition layer increases the effective refractive index. This increase changes the SPP coupling constant, hence affecting the SPR.

1.3.1   Performances

The performances of a SPR biosensor can be described by using some parameters such as sensitivity, resolution, linearity, accuracy, reproducibility and limit of detection. The sensor response Y to a given value of the measurand X can be predicted by the sensor transfer function F, $Y = F(X)$ determined from a theoretical sensor model or by a sensor calibration curve. In our case the measurand X refers to the chemical or biological analyte concentrations that causes the changes in the surface refractive index configuration [9], [12], [16].

Sensitivity:

The sensor sensitivity is the ratio of the change in sensor output to the change in the measurand (or slope of the calibration curve):

$$S = \frac{\partial Y}{\partial X} \tag{1.35}$$

We can also define a refractometric sensitivity that describes the sensitivity of the SPR sensor to the refractive index n and can be written as

$$S_{RI} = \frac{\partial Y}{\partial n} \tag{1.36}$$

and similarly a sensitivity of an SPR biosensor to the concentration of analyte c

$$S_c = \frac{\partial Y}{\partial c} \tag{1.37}$$

The sensitivity of a SPR biosensor to the concentration of the analyte can be decomposed into two main factors:

$$S_c = \frac{\partial Y}{\partial c} = \frac{\partial Y}{\partial n}\frac{dn(c)}{dc} = S_{RI}S_{nc} \tag{1.38}$$

where S_{nc} is derived from the refractive index change caused by the binding of analyte concentration c to the biorecognition layer.

The sensitivity of a SPR sensor to a refractive index S_{RI} is given by two contributions:

$$S_{RI} = \frac{\partial Y}{\partial n_{eff}}\frac{\delta n_{eff}}{\delta n_b} = S_{RI1}S_{RI2} \tag{1.39}$$

The first term S_{RI1} depends on the method of excitation of surface plasmons and it represents an instrumental contribution. The second term S_{RI2} describes the sensitivity of the effective index of a surface plasmon to the refractive index and it is independent respect to the SPP excitation method. These last term mainly depends on the profile of the refractive index (for instance a bulk or surface refractive index changes).

Resolution:

The resolution of a SPR biosensor is defined as the smallest change in the bulk refractive index that produces a detectable change in the sensor output and it is strictly related to the level of uncertainty of the sensor output. The resolution σ_{RI} is typically expressed in terms of the standard deviation of the sensor output noise, σ_{so}, translated to the refractive index of bulk medium, $\sigma_{RI} = \sigma_{so}/S_{RI}$.

Dominant sources of noise are the fluctuations in the light intensity emitted by the light source, the laser in our case, the shot noise associated with photon statistics, associated to the conversion of the light intensity into electric signal.

Noise in the intensity of light emitted by the light source is proportional to the intensity and its standard deviation σ_L can be given as $\sigma_L = \sigma_{rL}I$ where σ_{rL} is relative standard deviation and I is the measured light intensity.

Shot noise is associated to random arrival of photons on a detector and the corresponding random production of photoelectrons. Photon flux usually obeys Poisson statistics and produces a shot noise σ_S which is directly proportional to the square root of the detected light intensity: $\sigma_S = \sigma_{rS}\sqrt{I}$ where σ_{rS} is relative standard deviation. Detector noise consists of several contributions that originate mostly in temperature noise and its standard deviation σ_D is independent on the light intensity.

The resulting noise of a measured light intensity σ_I is a statistical superposition of all the noise components and it is expressed as:

$$\sigma_I(I) = \sqrt{I^2 \sigma_{rL}^2 + I \sigma_{rS}^2 + \sigma_D^2} \qquad (1.40)$$

Linearity, accuracy, and reproducibility:

Sensor linearity defines the extent to which the relationship between the measurand and the sensor output is linear over the working range. Linearity is usually specified in terms of the maximum deviation from a linear transfer function over the specified dynamic range. Sensors with linear transfer function are desirable as they require fewer calibration points to produce an accurate sensor calibration. However, response of SPR biosensors is usually a non-linear function of the analyte concentration and therefore calibration needs to be carefully considered.

The sensor accuracy describes the agreement between a measured value and a true value of the measurand i.e. the analyte concentration.

The sensor reproducibility refers to the ability of the sensor to return the same output when measuring the same value of measurand.

Limit of detection (LOD)

LOD is the concentration of analyte c_L derived from the smallest measure Y_L that can be detected with reasonable certainty. The value is given by

$$Y_{LOD} = Y_{blank} + m\,\sigma_{blank} \qquad (1.41)$$

where Y_{blank} is the mean of the blank (sample with no analyte) measures, σ_{blank} is the standard deviation of the blank measures, and m is a numerical factor chosen according to the confidence level desired (typically m = 2 or 3).

As $c_{blank} = 0$, the LOD concentration c_{LOD} can be expressed as:

$$c_{LOD} = \left.{m\,\sigma_{blank}}\middle/{S_c(c = 0)}\right. \qquad (1.42)$$
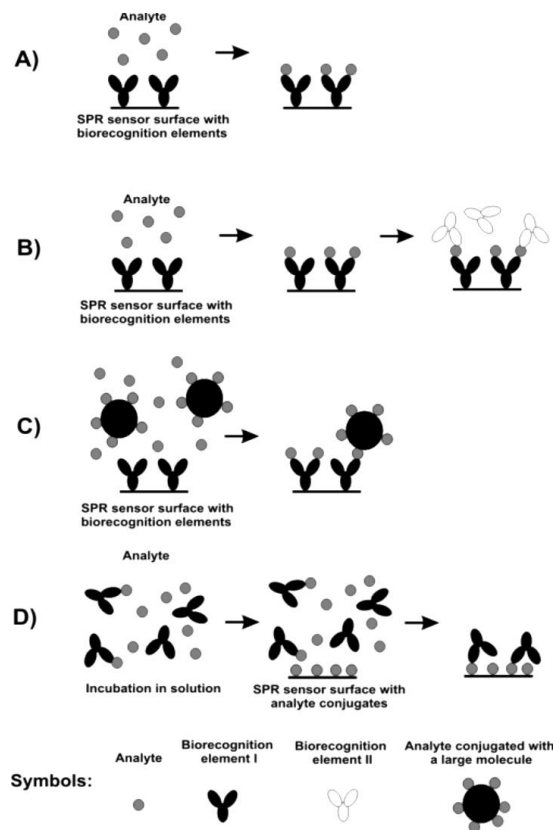
1.3.2 Detection techniques

Figure 1.7 Main detection formats used in SPR biosensors: A) direct detection; B) sandwich detection format; C) competitive detection format; D) inhibition detection format.

In the previous section (eq 1.38) we have seen that the SPP sensitivity to some analyte concentrations is governed by two factors one due to the detection method S_{RI} and the other one due to the ability of the analyte to cause a change in the refraction index S_{nc}.

If only the detection method is considered S_{RI} we can defined a resolution of the instrument by defining the small refractive index variations that can be detected. This value seems to have reached an intrinsic limit of 10-7 RIU [25] even if some authors claims it could be reduced until 10-8 RIU [26]–[30]. Nevertheless this seems to be an ultimate limits for this detection technique and therefore in order to increase the resolution and the LOD for an analyte concentration several detection formats were developed. We report the main ones in Figure 1.7 [12].

The detection format is chosen on the basis of analyte target molecules size, interaction with the bio-recognition layer, and range of concentrations.

The simplest detection scheme is the direct one reported in Figure 1.7a. In this case the direct binding between the analyte and the biorecognition layer is able to produce a sufficient response of the sensor in the desired analyte concentrations range. The specificity and LOD can be improved by using the sandwich detection format (Figure 1.7b). Here a second antibody attaches to the bound analyte layer enhancing in this way the SPP response, proportionally to the bounded analytes.

Small analytes (molecular weight < 5000) often does not generate a sufficient change in the refractive index. This is due to the fact that the analyte molecules usually are captured by a bio recognition layer that acts as a spacer between them and the metal surface. This spacer decreases the molecular sensitivity S_{nc}, due to the evanescent nature of the SPP electric field inside the dielectric. Thanks to the competitive or inhibition detection format one can overcome this low S_{nc} value.

The competitive detection format is reported in Figure 1.7c. Here the surface is coated with fixed number of binding sites i.e. antibody. In the solution both analytes and bigger conjugate analyte molecules are present. Since the two species compete for the same binding site, and only if the large conjugate molecules bound we can detect a signal, the SPR variations is inversely proportional to the analyte concentration.

The inhibition method is presented in Figure 1.7d. Here fixed concentration of antibodies is mixed in a solution with an unknown concentration of their affinity analyte. On the surface sensors the same analytes were previously immobilized. When the solution containing both antibodies and analytes flows over the surface the free antibodies bind with the immobilized analyte. Also in this case the response is inversely proportional to the analyte concentration since the greater is the SPR signal the more antibodies are free to bind and this means a low analyte concentration.

1.3.3 Applications

The fields where SPR biosensors find application can be divided into three main categories: medical diagnostic, environmental monitoring, and food safety[12].

Regarding the medical area SPR biosensors proved to be useful tools to detect: viruses [31], [32], cancer markers [33], [34], myocardial infarction [35], allergy markers[36], ageing correlated diseases[37], and some other as antibodies drugs and hormones [38]. In the following table 1.3 some applications of the SPR for the identification of medical analytes are listed:

analyte	sensor system	detection matrix	limit of detection	detection format
cancer markers				
prostate-specific	Ibis II	3% BSA in PBS	0.15 ng/mL	sandwich
antigen (PSA)	Biacore 2000	buffer	10 ng/mL	direct
			1 ng/mL	sandwich
PSA−ACT complex	Biacore 2000	HBS buffer	20.7 ng/mL	direct
(α_1-antichymotrypsin)		HBS buffer	10.2 ng/mL	sandwich
		human serum	47.5 ng/mL	direct
		human serum	18.1 ng/L	sandwich
carbohydrate antigen	Spreeta	buffer	410.9 U/mL	direct
(CA 19-9)		buffer	66.7 U/mL	sandwich
vascular endothelial growth factor (VEGF)	cutom-built SPRI	buffer	1 pM	sandwich
interleukin-8 (IL-8)	Biacore X	buffer	2.5 pM (∼0.02 ng/mL)	sandwich
		human saliva	184 pM (∼1.5 ng/mL)	
carcinoembryonic antigen (CEA)	Autolab Springle	buffer	0.5 ng/mL	direct
fibronectin	custom-built	buffer	2.5 μg/mL	direct
		buffer	0.5 μg/mL	sandwich
		buffer	0.25 μg/mL	amplification
antibodies against viral pathogens				
hepatitis virus specific	Biacore 1000	human serum		direct
	Spreeta	5% serum in PBS	9.2 nM	direct
			4.4 nM	sandwich
			0.64 nM	amplified
anti-hepatits simplex virus	Biacore X	serum in HBS (1:100)		direct
anti-EBNA	custom-built	1% human serum	0.2 ng/mL	direct
anti-protein S	Biacore X	plasma 1:5		direct
anti-RSV	Biacore 2000	HBS Buffer		direct
anti-adenoviral	Biacore 3000	ascites fluid in Hepes (1:10)		direct

Table 1.3 Medical applications of SPR sensing

There are also several application in the environmental monitoring fields. The analytes taken into consideration by these fields are pesticides[39], aromatic hydrocarbons [40], [41], heavy metals [42], phenols [43], and dioxins [44]. In the following table 1.4 some applications of the SPR for the identification of environmental quantities are listed:

analyte	sensor system	detection matrix	limit of detection	detection format
pesticides				
atrazine	Sensia	water	20 pg/mL	inhibition
			1 pg/mL	
chlorpyrifos	custom-built	water	50 pg/mL	inhibition
carbaryl	custom-built	water	1 ng/mL	inhibition
DDT	Sensia	water	15 pg/mL	inhibition
DDT		water	18 pg/mL	inhibition
carbaryl			50 pg/mL	
chloropyrifos			52 pg/mL	
2,4-dichlorophenoxyacetic acid	SPR-20	buffer	0.5 ng/mL	inhibition
	custom-built	buffer	10 ppt	inhibition
2,4,6-trinitrotoluene (TNT)				
	Biacore 2000	buffer	10 pg/mL	inhibition
	Biacore 2000	buffer	10 pg/mL	inhibition
aromatic hydrocarbons				
2-hydroxybiphenyl	SPR-20	buffer	0.1 ng/mL	inhibition
benzo[a]pyrene	SPR-20	buffer	0.01 ng/mL	inhibition
	SPR-20	buffer	0.05 ng/mL	inhibition
heavy metals				
Cu^{2+} ions	custom-built	buffer	~pM	direct
Cd, Zn, Ni	Biacore X	buffer	~μM	direct
Cu^{2+}	custom-built	deionized water	32 pM	direct
Ni^{2+}			178 pM	
phenols				
bisphenol A	SPR-20	buffer	10 ng/mL	inhibition
	Spreeta	buffer	1 ng/mL	inhibition
2,4-dichlorphenol	SPR-20	buffer	20 ng/mL	competitive
PCB	Biacore 2000	buffer	2.5 ng/mL	competitive
2,3,7,8-TCDD	Biacore 2000	buffer	0.1 ng/mL	competitive

Table 1.4 Environmental applications of SPR

SPR sensors finds applications also in food analysis. In these fields they are used to monitor pathogens [45], toxins[46], drug residues [47], vitamins, hormones, antibodies [48], chemical contaminants, allergens, and proteins [49]. Some applications of the SPR for the identification of different bacteria in foods are listed in table 1.5:

analyte	sensor system	detection matrix	limit of detection	detection format
Escherichia coli O157:H7				
	Multiskop	buffer	10^4 cells/mL	direct
	Multiskop	buffer	10^2 cells/mL	direct
	custom-built	detergent-lysed bacteria	10^4 cfu/mL	sandwich
		heat-killed bacteria	10^5 cfu/mL	
		untreated bacteria	10^6 cfu/mL	
	Spreeta	BPV solution	8.7×10^6 cfu/mL	direct
	Spreeta	aqueous solution	10^6 cells/mL	direct
	SR 7000	PBST solution	10^3 cfu/mL	sandwich
	custom-built	heat-killed bacteria in buffer	1.4×10^4 cfu/mL	sandwich
		apple juice, pH 7.4	10^5 cfu/mL	
	Biacore 2000	pasteurized milk	25 cfu/mL	direct
	Spreeta	milk; apple juice; ground beef	10^2-10^3 cfu/mL	direct
Salmonella spp.				
S. enteritidis	custom-built	heat-killed bacteria in buffer	10^6 cfu /mL	direct
S. group A, B, D, E	Biacore 3000	HBS-EP solution	1.7×10^5 cfu/mL	sandwich
S. typhimurium	Multiskop	buffer	10^2 cfu/mL	direct
S. paratyphi	Multiskop	buffer	10^2 cfu/mL	direct
	Plasmonic	milk	10^5 cells/mL	sandwich
S. choleraesuis	custom-built	buffer	4.4×10^4 cfu/mL	sandwich
		apple juice, pH 7.4	10^4 cfu/mL	
S. enterica	Biacore 2000	pasteurized milk	23 cfu/mL	direct
Lysteria monocytogenes				
	custom-built	heat-killed bacteria in buffer	10^7 cfu /mL	direct
	Biacore 3000	PBS solution	10^5 cells/mL	competitive
	custom-built	apple juice, pH 7.4; buffer	3×10^3 cfu/mL	sandwich
Campylobacter jejuni				
	custom-built	heat-killed bacteria in buffer	1×10^5 cfu/mL	sandwich
		apple juice, pH 7.4	5×10^4 cfu/mL	
Staphylococcus aureus				
	SR 7000	PBST soluiton	10^5 cfu/mL	sandwich
			10^7 cfu/mL	direct
	Spreeta	buffer	10^4 cfu /mL	direct

Table 1.5 Food safety application of SPR.

Many other examples of SPR sensing applications could be listed here but this goes far beyond our goal. In fact, since SPR detection is nowadays accepted as a standard laboratory tools used to monitor the interaction kinetics between probe and analyte, it is almost impossible list all its application. For a complete review of this sensing field, update to the year 2008, the reader is reminded to the Homola work [12].

2 Surfaces Simulation Methods

In this chapter we will exploit different methods used for the reflectance and transmittance simulation from a nanostructured surface. The first two methods i.e. the Rigorous Coupled Wave Analysis Method (RCWA) [50]–[54]and the Chandezon Method (CM) [55]–[57], are currently widely used by the scientific community to analyse both unidimensional and bidimensional periodical structures[58]–[62]. Even if the first description of these two methods dates back to the 1980, they are constantly studied for improving their efficiency and applications.

The Finite Element Method (FEM) is nowadays one of the most widespread numerical techniques for the simulation of structures with applications that reach electromagnetic [63], thermal, chemical and mechanical fields. Since its implementation is very complex, dedicated software were developed over the years. In our case we used the radio frequency package implemented in Comsol v3.5 in order to solve both unidimensional and bidimensional periodic structures.

Finally we will generalize the vector model introduced in section 1.2.2. This method is the easiest way to predict where Surface Plasmon Resonance will occur when periodic structured surface is used. Nevertheless it does not give any information about their shape in relation with the periodic geometrical structure.

Our developed simulation methods will reproduce the behaviour of periodic structures lighted in conical mounting configuration. The general scheme is reported in Figure 2.1.
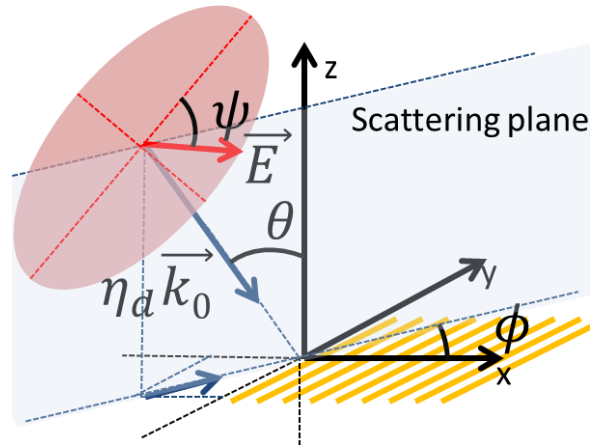

Figure 2.1 Conical mounting configuration scheme.

Figure 2.1 represents a unidimensional grating (yellow lines) lighted in conical configuration. The grating surface lays in the x, y plane. The incident wave vector $\eta_d \overrightarrow{k_0}$ along with the vector normal to the grating plane defines the scattering plane (cyan transparent layer). The incoming light electric field $\vec{E}$ lays on the polarization ellipse (red coloured ellipse).

Three main angles described this configuration: the incident angle θ; the polarization angle ψ, and the azimuthal angle ϕ. As we can see ϕ is defined as the angle between the grating momentum $\vec{G}$ (In figure2.1 it coincides with the x- axis) and the scattering plane. When $\psi = 0°$ we will refer to the transverse magnetic polarization mode (TM) meanwhile when $\psi = 90°$ we will refer to the Transverse Electric polarization mode (TE).

Looking at this reference system the incoming light wave vector can be written as:

$$\eta_d \vec{k_0} = \eta_d \begin{cases} k_0 sin\theta cos\phi \\ k_0 sin\theta sin\phi \\ -k_0 cos\theta \end{cases}$$ (2.1)

And the electric field as:

$$\vec{E} = E_0 \begin{cases} cos\psi\ cos\theta\ cos\phi + sin\psi\ sin\phi \\ cos\psi\ cos\theta\ sin\phi - sin\psi\ cos\phi \\ cos\psi\ sin\theta \end{cases}$$ (2.2)

The unidimensional periodic grating structures can be simulated in the conical mounting configuration by using the RCWA and the FEM methods we developed, meanwhile we restricted the CM to light incoming with ϕ=0° and in TM or TE polarization mode. The simulation of the two dimensional periodic structures in conical mounting configuration will be performed by using only the FEM method.

2.1 Rigorous Coupled Wave Analysis Method

The RCWA method or Fourier Modal Method (FMM) was developed over the '80s and '90s. Its aim is to rigorously solve the electromagnetic fields problem inside a periodic structure, and therefore calculate the light diffraction coefficients. One of the first paper on the subject dates back to 1981 [50] but the true success of this method arrived in 1995 were the work of M.G. Moharam [51], [52]and P. Lalanne[64] improved the convergence of this method.

Here we will briefly describe this method and the modifications that must be introduced to improve the method convergence and stability. Here we will strictly follow the formulation proposed in [52], where only the TM lighting mode for ϕ = 0° is considered. Nevertheless we implemented a full model to perform the simulation in conical mounting configuration.
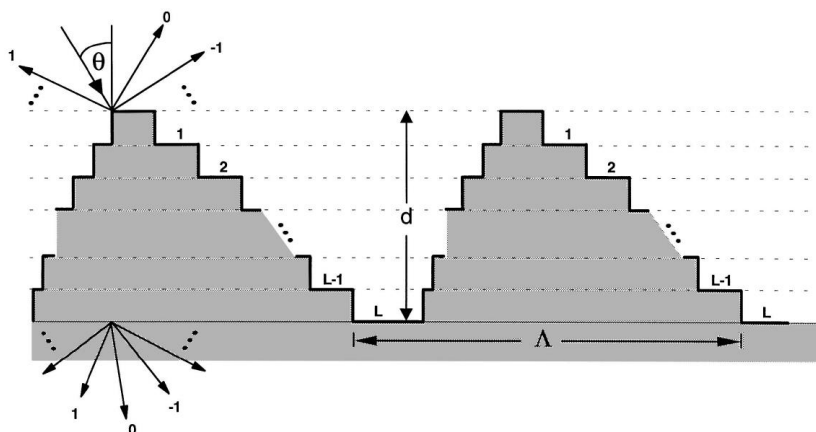

Figure 2.2 Geometry for the study of diffraction grating using the RCWA method

Figure 2.2 shows how a general grating profile is treated by the RCWA method. There is an upper continuum medium where an incident plane wave along with the grating reflected rays

propagate. The incident light incomes with an angle θ respect to the normal of the grating plane. The transmitted rays propagate in a lower medium that also acts as the grating substrate.

The region between the upper and lower medium is the grating region and it is characterized by a periodic distribution of the dielectric constant along the x-direction. Is therefore possible to develop it in a Fourier series:

$$\varepsilon(x,z) = \sum_h \varepsilon_h(z) \exp\left(j\frac{2\pi h}{\Lambda}x\right) \tag{2.3}$$

Here $\varepsilon_h(z)$ is the h-th Fourier component which incorporates the z-dependence of the dielectric function. In order to apply the RCWA method we need to eliminate the z-dependency of the Fourier component. We can achieve this by dividing the grating region in an arbitrary number of slabs having a definite height as shown in figure 2.2. It is obvious that increasing the number of layers every grating profile can be describe with the desired accuracy; and it is also evident that this method well describe the case of a digital grating. In this way the dielectric constant inside the grating region acquires this mathematical formulation:

$$\varepsilon_l(x) = \sum_h \varepsilon_{l,h} \exp\left(j\frac{2\pi h}{\Lambda}x\right); \ \ D_l - d_l < z < D_l; \ D_l = \sum_{p=1}^l d_l \tag{2.4}$$

where d_l represent the thickness of the l-th layer. The field in the upper region of the grating is represented by:

$$H_{I,y} = exp\{-jk_0\eta_I[\sin(\theta)\,x + \cos(\theta)\,z]\} + \sum_i R_i exp\{-j[k_{xi}x - k_{I,zi}z]\} \tag{2.5}$$

where the first term represents the incident field meanwhile the second term represents the reflected component of the field.

In the lower medium we got the transmitted rays:

$$H_{II,y} = \sum_i T_i exp\{-j[k_{xi}x - k_{II,zi}(D_L - z)]\} \tag{2.6}$$

In all the fields expression we hide the temporal dependency $e^{i\omega t}$. The quantity k_{xi}, $k_{II,zi}$, and $k_{I,zi}$ are determined from the Rayleigh-Floquet field expansion:

$$\begin{aligned} k_{xi} &= k_0[\eta_I \sin(\theta) - i\,(\lambda_0/\Lambda)] \\ k_{l,zi} &= \sqrt{k_0^2\eta_l^2 - k_{xi}^2}; l = I, II \end{aligned} \tag{2.7}$$

The tangential magnetic and electric field in the l-th grating layer are expressed through a Fourier expansion:

$$\begin{aligned} H_{l,gy} &= \sum_i U_{l,yi}\,(z)\exp(-jk_{xi}x) \\ E_{l,gx} &= j\sqrt{\frac{\mu_0}{\varepsilon_0}}\sum_i S_{l,xi}\,(z)\exp(-jk_{xi}x) \end{aligned} \tag{2.8}$$

By using the Maxwell's equations:

$$\nabla \times H = \frac{\varepsilon_0 \varepsilon \partial E}{\partial t} \ \ ; \ \ \nabla \times E = -\frac{\mu_0 \mu \partial H}{\partial t} \tag{2.9}$$

The three following useful equations can be obtained:

$$\frac{\partial H_y}{\partial z} = -j\omega\varepsilon_0\varepsilon(x,z)E_x$$
$$\frac{\partial H_y}{\partial x} = j\omega\varepsilon_0\varepsilon(x,z)E_z \qquad (2.10)$$
$$\frac{\partial E_x}{\partial z} = -j\omega\mu_0\mu H_y + \frac{\partial E_z}{\partial x}$$

By solving the equations 2.10 inside each grating slab, and taking into account that in our case $\mu = 1$ we get the following relation:

$$\frac{\partial^2 H_{l,gy}}{\partial z^2} = \left[-k_0^2\,\varepsilon(x) + \varepsilon(x)\frac{\partial}{\partial x}\frac{1}{\varepsilon(x)}\frac{\partial}{\partial x}\right]H_{l,gy} \qquad (2.11)$$

Since the grating is periodic, we assume that the fields $H_{l,gy}$, and the dielectric constant inside each slab can be written as a Fourier sum. Hence the equation 2.11 can be solved considering the functions $\exp(-jk_{xi}x)$ as a base. Therefore it assumes the sequent matrix form:

$$\frac{\partial^2 \mathbf{U}_{l,y}}{\partial(z')^2} = [\mathbf{E}_l]\left[\mathbf{K}_x\mathbf{E}_l^{-1}\mathbf{K}_x - \mathbf{I}\right]\mathbf{U}_{l,y} \qquad (2.12)$$

where $z' = k_0 z$, $\mathbf{I}$ is the unitary matrix, $\mathbf{K}_x$ is a diagonal matrix with diagonal element k_{xi}/k_0, and $\mathbf{E}_l$ is the matrix with its i,p-th element $\varepsilon_{l,i-p}$.

Being the functions $U_{l,yi}(z)$ only a function of z, they can be solved assuming a finite number n for the Rayleigh expansion of the fields, since the matrix equation 2.12 represents a standard eigenvalue problem. Therefore the analytical expression for $U_{l,yi}(z)$ becomes:

$$U_{l,yi}(z) = \sum_{m=1}^{n} w_{l,i,m}\left\{c_{l,m}^+ \exp\left[-k_0 q_{l,m}(z - D_l + d_l)\right]\right.$$
$$\left. + c_{l,m}^- \exp\left[k_0 q_{l,m}(z - D_l)\right]\right\} \qquad (2.13)$$

where $w_{l,i,m}$ are the elements of the eigenvector matrix $\mathbf{W}_l$ and $q_{l,m}$ are the square root with positive real part of the eigenvalues of the matrix $[\mathbf{E}_l]\left[\mathbf{K}_x\mathbf{E}_l^{-1}\mathbf{K}_x - \mathbf{I}\right]$. The coefficients $c_{l,m}^+$ and $c_{l,m}^-$ are unknown constant that will be determined by imposing the adequate boundary conditions between each grating layer.

In order to fully solve the system we need also to find the condition for the tangential component of the electric field E_x which are expressed in a matrix form by the equation:

$$\mathbf{S}_{l,x} = [\mathbf{E}_l]\frac{\partial \mathbf{U}_{l,y}}{\partial(z')} \qquad (2.14)$$

Imposing the boundary conditions between the input region and the first grating layer (z=0) we obtain:

$$\begin{bmatrix}\delta_{i0} \\ j\delta_{i0}cos(\theta)/\eta_I\end{bmatrix} + \begin{bmatrix}\mathbf{I} \\ -j\mathbf{Z}_I\end{bmatrix}\mathbf{R} = \begin{bmatrix}\mathbf{W}_1 & \mathbf{W}_1\mathbf{X}_1 \\ \mathbf{V}_1 & -\mathbf{V}_1\mathbf{X}_1\end{bmatrix}\begin{bmatrix}\mathbf{c}_1^+ \\ \mathbf{c}_1^-\end{bmatrix} \qquad (2.15)$$

By applying it at the boundary between the $l-1$ and l grating layers we have:

$$\begin{bmatrix}\mathbf{W}_{l-1}\mathbf{X}_{l-1} & \mathbf{W}_{l-1} \\ \mathbf{V}_{l-1}\mathbf{X}_{l-1} & -\mathbf{V}_{l-1}\end{bmatrix}\begin{bmatrix}\mathbf{c}_{l-1}^+ \\ \mathbf{c}_{l-1}^-\end{bmatrix} = \begin{bmatrix}\mathbf{W}_l & \mathbf{W}_l\mathbf{X}_l \\ \mathbf{V}_l & -\mathbf{V}_l\mathbf{X}_l\end{bmatrix}\begin{bmatrix}\mathbf{c}_l^+ \\ \mathbf{c}_l^-\end{bmatrix} \qquad (2.16)$$

At the boundary between the last grating layer and the substrate region ($z = D_L$) we get:

$$\begin{bmatrix} \mathbf{W}_L\mathbf{X}_L & \mathbf{W}_L \\ \mathbf{V}_L\mathbf{X}_L & -\mathbf{V}_L \end{bmatrix}\begin{bmatrix} \mathbf{c}_L^+ \\ \mathbf{c}_L^- \end{bmatrix} = \begin{bmatrix} \mathbf{I} \\ j\mathbf{Z}_{II} \end{bmatrix}\mathbf{T}$$

(2.17)

In this cases $\mathbf{V}_l = \mathbf{E}_l^{-1}\mathbf{W}_l\mathbf{Q}_l$ with $\mathbf{Q}_l$ a diagonal matrix with the diagonal elements $q_{l,m}$, $\mathbf{X}_L$ is a diagonal matrix with the diagonal elements $\exp(-q_{l,m}d_l)$; $\mathbf{Z}_I$ and $\mathbf{Z}_{II}$ are diagonal matrix with the element $k_{I,zi}/\eta_I^2\,k_0$ and $k_{II,zi}/\eta_{II}^2\,k_0$ respectively. $\mathbf{R}$ and $\mathbf{T}$ are column matrixes with the reflection and transmission coefficient respectively meanwhile δ_{i0} is the usual Kronecker function. All these boundary condition can be summarized in an easy formulation:

$$\begin{bmatrix} \delta_{i0} \\ j\delta_{i0}cos(\theta)/\eta_I \end{bmatrix} + \begin{bmatrix} \mathbf{I} \\ -j\mathbf{Z}_I \end{bmatrix}\mathbf{R} = \prod_{l=1}^{L}\begin{bmatrix} \mathbf{W}_l & \mathbf{W}_l\mathbf{X}_l \\ \mathbf{V}_l & -\mathbf{V}_l\mathbf{X}_l \end{bmatrix}\begin{bmatrix} \mathbf{W}_l\mathbf{X}_l & \mathbf{W}_l \\ \mathbf{V}_l\mathbf{X}_l & -\mathbf{V}_l \end{bmatrix}^{-1}\begin{bmatrix} \mathbf{I} \\ j\mathbf{Z}_{II} \end{bmatrix}\mathbf{T}$$

(2.18)

This expression may appear simple but it cannot be solved straightforwardly due to the numerical error that will be produce in the matrix inversion. This errors are due to the very small number produced by $\exp(-q_{l,m}d_l)$ in the diagonal element of the matrix $\mathbf{X}_l$. In order to avoid these numerical errors we implemented in our code the full solution approach described in [52].

Once the coefficients $\mathbf{R}$ and $\mathbf{T}$ are found the reflectance and transmittance of the diffracted ray can be found by using these two equations:

$$DE_{ri} = R_iR_i^*\mathrm{Re}[k_{I,zi}/k_0\eta_I\cos(\theta)]$$
$$TE_{ri} = T_iT_i^*\mathrm{Re}[k_{II,zi}\,\eta_I/k_0\eta_{II}^2\cos(\theta)]$$

(2.19)

The accuracy of the solution returned by this method depends on the number of the retained harmonics in the field expansion. Nevertheless the convergence rate of the diffraction efficiency parameters as a function of the number of retained harmonics depends on the light polarization i.e. it is slower for the TM mode respect to the TE one. A straight forward solution of this problems comes from the work of Lalanne [64] that propose to substitute the matrix equation 2.12 with this one:

$$\frac{\partial^2 \mathrm{U}_{l,y}}{\partial(z')^2} = [\mathrm{A}_l^{-1}][\mathrm{K}_x\mathrm{E}_l^{-1}\mathrm{K}_x - \mathrm{I}]\mathrm{U}_{l,y}$$

(2.20)

Being A the matrix formed by the inverse permittivity harmonic coefficient. He also further developed this technique and give the complete reformulation for the conical mounting problem.

Our standard grating description is performed by the model reported in figure 2.3 which shows the grating periodic cell cross section.
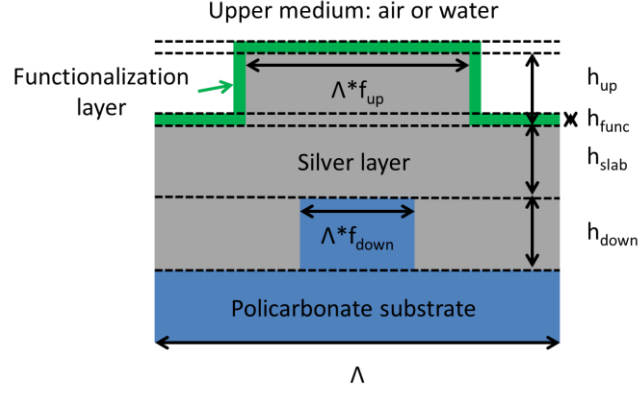
Figure 2.3 Standard grating geometrical description.

As we can see from Figure 2.3 our grating is a five layers system. The polycarbonate substrate is described by the blue area, the grey area represents the silver layer and the green layer that covers all the upper interface describes the functionalization layer. The dashed lines represent the interface between each of the grating layer where boundary conditions must be imposed. In most of the grating slabs the dielectric constant is described by a rectangular function. For example, if we consider the fifth layer, that corresponds to the silver-polycarbonate-silver layer, its Fourier transform coefficients are:

$$\varepsilon_{5,m} = \varepsilon_{poly} sinc(m) + \left(\varepsilon_{poly} - \varepsilon_{Ag}\right) f_{down}(sinc(mf_{down})) \qquad (2.21)$$

The layer that needs a particular description is the second one (from the upper interface of the grating), where we have three different materials that describe the dielectric constant. In this case the Fourier coefficients becomes:

$$\varepsilon_{2,m} = \varepsilon_{air} sinc(m) + \left(\varepsilon_{func} - \varepsilon_{air}\right) f_{func} \left(sinc(mf_{func})\right) \\ + \left(\varepsilon_{Ag} - \varepsilon_{func}\right) f_{up}(sinc(mf_{up})) \qquad (2.22)$$

In order to test the implemented method we consider in figure 2.4 the diffraction coefficients obtained by using the Moharam and Lalanne implementations. We performed the calculations for both the TM and TE polarization, considering an incident angle of 15° and an azimuthal angle of 0°. In reference to figure 2.3 the geometrical parameters used in this simulation are respectively:

λ	Λ	f_{up}	f_{down}	h_{down}	h_{up}	h_{slab}	h_{func}	ε_{air}	ε_{Ag}	ε_{func}	ε_{poly}
635 nm	740 nm	0.45	0.3	20 nm	20 nm	35 nm	1.5 nm	1	-17-0.7i	1	2.4964

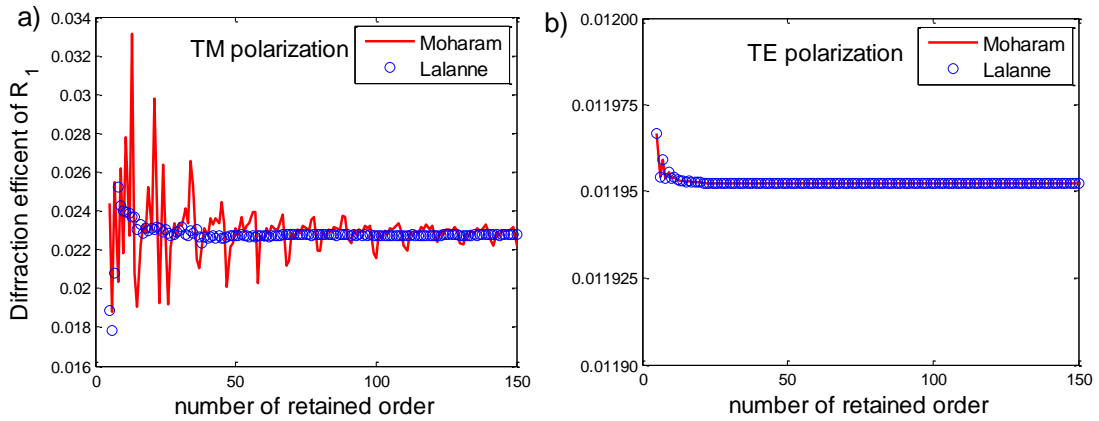**Table 2.1 Parameters used for the digital grating cross section description**

Figure 2.4 A comparison between the diffraction efficiency convergence by using the old and new method for: (a) TM, and (b) TE polarization

In figure 2.4 we reported the Diffraction efficiency of the R_{-1} reflected ray as a function of the number of retained Rayleigh orders in the field expansion (2N+1). The continuous red line refers to the Moharam formulation meanwhile the blue circles refers to the Lalanne formulation. As we can see the method quickly converge in both the formulation for the TE polarization (Figure 2.4b), while for the TM (Figure 2.4a) we get an enormous improvement of the convergence rate by adding the Lalanne modifications. Also the oscillatory behaviour is completely suppressed.

A complete explanation of the numerical problem of the different rate convergence can be found in the work of L. Li [65] and further developed for the two dimensional periodic structures case by Schuster [54]. The treatment of this topics goes far beyond our purpose here; nevertheless we can see from figure 2.4 that our implemented code well converge if a number N = 100, that corresponds to 2N+1 retained harmonics, is used.

2.2   Chandezon method

The first Implementation of the Chandezon or curvilinear, or differential method dates back to 1982 [55]. The difference between CM and RCWA it is well explained by figure2.5 [66].
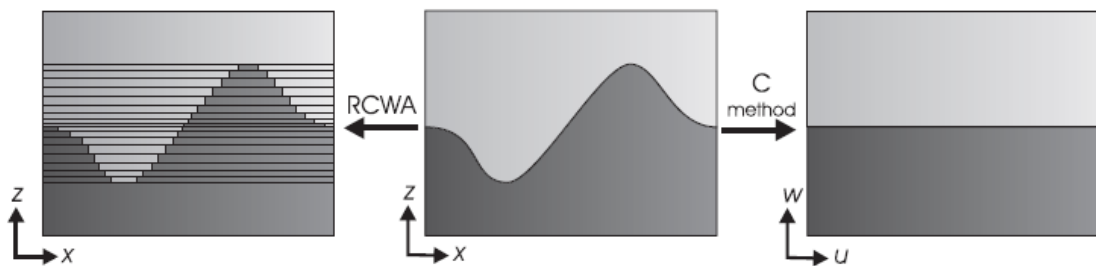

Figure 2.5 Difference in the grating profile treatment between the RCWA and Chandezon Method.

Starting from the grating profile describe in the central panel of figure 2.5, the RCWA method divides the grating region in a huge amount of layers each one with a particular step dielectric function profile $\varepsilon(x)$ (left panel of figure 2.5), while the Chandezon method, through a change in the coordinates system, transforms the grating profile in a planar interface, eliminating in this way the z-dependency of the dielectric function inside the grating region. In the new coordinate

system the problem is reduced to the calculations of transmission and reflection of light passing through a set of planar interfaces.

For briefly illustrate the method we will follow the derivation showed by Li [67]. Nevertheless we generalized the Li method description allowing a multilayer coating for the grating, hence we can describe the thin silver film, and the functionalization coating layer. The method we implemented reproduces the behaviour of the grating lighted by the TM polarization mode, and with the grating slits perpendicular to the scattering plane, i.e. ϕ= 0°. It is also suited for the description of discontinuous grating profile such as a trapezoidal or triangular one because it uses the same electromagnetic formulation introduced in [58], [68].
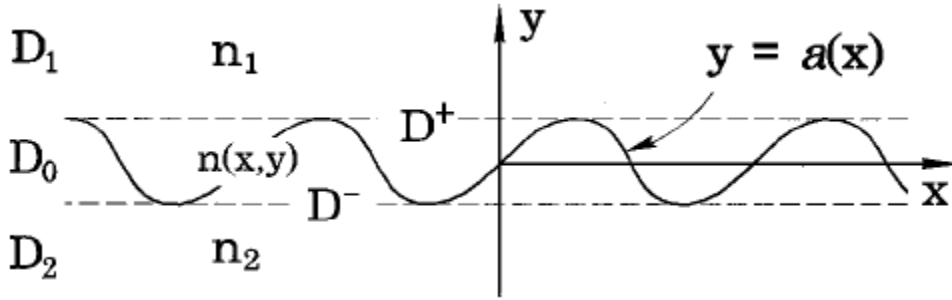

Figure 2.6 schematic for the CM implementation.

We considered a periodically corrugate interface, invariant in the z-direction between two homogeneous isotropic media with refractive index η_I, η_{II} respectively. The grating period and amplitude are denoted by Λ and d. The incident angle is θ and the scattering plane is perpendicular to the grating slits. The harmonic time convention $\exp(-i\omega t)$ is assumed. In figure 2.6 the grating is described by a function $y = a(x)$ that splits the space into two regions called D^+, D^-.

The space could be also further divided into three regions by using the dashed lines: D_1, D_2, D_0. In the domains D_1, and D_2 the field can be written as in eq. 2.5 and 2.6 by using the Ryleigh - Floquet expansion:

$$F = \sum_m A_m^{(p)\pm} \exp(j\alpha_m x \pm i\beta_m^{(p)} y), p = 1,2 \tag{2.23}$$

where $F = H_z$, $\alpha_m = \eta_1 k_0 \sin(\theta) + mK$, $K = 2\pi/\Lambda$, $\beta_m^{(p)} = \left(\eta_p^2 k_0^2 - \alpha_m^2\right)^{1/2}$ with $\text{Re}\left[\beta_m^{(p)}\right] + \text{Im}\left[\beta_m^{(p)}\right] > 0$, and $A_m^{(p)\pm}$ are constant amplitudes. Since no reflected wave could propagate in the D_1 domain backward the y-direction, except for the incoming light ray, and no transmitted wave could propagate in the substrate along the y direction we can simplify the notation saying that $A_0^{1-} = 1; A_m^{(1)+} = A_m^{(1)}; A_m^{(2)-} = A_m^{(2)}$.

This grating problem is therefore reduced to solve the Helmholtz equation in D^+ and D^-, conditioned by the previously described boundary conditions at infinity, and along the grating profile.

$$\left[\frac{\partial^2}{\partial x^2} + \frac{\partial^2}{\partial y^2} + k_0^2 \mu \varepsilon(x,y)\right] F = 0 \tag{2.24}$$

If we consider the above equation 2.24 in the domains D^+ or D^- for the change of variable:

$$\begin{cases} v = x \\ u = y - a(x) \end{cases} \tag{2.25}$$

The differential operators become:

$$\begin{cases} \dfrac{\partial}{\partial x} = \dfrac{\partial}{\partial v} - \dot{a}\,\dfrac{\partial}{\partial u} \\[2mm] \dfrac{\partial}{\partial y} = \dfrac{\partial}{\partial u} \end{cases} \tag{2.26}$$

where $\dot{a} = \mathrm{d}a/\mathrm{d}x$. Substituting these expressions into the Helmholtz equation 2.24 we obtain this differential operator:

$$L(\partial_u, \partial_v, x) = \frac{\partial^2}{\partial v^2} - 2\dot{a}\frac{\partial}{\partial v}\frac{\partial}{\partial u} - \ddot{a}\frac{\partial}{\partial u} + (1 + \dot{a}^2)\frac{\partial^2}{\partial u^2} + k_0^2 \mu \varepsilon_p \tag{2.27}$$

For convenience we will use x insteadof v to label the spatial variable since $x = v$. In this coordinate system if x varies and u is kept constant, the point (x, u) traces curves parallel to the grating profile, therefore ε remains constant.

The second order equation 2.27 can be rewritten as a pair of first order equations:

$$\begin{bmatrix} k_0^2 \mu \varepsilon_p + \dfrac{\partial^2}{\partial v^2} & 0 \\ 0 & 1 \end{bmatrix}\begin{pmatrix} F \\ F' \end{pmatrix} = \begin{bmatrix} i\left(\dfrac{\partial}{\partial v}\dot{a} + \dot{a}\dfrac{\partial}{\partial v}\right) & 1 + \dot{a}^2 \\ 1 & 0 \end{bmatrix}\dfrac{\partial}{i\partial u}\begin{pmatrix} F \\ F' \end{pmatrix} \tag{2.28}$$

Taking into account that the fields F must respect the same periodicity of the grating and since the wave in D^+ and D^- can be treated as plane waves we can write the differential operator:

$$\frac{\partial}{\partial v} \to i\boldsymbol{\alpha}, \qquad \frac{\partial}{\partial u} \to i\rho \tag{2.29}$$

where $\boldsymbol{\alpha}$ is a diagonal matrix formed by α_m.

By inserting this consideration into the equation 2.28 we obtain an eigenvalue problem:

$$\begin{bmatrix} -\dfrac{1}{\boldsymbol{\beta}^{(p)2}}(\boldsymbol{\alpha}\dot{\boldsymbol{a}} + \dot{\boldsymbol{a}}\boldsymbol{\alpha}) & \dfrac{1}{\boldsymbol{\beta}^{(p)2}}(1 + \dot{\boldsymbol{a}}\dot{\boldsymbol{a}}) \\ 1 & 0 \end{bmatrix}\begin{pmatrix} \boldsymbol{F} \\ \boldsymbol{F'} \end{pmatrix} = \frac{1}{\rho}\begin{pmatrix} \boldsymbol{F} \\ \boldsymbol{F'} \end{pmatrix} \tag{2.30}$$

where $\boldsymbol{\beta}^{(p)}$ is a diagonal matrix formed by $\beta_m^{(p)}$ and $\dot{\boldsymbol{a}}$ is the matrix formed by the Fourier coefficients of $\dot{a}$:

$$(\dot{\boldsymbol{a}})_{mn} = (\dot{a})_{m-n} = \frac{1}{\Lambda}\int_0^{\Lambda} \dot{a}(x) exp[-i(m - n)Kx]\,dx \tag{2.31}$$

If each block of the previous 2×2 matrix (eq.2.30) is truncated to $N \times N$, the $2N$ eigenvalues obtained could be divided into two sets. The first set Σ^+ contains the positive real eigenvalues and the eigenvalues that have a positive imaginary part. The second set Σ^- contains the negative real eigenvalues and the eigenvalues that have a negative imaginary part. In the domain D^+ all the eigensolutions in Σ^- except the one corresponding to the incident plane wave should be discarded. Conversely in domain D^- all the eigensolutions in Σ^+ must not be considered since we want our problem to be confined at $u = \infty$.

Now we can write the z-component of the magnetic field in the domains D^+ and D^-.

$$F^+ = \exp\left[i\alpha_0 x - i\beta_0^{(1)} y\right] + \sum_{n \in U^+} \exp\left[i\alpha_n x + i\beta_n^{(1)} y\right] A_n^{(1)}$$

$$+ \sum_m \exp(i\alpha_m x) \sum_{q \in V^+} F_{mq}^+ \exp\left(i\rho_q^+ u\right) C_q^+$$

$$F^- = \sum_{k \in U^-} \exp\left[i\alpha_k x - i\beta_k^{(2)} y\right] A_k^{(2)}$$

$$+ \sum_m \exp(i\alpha_m x) \sum_{r \in V^-} F_{mr}^- \exp(i\rho_r^- u) C_r^-$$

(2.32)

where $A_n^{(p)}$ and $C_q^\pm$ are the unknown diffraction amplitudes, $F_{mq}^\pm$ are the elements of the F part of the q-th eigenvector and $U^\pm$ and $V^\pm$ denote the sets of the indices for the propagating and evanescent orders in domains $D^\pm$ respectively.

As we can note the expression for the total field is written in a mixed variables system. It is therefore convenient to write everything as a function of x and u since $y = u - a(x)$. This substitution allows to expand the exponential function of $a(x)$ in a Fourier series and then to regroup the Fourier coefficients. In this way we obtain:

$$F^+ = \sum_m \exp(i\alpha_m x) \left\{ L_m\left(-\beta_0^{(1)}\right) \exp\left[-i\beta_0^{(1)} u\right] \right.$$

$$+ \sum_{n \in U^+} L_{m-n}\left(\beta_n^{(1)}\right) \exp\left[i\beta_n^{(1)} u\right] A_n^{(1)}$$

$$+ \left. \sum_{q \in V^+} F_{mq}^+ \exp\left(i\rho_q^+ u\right) C_q^+ \right\}$$

(2.33)

$$F^- = \sum_m \exp(i\alpha_m x) \left\{ + \sum_{k \in U^-} L_{m-k}\left(-\beta_k^{(2)}\right) \exp\left[-i\beta_k^{(2)} u\right] A_k^{(2)} \right.$$

$$+ \left. \sum_{r \in V^+} F_{mr}^- \exp(i\rho_r^- u) C_r^- \right\}$$

where $L_m(\gamma)$ is:

$$L_m(\gamma) = \frac{1}{\Lambda} \int_0^\Lambda \exp[i\gamma a(x) - imKx] \, dx$$

(2.34)

Matching the boundary conditions at $u = 0$ is equivalent to satisfy the following matrix equation:

$$\begin{bmatrix} F_{mn}^{R+} & F_{mq}^+ & -F_{mk}^{R-} & -F_{mr}^- \end{bmatrix} \begin{bmatrix} A_n^{(1)} \\ C_q^+ \\ A_k^{(2)} \\ C_r^- \end{bmatrix} = \begin{bmatrix} -F_{m0}^{R,in} \end{bmatrix}$$

(2.35)

where $F_{mn}^{R+} = L_{m-n}\left(\beta_n^{(1)}\right)$, $F_{mk}^{R-} = L_{m-k}\left(-\beta_k^{(2)}\right)$, and $F_{m0}^{Rin} = L_m\left(-\beta_0^{(1)}\right)$

The superscript R is associated to the terms of the Rayleigh solution. The equation 2.35 still cannot be solved since it contains N equations and 2N unknowns. The other N equations are provided by the boundary condition of the electric field that lies in the x, y plane. The electric field component tangential to the grating profile is described by the function $G = E_x + \dot{a}E_y$. By expressing E_x and E_y in terms of H_z we get the following expression for G:

$$G = \frac{Z_0}{ik_0\varepsilon}\left[\dot{a}\frac{\partial F}{\partial v} - (1 + \dot{a}^2)\frac{\partial F}{\partial u}\right] \tag{2.36}$$

By using this fields expression we obtain the complete system:

$$\begin{bmatrix} F^{R+}_{mn} & F^+_{mq} & -F^{R-}_{mk} & -F^-_{mr} \\ G^{R+}_{mn} & G^+_{mq} & -G^{R-}_{mk} & -G^-_{mr} \end{bmatrix}\begin{bmatrix} A^{(1)}_n \\ C^+_q \\ A^{(2)}_k \\ C^-_r \end{bmatrix} = \begin{bmatrix} -F^{R,in}_{m0} \\ -G^{R,in}_{m0} \end{bmatrix} \tag{2.37}$$

where the matrix elements are defined as follow:

$$G^{R+}_{mn} = \frac{Z_0}{k_0\varepsilon_1}\sum_s\left[\dot{a}_{m-s}\alpha_s - (\mathbf{1} + \dot{a}\dot{a})_{ms}\beta^{(1)}_n\right]L_{s-n}\left(\beta^{(1)}_n\right)$$

$$G^{R-}_{mk} = \frac{Z_0}{k_0\varepsilon_2}\sum_s\left[\dot{a}_{m-s}\alpha_s + (\mathbf{1} + \dot{a}\dot{a})_{ms}\beta^{(2)}_k\right]L_{s-k}\left(-\beta^{(2)}_k\right)$$

$$G^{Rin}_{m0} = \frac{Z_0}{k_0\varepsilon_1}\sum_s\left[\dot{a}_{m-s}\alpha_s + (\mathbf{1} + \dot{a}\dot{a})_{ms}\beta^{(1)}_0\right]L_s\left(-\beta^{(1)}_0\right) \tag{2.38}$$

$$G^+_{mq} = \frac{Z_0}{k_0\varepsilon_1}\sum_s\left[\dot{a}_{m-s}\alpha_s - (\mathbf{1} + \dot{a}\dot{a})_{ms}\rho^+_q\right]F^+_{sq}$$

$$G^-_{mr} = \frac{Z_0}{k_0\varepsilon_2}\sum_s\left[\dot{a}_{m-s}\alpha_s + (\mathbf{1} + \dot{a}\dot{a})_{ms}\rho^-_r\right]F^-_{sr}$$

Once the system in eq. 2.37 is solved, the field coefficients $A^{(1)}_n$ and $A^{(2)}_k$ can be used for the calculus of the diffraction amplitudes by using:

$$DE_{ri} = \frac{\beta^{(1)}_n}{\beta^{(0)}_n}\left|A^{(1)}_n\right|^2$$

$$TE_{ri} = \frac{\varepsilon_1\beta^{(2)}_k}{\varepsilon_2\beta^{(0)}_n}\left|A^{(2)}_k\right|^2 \tag{2.39}$$

Now we will consider the generalization of the above method to a multicoated layer.
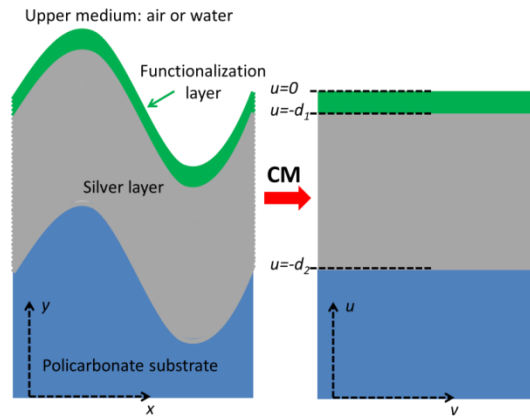

Figure 2.7 Schematic of the Chandezon method applied to the multicoated layer case

Figure 2.7 shows a four media system with three interfaces. The four media are the polycarbonate substrate, the silver layer, the functionalization layer, and the upper medium.

The formulation for the eigenvalues problem in the upper media and in the substrate media follows the previous description, and also in this case only the eigenvalue that respect the bounding conditions at ∞ must be retained in the calculations. Nevertheless, in this case, the

matching of the tangential fields for the silver/polycarbonate interface needs to be evaluate for $u = -d_2$, therefore F_{mk}^{R-} becomes: $F_{mk}^{R-}(-d_2) = F_{mk}^{R-}\exp(id_2\beta_k^{(2)})$ and $F_{mr}^{-}(-d_2) = F_{mr}^{-}\exp(-id_2\rho_r^{-})$. The same considerations applies to the G^{-} factor.

Inside the silver and functionalization layers all the eigenvalues and eigenvectors returned by the equation 2.30 must be retained in the calculations, since they represents reflected and transmitted waves inside the layer. We will call $F_{m\tau,1}^{\pm}$, $\rho_{\tau,1}^{\pm}$ and $F_{m\tau,2}^{\pm}$, $\rho_{\tau,2}^{\pm}$ the eigenvectors and eigenvalues and we found inside the functionalization and silver layer, respectively.

Each of the three equations refers to a boundary condition inside the grating.

The first stands for $u = 0$:

$$\begin{bmatrix} F_{mn}^{R+} & F_{mq}^{+} \\ G_{mn}^{R+} & G_{mq}^{+} \end{bmatrix}\begin{bmatrix} A_n^{(1)} \\ C_q^{+} \end{bmatrix} + \begin{bmatrix} F_{m0}^{R,in} \\ G_{m0}^{R,in} \end{bmatrix} = \begin{bmatrix} F_{m\tau,1}^{\pm} \\ G_{m\tau,1}^{\pm} \end{bmatrix}[C_1] \tag{2.40}$$

The second stands for $u = -d_1$:

$$\begin{bmatrix} F_{m\tau,1}^{\pm}(-d_1) \\ G_{m\tau,1}^{\pm}(-d_1) \end{bmatrix}[C_1] = \begin{bmatrix} F_{m\tau,2}^{\pm}(-d_1) \\ G_{m\tau,2}^{\pm}(-d_1) \end{bmatrix}[C_2] \tag{2.41}$$

And the third stands for $u = -d_2$:

$$\begin{bmatrix} F_{m\tau,2}^{\pm}(-d_2) \\ G_{m\tau,2}^{\pm}(-d_2) \end{bmatrix}[C_2] = \begin{bmatrix} F_{mk}^{R-}(-d_2) & F_{mr}^{-}(-d_2) \\ G_{mk}^{R-}(-d_2) & G_{mr}^{-}(-d_2) \end{bmatrix}\begin{bmatrix} A_k^{(2)} \\ C_r^{-} \end{bmatrix} \tag{2.42}$$

where the matrixes are calculated as follow:

$$F_{m\tau,1;2}^{\pm}(-d) = F_{m\tau,1;2}^{\pm}\exp(-id\rho_{\tau,1;2}^{\pm})$$

$$G_{m\tau,1;2}^{\pm}(-d) = \frac{Z_0}{k_0\varepsilon_{func;Ag}}\sum_s [\dot{a}_{m-s}\alpha_s + (1 + \dot{a}\dot{a})_{ms}\rho_r^{-}]F_{m\tau,1;2}^{\pm}(-d) \tag{2.42}$$

and $\varepsilon_{func;Ag}$ represent the dielectric constant of the functionalization layer and silver layer, respectively.

This matrix systems can be easily solved, since it can be reduced to a form of eq. 2.37. In this way the diffraction coefficients for the multilayer case can be calculated.

We applied this method to the calculation of a grating with a trapezoidal shape and we compare the results with the one obtained by using the RCWA analysis. The grating we used in this example has a trapezoidal shape described by the parameters shown in figure 2.8

In reference with figure 2.8 we used the following geometrical parameter for the grating description:

λ	Λ	f_{up}	f_{down}	h	d_{Ag}	d_{func}	ε_{air}	ε_{Ag}	ε_{func}	ε_{poly}
635 nm	740 nm	0.6	0.75	20 nm	58 nm	1.5 nm	1	-17-0.7i	1	2.4964

Table 2.2 Parameters used for the trapezoidal grating cross section description

For the RCWA calculations we retained 150 Rayleigh orders in the field expansion and we divided the trapezoidal shape in 10 layers. Regarding the CM only 20 Rayleigh orders were used since its convergence proved to be very fast.
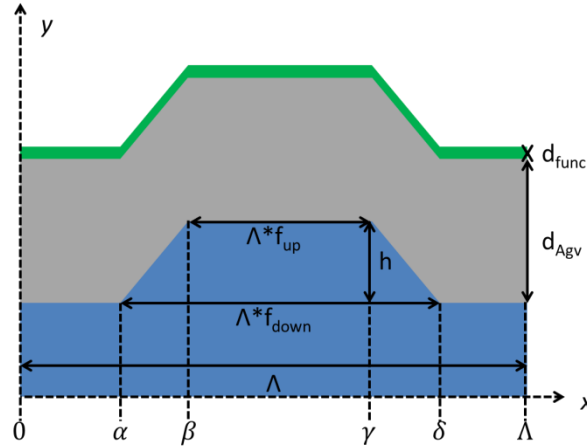
Figure 2.8 Schematic of a trapezoidal cross section for the grating description.

The trapezoidal shape reported in figure 2.8 is described by the following function:

$$a(x) = \begin{cases} 0, & 0 < x < \alpha \\ \dfrac{h}{\beta - \alpha}(x - \alpha), & \alpha < x < \beta \\ h, & \beta < x < \gamma \\ \dfrac{h}{\delta - \gamma}(-x + \delta), & \gamma < x < \delta \\ 0, & \delta < x < \Lambda \end{cases} \qquad (2.43)$$

Considering this function it is easy to calculate the entries of the matrix $\dot{a}$ and the parameters L_m, since it is a case function. The numerical parameter $\alpha, \beta, \gamma, \delta$ can be calculate by considering that we used a isosceles trapeze.
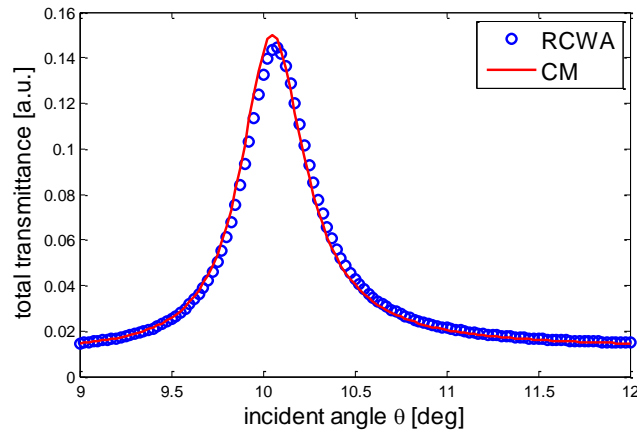

Figure 2.9 Total grating transmittance as a function of θ calculated for the trapezoidal grating using TM polarized light and $\phi=0°$; blue circle RCWA, red continuous line CM.

The figure 2.9 compares the grating total transmittance as a function of θ calculated by using the RCWA (blue circle) and the CM (red line) methods. We can see a good agreement between the results obtained by using the two simulation methods, with exception of some small differences in the maximum. These differences are due to the fact that the CM method we implemented is well suited for the solutions of this trapezoidal shape grating and it is faster respect to the RCWA

where an huge number of layers is used in order to accurately reproduce the grating cross section geometry.

In the general case the CM has some limitations. For example it is not suited for describing the digital grating case since the grating profile derivative is always zero except along the rectangular sides of the grating where it is infinite. Moreover this CM implementation fixes the multilayer profile even if a great number of layers is used. In most of the cases this is not the correct description for the experimental samples since a smooth effect onto the grating profile is usually expected increasing the number of the coating layers.

2.3   Finite Element Method

The finite element method (FEM) is based on the numerical approximation of the electromagnetic field inside a geometrical domain with imposed boundary conditions. In order to reproduce the behaviour of a grating in conical mounting configuration we used a full three dimensional electromagnetic solver, implemented with the software Comsol v3.5. It is not our goal to describe in details how the FEM method works but we will give some information about its implementation for the grating case simulation.

The first step consist on specify the geometry of the periodic cell. In order to achieve this goal we must add a fictitious dimension to the grating: the one along the slits. This dimension permits to solve the system since it can be describe inside a finite domain. The geometry and the parameters of the grating we implemented in this simulation is described in figure 2.10.
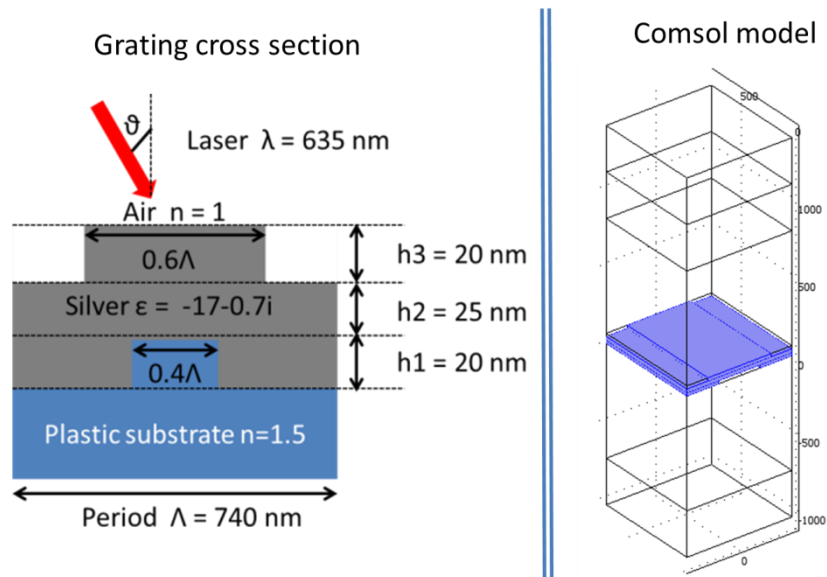

Figure 2.10 Schematic of the grating cross section used for the comparison between the RCWA and FEM method.

The grating cross section is described In figure 2.10 and it is similar to the one reported in figure 2.3 but without the functionalization layer. The parameters used in this formulation are reported in the following table 2.3.

λ	Λ	f_{up}	f_{down}	h_{down}	h_{up}	h_{slab}	h_{func}	ε_{air}	ε_{Ag}	ε_{func}	ε_{poly}
635 nm	740 nm	0.6	0.4	20 nm	20 nm	25 nm	--	1	-17-0.7i	--	2.25

Table 2.3 Geometrical parameters for the grating cross section description.

46

The Comsol corresponding model is showed in figure 2.10 where the blue part represent the silver layer. The domains above the silver layer represent the air meanwhile the ones below represent the polycarbonate substrate.

In order to correctly solve the FEM model the incoming light polarization mode must be specified. If the TM polarization mode is used the model has to be solved for H_x, H_y since the component perpendicular to the grating plane H_z = 0. In each domain the refractive index must be specified and the equation that will be solved is the Helmholtz equation for the Magnetic field components:

$$\nabla \times \left(\frac{1}{\varepsilon_r} \nabla \times \boldsymbol{H}\right) - k_0^2 \boldsymbol{H} = 0 \tag{2.44}$$

The upper and the lower domain are set as Perfectly Matched Layer adsorbing in the z-direction since we want to avoid reflection due to the boundary condition. Along the sides of the periodic cell we impose periodic boundary condition of Floquet type.

$$\boldsymbol{H}_{dst} = \boldsymbol{H}_{src}\exp(-j\boldsymbol{k}(\boldsymbol{r}_{dst} - \boldsymbol{r}_{src})) \tag{2.45}$$

This equation means that the Magnetic field in the destination boundary $\boldsymbol{H}_{dst}$ must be the same of the source $\boldsymbol{H}_{src}$, except for a phase factor. Equation 2.45 forces the solution to be periodic inside the unitary cell. In our case the periodicity momentum is defined by the vector $\boldsymbol{k}$, described in eq. 2.1.

We specify the input field by using the port boundary condition with a wave excitation of unitary input power. The magnetic field has only the x, y component since we want to solve the problem for a TM wave:

$$\boldsymbol{H}_{in} = \begin{cases} sin(\phi)\exp\left(-j(k_x x + k_y x)\right) \\ -cos(\phi)\exp\left(-j(k_x x + k_y x)\right) \\ 0 \end{cases} \tag{2.46}$$

And the propagation constant was set to k_z.

Inside the cell we impose continuity boundary condition. These ensure the continuity of the tangential components of the electric and magnetic fields.

This method solves the magnetic field without using any Rayleigh development of the field. This implies that the power of the various diffracted rays need to be directly calculated by using a Fourier transform of the simulated fields.

The field in the substrate $\boldsymbol{H}_s$ can be described as an expansion in the Rayleigh series as we have already seen for the RCWA (eq. 2.6) and CM (eq. 2.23) methods. In fact:

$$\boldsymbol{H}_s(z) = \sum_{m,n} \boldsymbol{H}_{mn,s} \exp\left(-i\left[\left(k_x + m\frac{2\pi}{\Lambda_x}\right)x \right.\right.$$
$$\left.\left. + \left(k_y + n\frac{2\pi}{\Lambda_y}\right)y\right]\right)\exp(-ik_{mn,sz}z) \tag{2.47}$$

While in the upper region, ranging from the silver layer and the port boundary condition, the upper field $\boldsymbol{H}_u$ assumes the following form:

$$H_u(z) = \sum_{m,n} H_{mn,u} \exp\left(-i\left[\left(k_x + m\frac{2\pi}{\Lambda_x}\right)x\right.\right.$$
$$\left.\left. + \left(k_y + n\frac{2\pi}{\Lambda_y}\right)y\right]\right)\exp(-ik_{mn,uz}z)$$
$$+ cH_{in}\exp(-ik_z(z-h)) \tag{2.48}$$

where $c = \sqrt{\frac{2}{\Lambda_x\Lambda_y}\frac{\varepsilon_0}{\mu_0}\frac{\cos(\theta)}{\eta_u}}$ is a constant that imposes the unitary power to the port, h is the z-quote of the port interface, Λ_x, and Λ_y are the dimension of the unitary periodic cell. The z component of the diffracted ray momentum is:

$$k_{mn,u;sz} = \sqrt{\left(\eta_{u;s}k_0\right)^2 - \left(k_x + m\frac{2\pi}{\Lambda_x}\right)^2 - \left(k_y + n\frac{2\pi}{\Lambda_y}\right)^2} \tag{2.49}$$

with the subscript u, s referring to the upper medium and to the substrate, respectively. After performing the Fourier transform of the H_s or H_u (subtracting the incident field component) we can retrieve the component $H_{mn,s;u}$ and use them in order to evaluate the diffracted rays power:

$$P_{mn,s;u} = \frac{\Lambda_x\Lambda_y}{2\eta_{u;s}}|H_{mn,s;u}|^2\sqrt{\frac{\mu_0}{\varepsilon_0}}\text{Re}[\cos(\theta_{mn,u;s})] \tag{2.50}$$

Where $\theta_{mn,u;s}$ is the light output angle:

$$\theta_{mn,u;s} = \tan^{-1}\frac{\sqrt{\left(k_x + m\frac{2\pi}{\Lambda_x}\right)^2 + \left(k_y + n\frac{2\pi}{\Lambda_y}\right)^2}}{k_{mn,u;s,z}} \tag{2.51}$$

Some physical quantities, such as total reflectance, total transmittance, and absorptance of silver layer, can be calculated by directly using Comsol built-in tools. With such tools, the net power flows through any boundary can be easily calculated. This allows an immediate calculation of the grating total transmittance and reflectance. The power dissipate by the silver layer can be easily evaluated by means of Comsol integration tools by applying this formula:

$$Q = \int_{silver\ domains}\frac{\omega}{2}Im(\varepsilon)|E|^2dV \tag{2.52}$$

We compared this FEM method with the RCWA one by calculating the diffraction efficiencies for a grating with the cross section reported in figure 2.10.
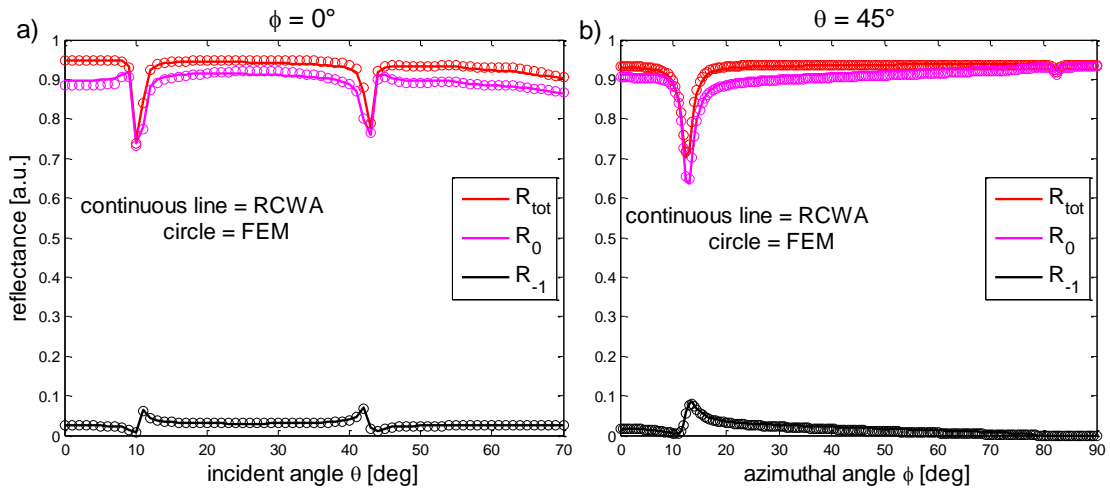
Figure 2.11 Comparison between the reflectance parameters calculated by using the RCWA method (continuous line) and the FEM method (circle): (a) as a function of θ, with φ=0° and (b) as function of φ, with θ=45°. Both calculated in the TM mode.

In Figure 2.11 we reported the comparison between the reflectance parameters R_{tot}, R_0, and R_{-1} calculated by using the RCWA method (continuous line) and the FEM method (circle). In figure 2.11a we report the reflectance as a function of θ, with ϕ=0° meanwhile in figure 2.11b we report the reflectance as function of ϕ, with θ=45°. As we can see there is a perfect agreement between the RCWA and the FEM method.

We performed the same analysis for the transmittance of diffracted rays as can be seen in Figure 2.12. we compared the transmittance parameters T_{tot}, T_0, and T_{-2} calculated by using the RCWA method (continuous line) and the FEM method (circle). In figure 2.11a we report the reflectance as a function of θ, with ϕ=0° meanwhile in figure 2.11b we report the reflectance as function of ϕ, with θ=45°. Also in this case we can see that there is a perfect agreement between the RCWA and the FEM method.
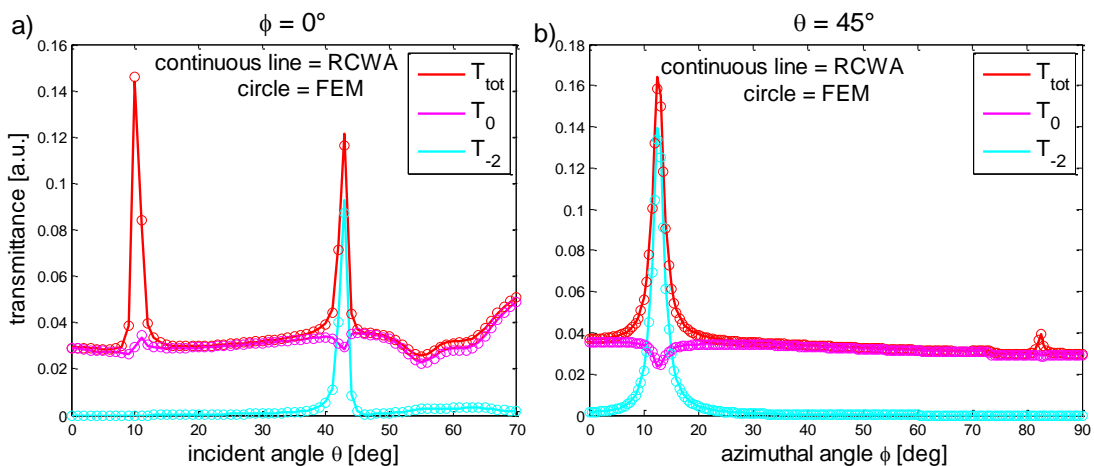

Figure 2.12 Comparison between the Transmittance parameters calculated by using the RCWA method (continuous line) and the FEM method (circle): (a) as a function of θ, with φ=0°; (b) as function of φ, with θ=45°. Both calculated in the TM mode.

Even if the simulation are the same for the RCWA and the FEM method, the latter is more powerful because we can simulate every desired periodic structure, as we will see in section

3.1.2. Moreover, thanks to the Comsol implemented tools, the fields inside the nanostructured surface can be easily calculated. As already specified in the introduction of this chapter, two - dimensional simulations can be performed also by using the RCWA and CM methods. Nevertheless their codes implementation and convergence need a careful and dedicated approach that will not be treated here.

2.4 Vector model method

We already introduced the vector model (VM) in section 1.2.2 applying it to the unidimensional grating in the conical mounting configuration with ϕ=0°. Here we want to generalize it to the bidimensional periodic structure case, considering the conical mounting configuration.
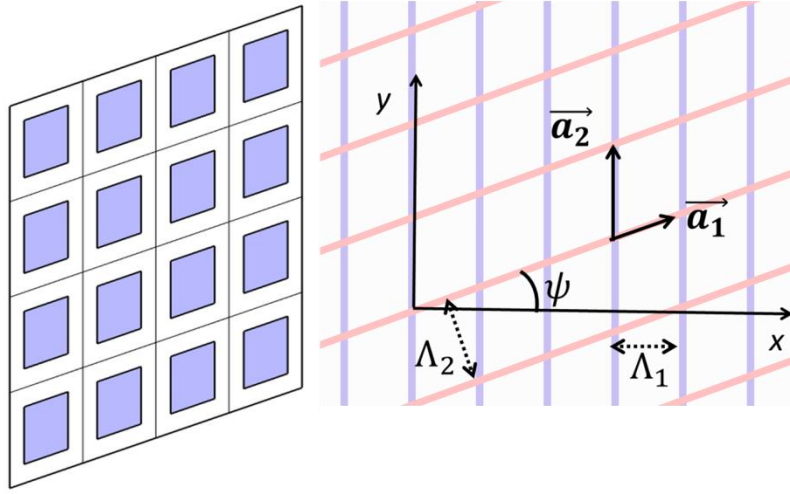

Figure 2.13 schematic for the generalization of the Vector Model

A general bidimensional periodic structure, like a tilted chessboard, is reported in Figure 2.13. The surface is invariant for every translation along any of the lattice vectors $\vec{R} = n_1\vec{a_1} + n_2\vec{a_2}$ is performed. Being $\vec{a_1}$, and $\vec{a_2}$ in reference to figure 2.13:

$$\vec{a_1} = \begin{cases} \Lambda_1 \\ \Lambda_1\tan(\psi) \\ 0 \end{cases} ; \ \vec{a_2} = \begin{cases} 0 \\ \Lambda_2\cos(\psi) \\ 0 \end{cases} \tag{2.53}$$

The reciprocal lattice vectors could be found straight forward [69] by considering:

$$\vec{g_1} = \frac{2\pi(\vec{a_2} \times \vec{e_3})}{\vec{a_1} \cdot (\vec{a_2} \times \vec{e_3})}; \ \vec{g_2} = \frac{2\pi(\vec{e_3} \times \vec{a_1})}{\vec{a_1} \cdot (\vec{a_2} \times \vec{e_3})} \tag{2.54}$$

where $\vec{e_3}$ is the unitary vector along the z-axis. This implies that the two dimensional plasmonic equations 1.33 in the grating plane x, y becomes:

$$\vec{k}_{spp} = \eta_d\vec{k}_{0;g.p.} + \begin{bmatrix} \cos(\phi) & -\sin(\phi) \\ \sin(\phi) & \cos(\phi) \end{bmatrix} (m_1\vec{g_1} + m_2\vec{g_2}) \tag{2.55}$$

This equation is satisfied when:

$$\sin(\theta) = -\rho_g \cos(\phi - \beta) \pm \sqrt{\rho_{spp}^2 - \rho_g^2 \sin^2(\phi - \beta)} \tag{2.56}$$

where $\rho_g = \frac{|m_1\vec{g_1}+m_2\vec{g_2}|}{\eta_d k_0}$; $\rho_{spp} = \frac{k_{spp}}{\eta_d k_0}$, meanwhile $\beta = \cos^{-1}\left[\frac{(m_1\vec{g_1}+m_2\vec{g_2})_x}{|m_1\vec{g_1}+m_2\vec{g_2}|}\right]$.

We can notice that the resonance has the same analytical form for one-dimensional or a bi-dimensional periodic grating is used. In fact the one - dimensional grating is described by equation 2.56 imposing m_1 or m_2 = 0. Moreover we underline that β depends only on the geometrical parameters, and not on the surface condition.

In the next chapter we will use this model to fit the plasmonic resonances obtained from the periodic nanostructured surfaces simulation. Then we will see how this method can be used to predict the sensitivity of various plasmonic configurations.

3 Simulation Results

In this chapter we will show the main results obtained by using the simulation tools previously described. First we will analyse the results we obtained by lighting a nanostructured surface in conical mounting configuration. We will start from the RCWA simulation of the one dimensional grating [70]–[72]. Then, by means of the FEM method, we will analyse two-dimensional nanostructures that can be considered as a superposition of two or three one dimensional gratings. We will also see that the SPRs resonances are well fitted by the Vector Model.

Then we will study the characterization of the SPRs in the Kretschmann configuration for flat and grating surfaces.

Moreover since the Kretschmann and grating coupling configurations excite the same surface modes, we will undercover and discuss their common features.

Finally we will study the theoretical sensitivity of the SPRs. In each case the sensitivity will be calculated by changing the refractive index of the dielectric medium, and by modeling a dielectric thin layer that covers the metal part of the interface. We will perform this analysis considering as possible variables: the wavelength, the incident angle, the polarization angle, and the azimuthal angle.

3.1 Nanostructured surfaces in conical mounting configuration

3.1.1 Grating

First of all we will study the behaviour of the grating in the conical mounting configuration by considering the zero order reflectance (R_0) and the total grating transmittance (T_{tot}). These are the experimental quantities we can measure with our experimental set up. All the grating simulations that we will show in this section are computed via the RCWA method. In reference to figure 2.10 we will use the following grating cross section parameters:

λ	Λ	f_{up}	f_{down}	h_{down}	h_{up}	h_{slab}	h_{func}	ε_{air}	ε_{Ag}	ε_{func}	ε_{poly}
635 nm	740 nm	0.45	0.3	20 nm	20 nm	35 nm	--	1	-17-0.7i	--	2.4964

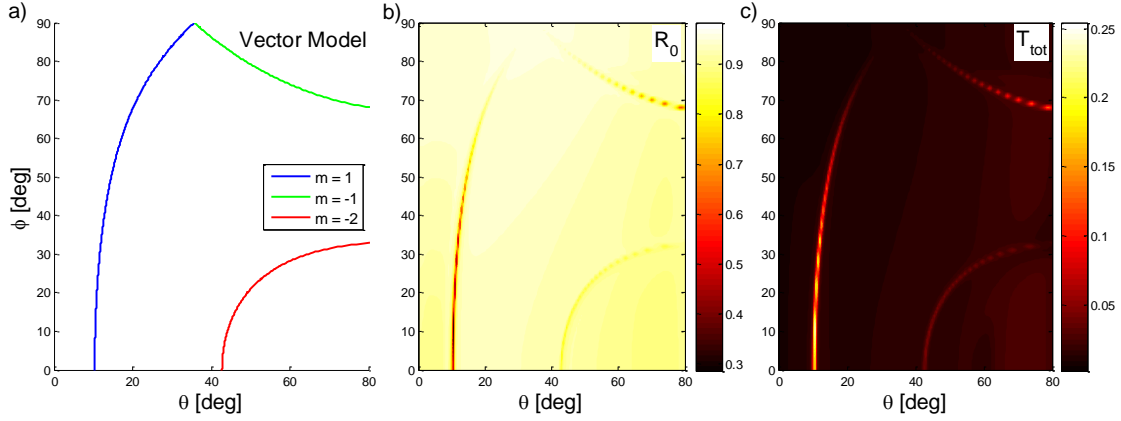**Table 3.1. Grating model parameters used in this section.**

Figure 3.1 SPRs for a unidimensional grating in conical mounting configuration: (a) pairs (θ, ϕ) calculated by using the VM, (b) R_0 and (c) T_{tot} calculated by using the RCWA method, as a function of θ and ϕ for the TM polarization mode

In figure 3.1a we report the resonance curves calculated via the vector model by using the parameters reported in table 3.1. In figure 3.2b and 3.2c we report the parameters R_0 and T_{tot} calculated by lighting the grating in the TM mode. In all these figures the calculated quantities are shown only for the positive azimuthal angles since they are symmetric respect to $\phi = 0°$ axis.

As we can see the resonances shape follows the vector model curves and they are characterized by a minima in R_0, and a maxima in T_{tot}. If a cross section at $\phi = 0°$ of the total transmittance map is considered, two maxima appear, corresponding to the SPR $m=1$ and $m=-2$, respectively. Let us call these two critical points $(\theta_{c,1}; \phi_{c,1})$ and $(\theta_{c,-2}; \phi_{c,-2})$. If we analyse a θ-cross section of the T_{tot} map for $5° < \theta < \theta_{c,1}$, T_{tot} show only a maximum at $\phi = 0°$. The value of this maximum increases while θ becomes closer to $\theta_{c,1}$ and for $\theta = \theta_{c,1}$ it reaches the highest value. If a similar cross section is considered for $\theta_{c,1} < \theta < 35.7°$ the two symmetric peaks at $\pm\phi_{r,1}$ appear. The absolute values of this resonance position $\phi_{r,1}$ increases augmenting θ, and we can also see that the peak transmittance decreases until it disappears for $\phi = 90°$. A similar behaviour of the azimuthal resonance can be noticed for the SPR $m=-2$; if a θ-cross section of the map for $35.7° < \theta < \theta_{c,2}$ the azimuthal transmittance has three maxima two a $\pm\phi_{r,-1}$ due to the excitation of the SPR $m=-1$, and one at $\phi = 0°$ due to the $m=-2$ SPR. Considering now only the resonances due to $m=-2$, if a cross section of the map is taken for $\theta > \theta_{c,2}$, two azimuthal resonances $\pm\phi_{r,-2}$ appear.

By comparing the R_0 map with the T_{tot} map, and in particular the R_0 minima and T_{tot} maxima, the plasmonic resonances present the same behaviour. Nevertheless, fixed θ, the azimuthal resonance angle ϕ_r, found as a minimum of the reflectance, is not exactly the found as a maximum of the transmittance [73], [74]. We report in table 3.2 the azimuthal resonance angles found through R_0 and T_{tot} for the SPR $m=1$ and $m=-2$.

ϕ_r	SPR $m=1$; $\theta = 10.5°$	SPR $m=-2$; $\theta = 43.0°$
R_0	10.55°	4.00°
T_{tot}	10.30°	4.60°

Table 3.2 Azimuthal resonance position found by using R_0 and T_{tot} parameters for the SPR $m=1$ and $m=-2$.

As we can see from table 3.2 for the SPR m=1 the resonance angle found by using the R_0 parameter is 0.25° greater than the one found considering the T_{tot} parameter. Conversely for the SPR m=-2 ϕ_r calculated through R_0 is 0.6° lower than ϕ_r calculated by using T_{tot}.
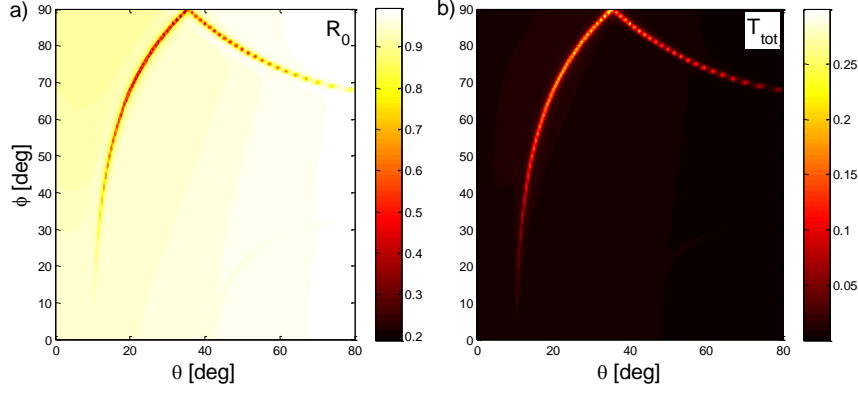

Figure 3.2: (a) R$_0$ and (b) T$_{tot}$ calculated by using the RCWA method as a function of θ and ϕ for the TE polarization mode

In figure 3.2a and 3.2b we report the parameters R_0 and T_{tot} calculated for the grating lighted in the TE mode as a function of θ and ϕ, respectively. As for the TM case, the reported maps are symmetric with respect to $\phi = 0°$ axis.

Also in this case the resonances follow the vector model and increase their amplitude with the increasing their azimuthal angle, being strongest at $\phi = 90°$. This behaviour is the opposite respect to the resonances found in the TM mode. The SPR m=-2 resonance weakly excited through this polarization mode, since it is confined for $|\phi| < 40°$; in fact it is difficult to identify it by looking at figure 3.2.

In conclusion, the plasmonic resonances for the unidimensional grating case appear as maxima (minima) if T_{tot} (R_0) parameter is plotted as a function of θ and ϕ. The resonances shape follows the curves predicted by using the Vector Model, and they appear as a sort of parabolic curve $\theta(\phi)$. This ⊂-shaped curves follow the analytical equation 2.56 of the vector model. The critical points of the curves, i.e. the parabola vertexes, are represented by $(\theta_{c,1};\ 0)$ and $(\theta_{c,-2};\ 0)$ since the azimuthal angle β of the VM is geometrically forced to 0° (eq. 2.56, with m_2=0). For each resonance, the critical point strongly affects the azimuthal resonance behaviour. One single azimuthal resonance is found at ϕ= 0° if $\theta \leq \theta_c$ meanwhile two symmetric azimuthal resonance can be identified for $\theta > \theta_c$.

In the next section we will analyse two dimensional crossed gratings. They will produce resonances described by the same analytical curves found for the one-dimensional grating case, but with a critical point $\phi_c \neq 0$.

3.1.2 Two-dimensional nanostructures

The first Two-dimensional nanostructure we simulated through the FEM method is the one showed in figure 3.3b. It is composed by two unidimensional gratings of 740 nm period rotated by an angle of 20°. The nanostructure is therefore similar to an equilateral rhombus. The grey areas describe the silver continuous layer which separates the substrate medium (glass, $\eta_d = 1.5$) from the upper medium (air, $\eta_d = 1$).The silver film thickness is set to 45 nm and the nanostructure amplitude is 20 nm. We simulated the nanostructure with a TM polarized light having a wavelength of 635 nm.

In figure 3.3a we report the total transmittance of the nanostructure and the position of the resonances calculated by using the vector model (white dashed line). As we can see all the different resonances due to the different SPR excitation orders, which in this case are described by the two coupling number m_1, and m_2, are well reproduced in the region near the critical point $(\theta_c; \beta)$. When two different orders should be excited for the same (θ, ϕ), some plasmonics bandgap occurs and huge discontinuities in the transmittance map can be noted, such as for θ=16° and ϕ= -55°.
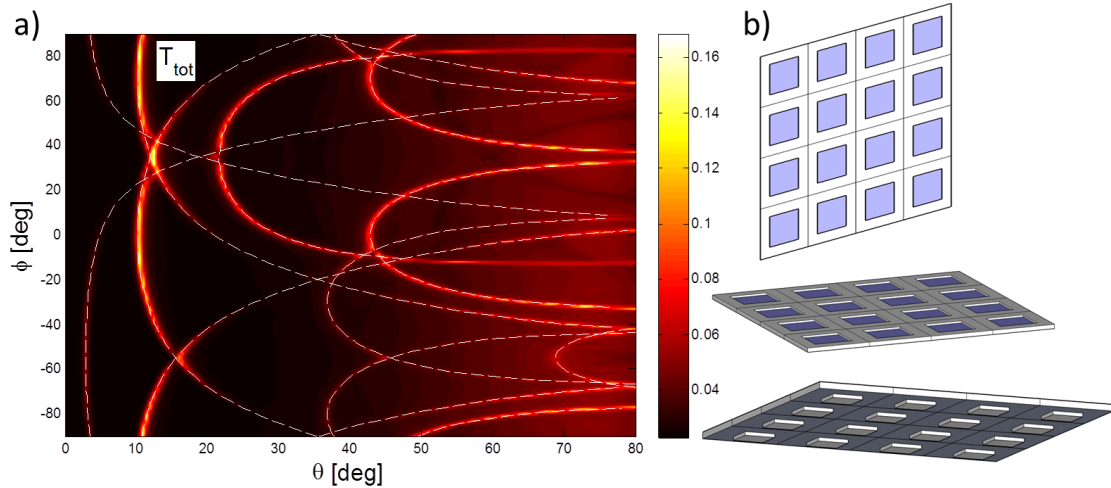

Figure 3.3 (a) T$_{tot}$ map as a function of θ and ϕ calculated for the bi-dimensional nanostructured surfaces by using a 635 nm light in the TM polarization mode. (b) schematic of the nanostructured surface.

As we can see the VM well reproduces the resonances calculated by means of the FEM method. Hence the VM is the quickest and accurate instrument to use for calculate the angular position of the SPR, when resonance shape and intensity are not required parameters. Also we can see that the shape of the resonance does not change significantly if a more complex structure than the one-dimensional grating, is used; we always obtain ⊂-shaped curves that follow the analytical equation 2.56 of the vector model.

In the previous example, we compared the T$_{tot}$ parameter calculated by the FEM method with the curves produced by the VM. We found a good agreement between the two simulation methods, being the transmittance maxima well fitted by the VM analytical curves. Nevertheless the SPRs produced considering the previous case have a maximum coupling order $\left|m_{1,2}\right|_{max}$=2. Hereafter we will study what happens when a coupling order up to $\left|m_{1,2}\right|_{max}$=6 could, in theory,

be excited and how the structure inside the periodic cell can affect the resonance coupling strength.

In order to depict this aspect we calculated the transmittance map produced by the nanostructures reported in figure 3.4
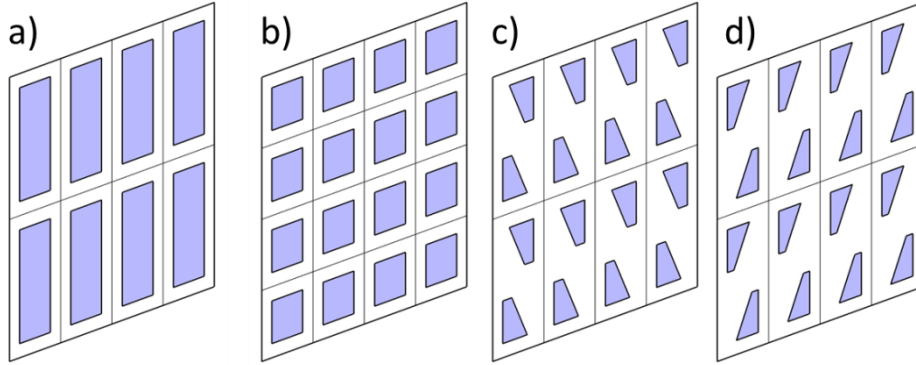

Figure 3.4 Different nanostructured surfaces implemented with the FEM method

Figure 3.4a represents the base bi-dimensional periodic structure we considered. In this case we use two different periods being the shorter one 740 nm, meanwhile the longest one equals 2*1.3*740 nm. The other structures reported (3.4b, 3.4c, and 3.4d) are obtained by adding another grating to the first nanostructure. For the structure reported in figure 3.4b, a grating is added in the middle of the periodic cell halving the longest period that becomes in this case 1.3*740 nm. In figure 3.4c we added a grating parallel to the diagonal that goes from the upper left corner down to the lower right corner. The opposite diagonal were used to add the grating as it is reported in figure 3.4d. Like in the previous case the total film thickness was set to 45 nm and the height of the nanostructure to 20 nm.

In figure 3.5 we report the T_{tot} maps found for the four different nanostructures (a, b, c, d) shown in figure 3.4 as a function of (θ, ϕ) calculated using a 635 nm light in TM polarization mode. White circles refers to the critical points $(\theta_c; \beta)$ we found by applying the VM to the basic periodic cell described in figure 3.4a, since this is the cell that could be considered as the unitary periodic cell for all the four cases here considered. As we can see from figure 3.5a, for the simplest model considered, not all the critical points correspond to a vertex for a transmittance ⊂-shaped resonance as conversely happens for the case reported in figure 3.3a. This behaviour is typical also for the others nanostructured surfaces considered.
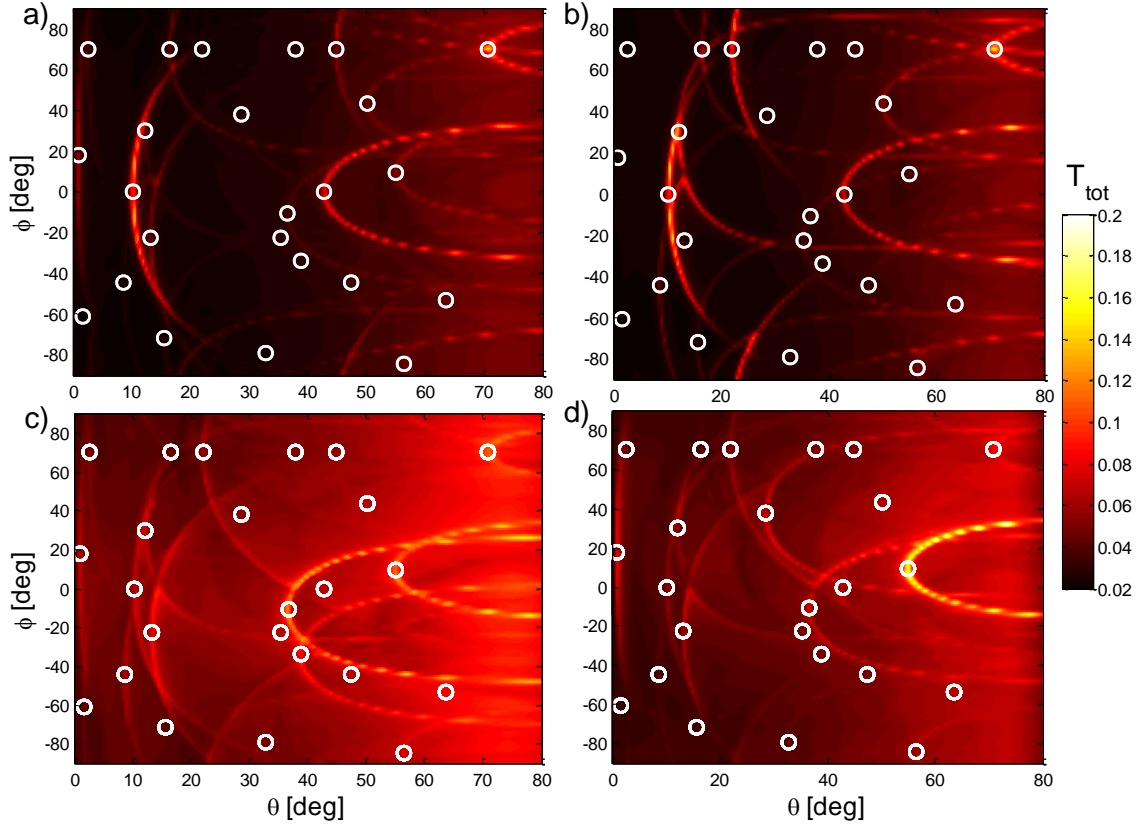
Figure 3.5 T$_{tot}$ calculated for the nanostructured surfaces showed in Figure 3.4 the association follows the respective letters. The white circles refers to the critical points (θ_c; β) calculated by using the VM.

The total transmittance map noticeably changes If some geometrical features are added inside the periodic cell, such as another grating with a fixed direction. This boosts some excitation orders and weakens some others, e.g. the resonance that occurs at θ_c=42.9° and ϕ_c=0° of figure 3.5, corresponding to m_1=2; m_2=0, is stronger for the (a) and (b) geometries then it is weakened by the (d) geometry and it disappears in the (c) geometry. There are also some resonances that never appear such as the one at θ_c=37.9°, ϕ_c=70° which in this case corresponds to the excitation order m_1=0; m_2=5, or the one at θ_c=63.6°, ϕ_c=-53.4° corresponding to m_1=2; m_2=5. Where m_1 and m_2 were calculated by considering the structure of figure 3.4a as the unitary cell.

Nevertheless regarding the geometry (b) if we use the smallest possible periodic cell for the VM calculations, all the resonance that appear are well fitted. In fact by considering the smallest periodic cells the maximum excitation order allowed by the vector model is $\left|m_{1,2}\right|_{max}$=2 as it happens in the case of figure 3.3a

In this study we learn that also complicated structures show the usual plasmonic resonance effect described, If present, by the vector model analytical equation 2.56. The change of the periodic cell geometrical features can lead to an enhancement of certain resonances whose shape and intensity can be evaluate through the FEM method.

3.2   Kretschmann configuration

Among all the configurations for SPP excitation, the Kretschmann one is the most used and it is also implemented in numerous commercial instruments (section 1.2.1). In this configuration SPPs are excited by lighting the metal/dielectric interface from an high refractive medium, i.e. a glass prism, see figure 3.6. When the condition of total internal reflection is satisfied, an evanescent wave penetrates the metallic film and it couples with the SPP at the metal/air interface, producing the resonance.

In this case no rays are transmitted since we are in total internal reflection (TIR) condition and the resonance can be only monitored by looking at the properties of the zero order reflected ray; i.e. the reflectance as a function of the light incident angle or wavelength is measured. Conversely when a grating structured surfaces is mounted in this configuration some rays could be transmitted since they coupled with the grating momentum. In this case the plasmonic equation that needs to be satisfied is eq. 1.33, here reported:

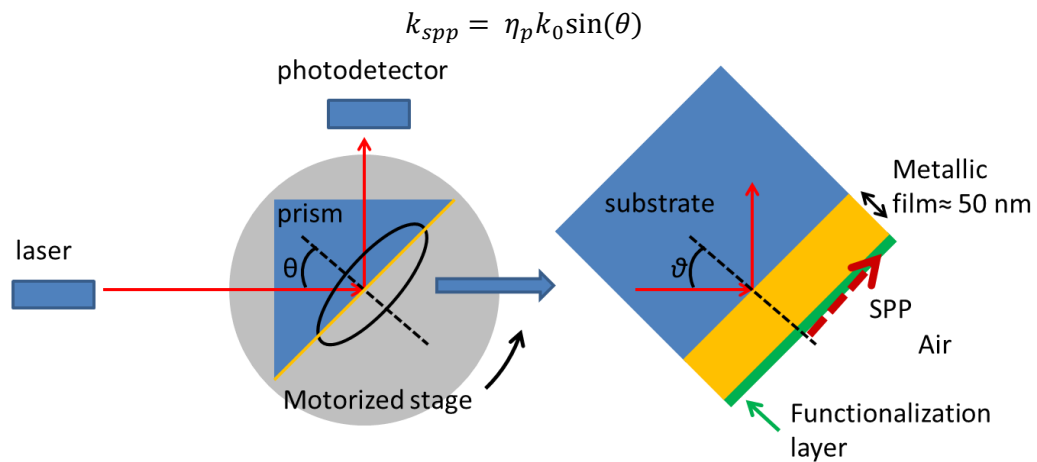$$k_{spp} = \eta_p k_0 \sin(\theta) \qquad (3.1)$$

Figure 3.6 Schematic of the Kretschmann configuration

3.2.1 Flat surfaces

We adopted the RCWA method to simulate the Kretschmann resonances, but we implemented a simplified version of it, i.e. the one reported in the first part of Moharam work [52]. For the characterization of this type of resonance we used a two layers system. The first layer represents the silver film (yellow layer in Fig 3.6) and it is in contact with the polycarbonate substrate. The second layer is placed between the silver metallic film and the air buffer (green layer in Fig 3.7). This layer simulates the presence of a functionalization layer that will account for the biological modification of the surface. The light, obviously, incomes from the polycarbonate substrate.

Initially we simulated the R_0 map as a function of the incoming light incident angle and wavelength. The parameters used in the simulation are:

η_p=1.58	η_{air}=1	η_{func}=1	d_{Ag}= 50 nm	d_{func}= 1 nm

Table 3.3 physical parameters used in the simulations

where η_p is the polycarbonate refractive index which was assumed to be constant for all the light wavelenght. Conversely the silver dielectric permittivity was considered as a function of the wevelenght by using the values measured by Rakić [75].

We report in figure 3.7a R_0 as a function of the incident light wavelength and the incident angle found for a flat silver surface lighted in the TM mode. The SPR is clearly seen as the dark band inside the map that represent the reflectance minima. In figure 3.8b we report R_0 as a function of θ for λ = 633 nm calculated with the same previous conditions. Here the resonance is a represented by a sharp minimum in the R_0 parameter. The experimental characterization of this minimum will be discussed in section 4.2.2
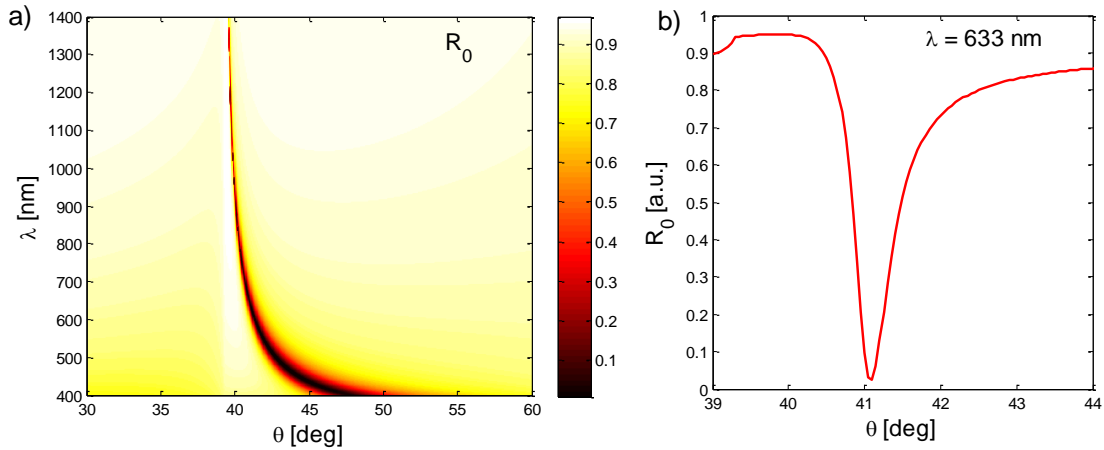

Figure 3.7 R_0 parameter calculated as a function of θ and λ. (b) R_0 as a function of θ for λ=633 nm. Both figures were calculated for a flat silver surfaces lighted in the Kretschmann configuration with TM polarized light.

3.2.2 Grating surfaces

In the previous section we saw what happens when a flat metal/dielectric interface is lighted in Kretschmann configuration. Now we want to study what happens when instead of flat surfaces we light a unidimensional nanostructured surface. This field has been studied in other works in order to understand the excitation of the SPP in the upper and lower interface [76], [77], and to enhance the Kretschmann sensitivity [78], [79]. Nevertheless all these studies refer to the condition where the grating is oriented perpendicular to the scattering plane i.e. ϕ=0°. Here we will study the complete system as a function of the θ and ϕ angles and we will show what happens at the nanostructured metal/substrate interface and at the metal/dielectric one.

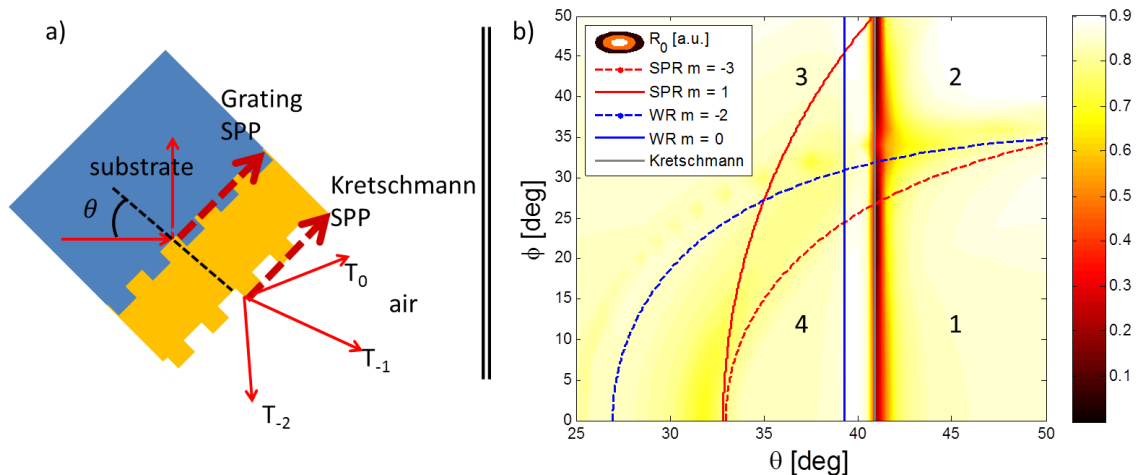**Figure 3.8 (a) Schematic of the excitation of SPP in the Kretschmann configuration using a nanostructured surface. (b) R$_0$ as a function of θ and ϕ calculated using a unidimensional grating lighted in a Kretschmann configuration by using a 633 nm light wavelength in TM polarization mode.**

We schematized the results in figure 3.8a. The light was incoming from the grating polycarbonate substrate and it was reflected from the silver yellow layer. The intensity of this reflected ray is reported as a function of θ and ϕ in figure 3.8b, and were calculated assuming that the grating is lighted with a 633 nm laser and in TM polarization mode. The grating parameters were the ones reported in table 3.1. The Kretschmann plasmonic excitation corresponds to the dark vertical band in figure 3.9b, fitted by the grey line. It relates to the excitation of the SPP at the metal/air interface and it is independent from the azimuthal angle since its excitation follows eq. 3.1.

At the polycarbonate/metal interface another SPP can be excite. This coupling could be related to the m=-3 (red dashed line) or m=1 (red continuous line) orders. Also in these cases the SPP excitation is represented by the classical vector model (eq. 2.56) considering the polycarbonate refractive index η_d=1.58. As we can see, from figure 3.8b, shallow minima are present along the red dashed line. Hence the weak coupling of the SPP at this interface should follow the SPR m=-3 order. We measured these plasmonic resonances in section 4.2.3 and we found that, despite these simulations results, the most pronounced SPP excitation order is the m=1 one.

The other two blue lines reported in figure 3.8b are related to the Wood-Rayleigh anomalies. These anomalies happen when the z-component of a diffracted ray becomes zero and, therefore, it is related to the number of grating transmitted rays. These resonances divide the plane (θ, ϕ) in four regions, each one with a specific number of diffracted rays, as reported in table 3.4:

Region	Transmitted ray.
1	T_{-1}, T_{-2}
2	T_{-1}
3	T_0, T_{-1},
4	T_0, T_{-1} T_{-2}

Table 3.4 Rays transmitted by the grating in each numbered region as reported in Figure 3.8b

As we can see the T_{-1} ray is always present, the T_{-2} ray is present under the dashed blue line while the T_0 order is present at the left of the vertical blue line. The T_{-1} and T_{-2} rays are directly related to the grating presence. They have a transmittance maximum when the Kretschmann Plasmon is fully excited. Moreover their output angles pairs $(\theta_{out}, \phi_{out})$ at the resonance, are the same angles that must be used to excite the SPP at the metal/air interface if the grating is lighted from the air in a conical mounting configuration. This fact was already pointed out in the work of Park [73], [80], [81] for the special case of $\phi = \phi_{out} = 0°$.

3.3   Relationship between the Kretschmann and grating configurations

The main difference between the Kretschmann and the grating configuration is the excitation medium. In the grating configuration the light incomes from the upper dielectric medium while in the Kretschmann configuration it incomes from an high refractive index medium. Previously, we showed that if the flat interface of the Kretschmann configuration is replaced with a nanostructured surface there are also some transmitted rays that propagate in the dielectric medium. When the Kretschmann plasmon is excited, these rays are transmitted with an angle respect to the normal which is the same one that must be used to excite the SPP if the same nanostructured surface is lighted in conical configuration [74].

Nevertheless the picture is not yet complete; here we will explain what happen to the grating transmitted rays in the substrate when the grating is lighted in the conical configuration. We will see that among all the four transmitted rays, propagating in the grating substrate, there is only one that carries the major information about the SPR transmittance. At the maximum of the excitation this ray propagates into the substrate with an angle that is equal to the one that must be used to excite the SPP in the Kretschmann configuration [74]. Here we will analyse two different cases: the transmitted ray when SPR $m=1$ in air is excited (figure 3.9 and following), and when SPR $m=-2$ in water is excited (figure 3.10 and following).

We have already seen that in order to excite the SPP through a grating in the conical mounting configuration the equation 2.56 must be satisfied. The equation is reported here for the simply case of a unidimensional grating:

$$sin(\theta_{in}) = \frac{-mGcos(\phi_{in}) \pm \sqrt{-m^2G^2\sin^2(\phi_{in}) + Re^2(k_{spp})}}{k_0\eta_d} \tag{3.2}$$

where $k_0 = 2\pi/\lambda$ is the vacuum light momentum and λ the vacuum wavelength, η_d is the refraction index of the dielectric medium (air or water), $k_{spp} = k_0\sqrt{\frac{\varepsilon_d\varepsilon_m}{\varepsilon_d+\varepsilon_m}}$ is the modulus of the SPP coupling constant, $\varepsilon_d = \eta_d{}^2$ is the relative dielectric constant of the dielectric medium and ε_m is the metal dielectric constant, $G = 2\pi/\Lambda$, and Λ is the grating period. We add the subscript in since we want to underline that these are the light incident angles in conical configuration when the light propagates in the upper medium.

The output angle pair $(\theta_{out,n}, \phi_{out,n})$ of the transmitted ray could be calculated through the RCWA since their momenta components are:

$$\begin{cases} k_{x,n} = k_o[\eta_d\sin(\theta)\cos(\phi) + n(\lambda/\Lambda)] \\ k_y = k_o\eta_d\sin(\theta)\sin(\phi) \\ k_{z,n,II} = \sqrt{(k_o\eta_p)^2 - k_{x,n}{}^2 - k_y{}^2} \end{cases} \tag{3.3}$$

Where η_p is the refraction index of the polycarbonate grating substrate, and n is the subscript that corresponds to the Rayleigh - Floquet expansion order of the diffracted ray. The output angle pairs is therefore:

$$\theta_{out,n} = \tan^{-1}\left(\sqrt{k_{x,n}{}^2 + k_y{}^2}/k_{z,n,II}\right); \ \phi_{out,n} = \tan^{-1}(k_y/k_{x,n}) \qquad (3.4)$$

In the two cases considered: air, and water, four transmitted rays T_{-2}, T_{-1}, T_0, T_1 are always present.
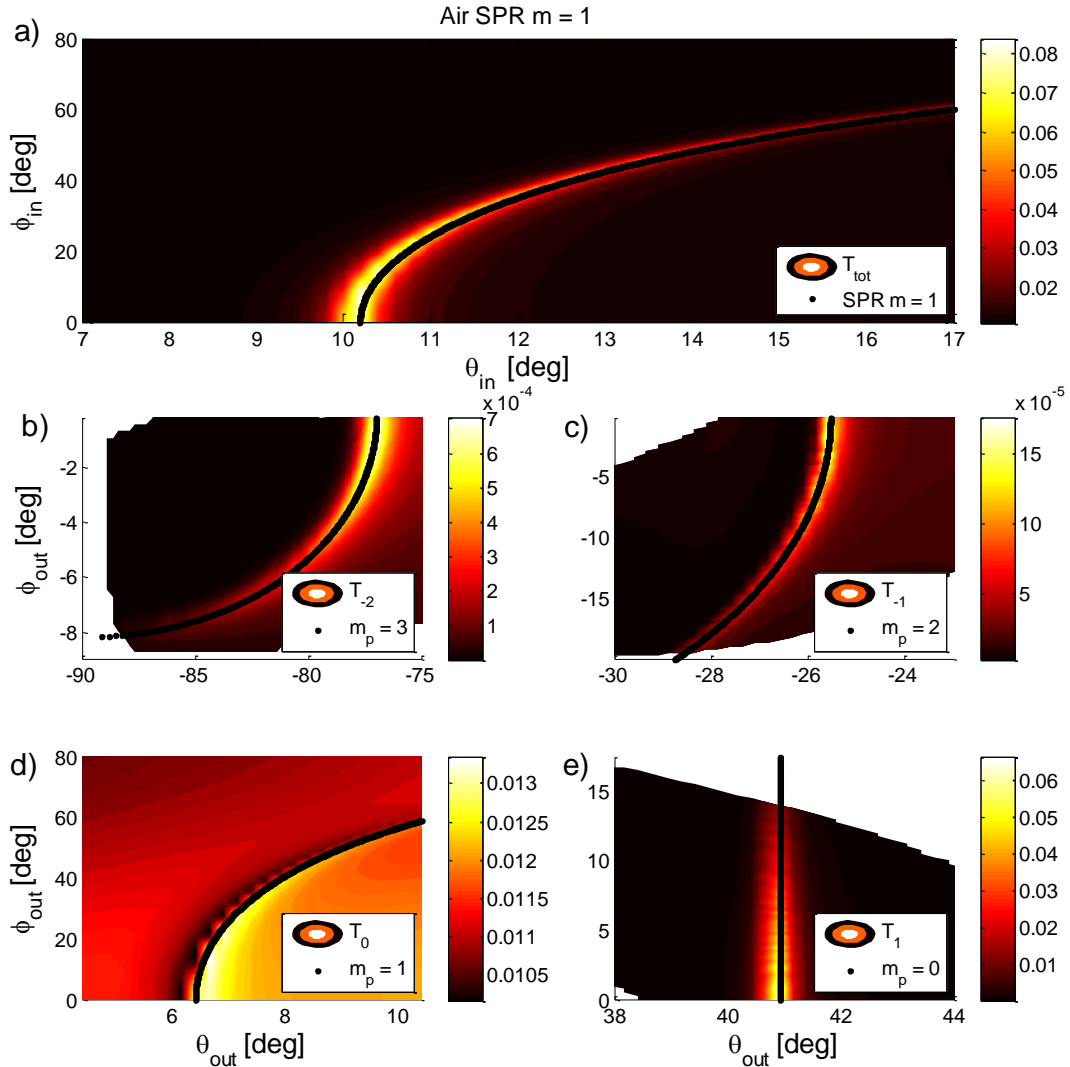

Figure 3.9 (a) T_{tot} as a function of θ_{in} ϕ_{in}. (b) T_{-2}, (c) T_{-1}, (d) T_0, (e) T_1 as a function of θ_{out} ϕ_{out}, calculated for a trapezoidal grating lighted in TM mode for the SPR $m=1$ in air. The black lines refer to the VM calculations

In figure 3.9a we report the T_{tot} as a function of θ_{in} and ϕ_{in}. Here the same resonance of figure 3.1c can be seen and also in this case it is well fitted from the vector model considering $m=1$ as the coupling constant. The transmittance values are slightly different because we use a trapezoidal grating cross section. In reference to figure 2.8 the parameters used are reported in table 3.5.

λ	Λ	f_{up}	f_{down}	h	d_{Ag}	d_{func}	ε_{air}	ε_{Ag}	ε_{func}	ε_{poly}
635 nm	740 nm	0.75	0.93	20 nm	58 nm	--	1	-17-0.7i	--	2.4964

Table 3.5 Parameters used in the trapezoidal grating simulation

The other four figures 3.9b, 3.9c, 3.9d, and 3.9e show the ray transmittance T_{-2}, T_{-1}, T_0, and T_1 plotted as a function of their output angles $(\theta_{out}, \phi_{out})$, respectively. As we can see in all these

four figures a resonance appears and it is well fitted by the black dotted curves. These curves represents the solution of this equation:

$$sin(\theta_{out}) = \frac{-m_p G cos(\phi_{out}) \pm \sqrt{-m_p^2 G^2 \sin^2(\phi_{out}) + Re^2(k_{spp})}}{k_0 \eta_p} \qquad (3.5)$$

which is similar to the equation 3.2 with the exception that we substitute η_d with η_p, and m with m_p (k_{spp} remains the same). We will refer to m_p calling it: the decoupling constant.

The maps reported in figure 3.9 show that every ray carries a different part of the SPR information. We can see that for T$_{-2}$, and T$_{-1}$ the resonance is represented by a transmission enhancement and it is well fitted by the decoupling constant m_p=3 and m_p=2, respectively. Nevertheless their contribution to the total transmittance is negligible since their values reach a maximum of about 7×10^{-4} a.u. while the T$_{tot}$ maximum is slightly greater than 0.08 a.u.

The T$_0$ ray follows the Snell law and its resonance it is well fitted by using the decoupling order m_p= 1. Its resonance is not represented by an enhancement in the transmittance but it has a step like shape. The value of T$_0$ varies in a narrow range of values from 0.013 a.u. to 0.016 a.u. and regarding the T$_{tot}$ map this values represent the baseline of the resonance. Further we will refer to this ray as "the baseline ray".

The most interesting output ray is the T$_1$ ray. As we can see its transmittance values go from 0 a.u. to a maximum of 0.065 a.u.. This means that at the resonance it carries about the 87 % of the total transmittance. As we can see from figure 3.9e the resonance is represented by a maximum well fitted by the decoupling constant m_p= 0 and it is independent from ϕ_{out}. The angle θ_{out} where this resonance happens is the same one that must be used to excite the SPP at the silver/air interface if the surface is mounted in Kretschmann configuration. We will refer to this ray as "the Kretschmann ray".

Figure 3.10 reports the behaviour the SPR m=-2 in water (η_d= 1.333).In figure 3.10a we report the T$_{tot}$ map as a function of θ_{in} and ϕ_{in} while the figures 3.10b, 3.10c, 3.10d, and 3.10e report the transmittance of the four diffracted rays T$_{-2}$, T$_{-1}$, T$_0$, and T$_1$ as a function of their output angles (θ_{out}, ϕ_{out}), respectively. All these maps were calculated by using the previously described trapezoidal grating parameters (table 3.5). As expected the resonance presents in the T$_{tot}$ map is well fitted by the VM considering m=-2 as the SPP coupling order, proving the effectiveness of our analysis if water is used as dielectric medium.

The rays behaviour is very similar to the SPR m=1 in air, previouslydescribed. This time the role of the Kretschmann ray is played by T$_{-2}$ as can be seen from figure 3.10b. Its resonance as a function of the output angles is ϕ_{out}-independent and it is well fitted by the decoupling constant m_p= 0. As previously seen at the resonance this ray carries the 60 % of the total transmittance. Its output incident angle is the same that must be used in the Kretschmann configuration for exciting the SPP at the silver/water interface. Again T$_0$ assumes the role of the baseline ray since its transmittance is comprised between 0.013a.u. and 0.016 a.u. and it is almost constant for all the considered angles (figure 3.10d). Its shallow resonance is fitted here by using m_p=-2. The other two rays, T$_{-1}$, and T$_1$ become the negligible rays since their

transmittance reaches a value of 2.2×10^{-4} a.u. meanwhile the T_{tot} maximum is slightly greater than 0.06 a.u.. Their resonances are fitted by using m_p=-1 and m_p=-3, respectively.
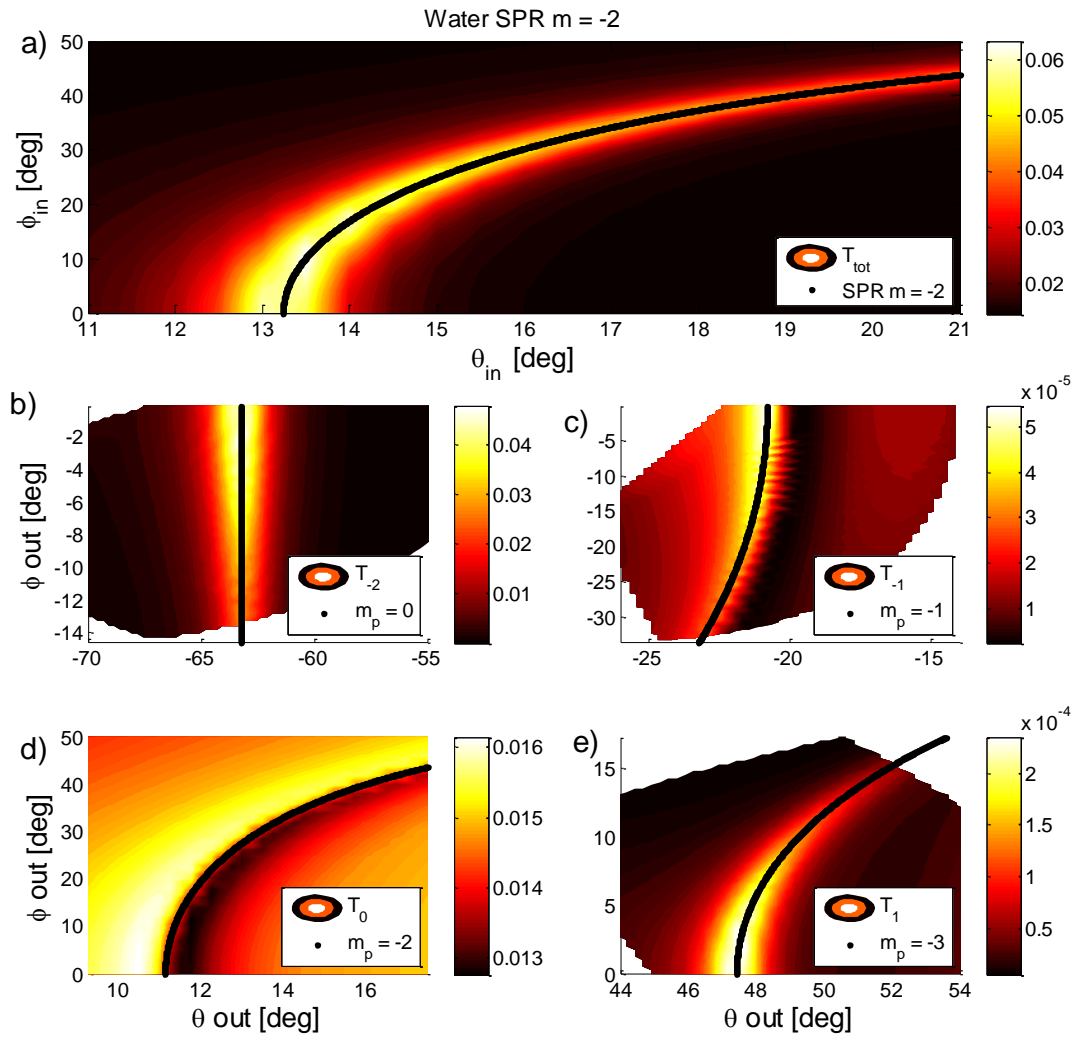

Figure 3.10 (a) T_{tot} as a function of θ_{in} ϕ_{in}. (b) T_{-2}, (c) T_{-1}, (d) T_0, (e) T_1 as a function of θ_{out} ϕ_{out} , calculated for a trapezoidal grating lighted in TM mode for the SPR m=-2 in water. The black lines refer to the VM calculations

The analysis we performed here can be summarized in the following table for the SPR m=1 and SPR m=-2, and it is valid for every dielectric medium in contact with the metal layer:

	SPP $m = 1$		SPP $m = -2$	
n	m_p	DR	m_p	DR
1	0	k	-3	--
0	1	b	-2	b
-1	2	--	-1	--
-2	3	--	0	k

Table 3.6 role of the n-th Rayleigh Floquet transmitted rays for the m =1 and m = -2 SPP coupling orders.

Table 3.6 summarizes the relation between the n-th diffracted order and the decoupling constant m_p we previously analyzed for the SPP excitation m=1 at the silver/air interface and for the SPP m=-2 at the silver/water interface. Among all the transmitted rays, the Kretschmann ray (mark in the table using "k") carries most of the transmittance at the resonance condition. T_0 is

the other important transmitted ray that influences the baseline transmittance value (has been indicated with the "b"). The other two rays can be neglected due to the fact that their transmittance is two orders of magnitude smaller respect to the transmittance carried by "k" and "b" rays and they are marked in table with "--".

The results reported in this table can be extended for other coupling orders but the main features remains the same: the baseline ray follows the Snell law and carries the baseline information having a shallow imprint of the resonance, meanwhile the Kretschmann ray carries the greater part of the resonance information. In order to sense the transmittance of this ray two possible methods could be experimentally pursued. In the first one the ray must be extracted from the grating substrate by using an optically matched prism and then analyzed by a light detector. In the second one optical medium continuity between the substrate and the detector must be ensure. If these solutions are not implemented the Kretschmann ray will undergo to TIR and it will not be sensed, losing the greater part of the SPR information. If this is the case the only ray that will be sensed is the baseline one; nevertheless the resonance can still be monitored as in Hiller's work [82], [83].

3.4   Simulated sensitivity

In this section we will analyse how the SPR shifts can be exploited for sensing purpose in different configurations. For each configuration we will see how these shifts are affected by a dielectric refractive index (η_d) increasing from 1 RIU to 1.02 RIU in step of 0.001 RIU. We will also see how different thicknesses of a dielectric layer affect the resonance. Usually this dielectric layer is used to simulate the presence of an organic layer (molecules, proteins, or antibodies). We will simulate this functionalization layer by assuming that it is formed by a dielectric having a refractive index of 1.5 RIU [20], [82], [84]. Its thickness will be varied from 0 nm to 10 nm in step of 0.5 nm.

Initially we will consider the wavelength and incident angle sensitivity for both the grating (ϕ=0°) and Kretschmann configurations [16]. In the grating case we will also analyse how an azimuthal rotation of the grating affect the θ-sensitivity. In particular we will recall the azimuthal rotated method introduced by Romanato [85]–[88], but we will also point out that an enhancement in the θ-sensitivity can be obtained exploiting the plasmonic excitation when the resonance curves are almost parallel to the θ-axis, i.e. for θ>70° in figure 3.1.

Next, we will analyse the polarization sensitivity in the grating configuration applying it to the case reported by Romanato [28], [89], [90] and to a condition adapts to our experimental constrictions (light wavelength and grating geometry). Nevertheless we will see that the two cases reach the same polarization sensitivity values.

Finally, we will introduce the azimuthal sensitivity which is one of the main parameters developed in this work [91]. We will see that this sensitivity behaves like the double deep incident angle sensitivity. Next we will improve this parameter by optimizing the shape of the SPR curves.

For all the grating simulations we will use the digital grating cross section with the parameters reported in table 3.1, meanwhile for the Kretschmann configurations we will use the parameters of table 3.3. In all the figures reported seven different colours (from dark blue to brown) will reproduce the curves we found for the different functionalization parameters. The colours will refer to η_d starting from 1.000 to 1.018 in step of 0.003 RIU if the buffer refractive index is changed. If the functionalization study is performed the colours will refer to the functionalization thickness going from 0 nm to 9 nm increasing in step of 0.15 nm.
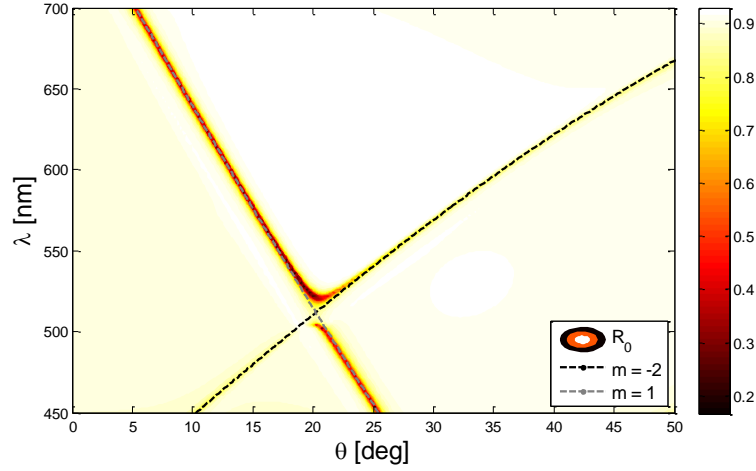
3.4.1   Wavelength sensitivity

Grating configuration:

Figure 3.11 R$_0$ map as a function of θ and λ calculated for ϕ = 0° lighting a grating in TM polarization mode. Black and grey dashed curves refers to the VM calculation for m=-2 and m=1, respectively.

In figure 3.11 we report the R$_0$ map as a function of θ and λ calculated for ϕ=0° lighting the grating with a TM polarized light. As we can see there are two intersecting dark bands. The one marked with the black dashed line refers to the SPR m=-2 and the one marked with the grey dashed line refers to the SPR m =1. We can see that, when the two resonance cross each other, a plasmonic bandgap appears similarly to what happens in the work of Alleyne [78]. Now we will fix θ = 14° and we will analyse the behaviour of the m=1 SPR. In particular we will see what happens to the plasmonic resonance when the dielectric medium refractive index η_d (see figure 3.12a),or the functionalization layer thickness h_{func} (see figure 3.12b), increase.
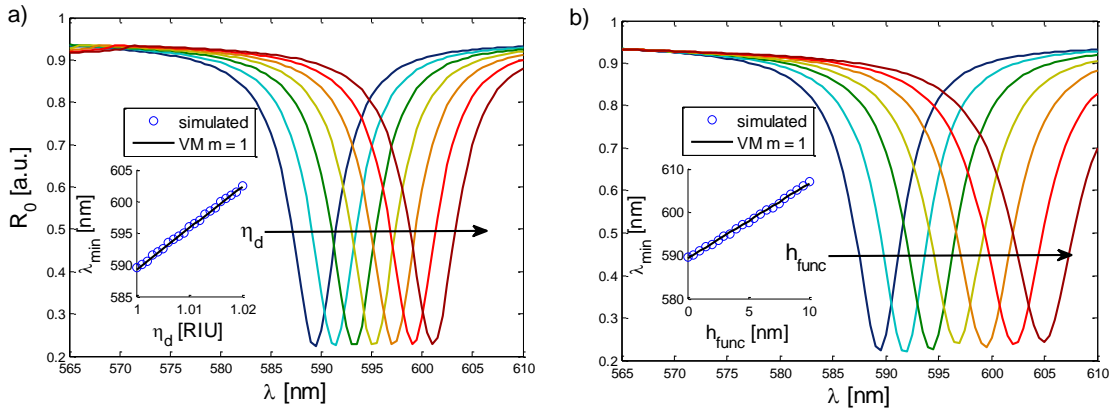

Figure 3.12 Grating configuration: (a) R$_0$ as a function of λ calculated increasing η_d, the inset shows the minimum position as a function of η_d, (b) R$_0$ as a function of λ calculated increasing h_{func}, the inset shows the minimum position as a function of h_{func}; both calculated with θ = 14°, ϕ = 0°, and in TM mode.

We report in figure 3.12a the curves R$_0$ as a function of λ for θ = 14° and ϕ = 0° in TM mode calculated for different values of η_d as specified in the introduction of this section; going from 0 RIU to 0.018 RIU in step of 0.003 RIU. The reflectance minimum shifts toward higher values of λ with the increasing of the η_d value. This shift is underline in the inset of figure 3.12a where we

report the position of the minimum as a function of η_d. The minima simulated with the RCWA model is well fitted by the VM using $m=1$ and also a good linear relation between the minimum position and the refractive index can be noted. The slope of this linear curve defined as $\partial\lambda/\partial\eta_d$ = 660 nm/RIU is the wavelength sensitivity to the buffer variations and its value is similar to the one of other grating coupling device as reported in [92]–[94].

Similarly we report in figure 3.12b the curves R_0 as a function of λ calculated for different values of h_{func} as specified in the introduction of this section. The linear correlation between the reflectance minima and the functionalization thickness is reported in the inset of figure 3.12b. The slope of this linear curve defined as $\partial\lambda/\partial h_{func}$= 1.77 nm$_\lambda$/nm$_{func}$ is the wavelength sensitivity to the functionalization thickness variations.

Also in this case we can see a good correlations between the VM $m=1$ and the values simulated by the RCWA code. In this case the relation between the two simulation methods is not well specified as in the case of the buffer variation η_d. In fact the parameter η_d could be directly inserted into the vector model, and its effect onto the plasmonic coupling k_{spp} constant is taken into account by the definition of $\varepsilon_d = \eta_d{}^2$ (eq 1.24). When we consider a functionalization layer adsorbed onto the metallic surface we cannot change the buffer refractive index η_d but we must change only the plasmonic coupling constant by changing $\varepsilon_d = \eta_{eff}{}^2$. The new defined parameters η_{eff} is the effective refractive index and it considers the modification introduced by the functionalization layer [20] since it is defined as:

$$\eta_{eff} = \eta_d + \frac{2h_{func}}{d_z}(\eta_{func} - \eta_d) \qquad (3.6)$$

where η_{func} = 1.5 RIU is the refraction index of the functionalization layer and d_z is the plasmon penetration depth inside the dielectric medium defined in equation 1.27. In each case we will consider d_z as the parameter that allow us to reproduce the RCWA simulated resonance with the Vector model.

We perform the same analysis for the SPR m = -2 taking θ = 33.5°. We found that $\partial\lambda/\partial\eta_d$=625 nm/RIU meanwhile $\partial\lambda/\partial h_{func}$= 0.9 nm$_\lambda$/nm$_{func}$, as reported in table 3.7.

Kretschmann configuration:

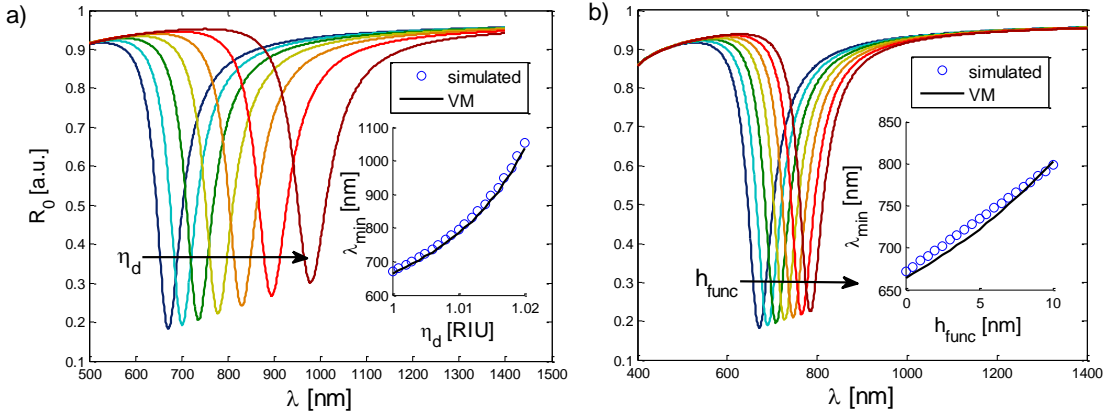**Figure 3.13 Kretschmann configuration: (a) R_0 as a function of λ calculated increasing η_d, the inset shows the minimum position as a function of η_d, (b) R_0 as a function of λ calculated increasing h_{func}, the inset shows the minimum position as a function of h_{func}; both calculated with θ = 40.8° and in TM mode.**

We perform the same analysis considering a flat surface in the Kretschmann configuration. In figure 3.13a we report different curves of R_0 as a function of λ for θ = 40.8° calculated for different values of η_d. A shift of the resonance as a function of the wavelength is clearly present and it is reported in the inset of figure3.13a. As we can see the simulated minima are well reproduced by the VM if used in the Kretschmann configuration (eq. 3.1). Nevertheless the relation between the minima position and η_d it is no longer linear and the buffer sensitivity goes from 1.0×10^5 nm/RIU to 3.9×10^5 nm/RIU.

In figure 3.13b we report the curves of R_0 as a function of λ calculated for different values of h_{func}. Again the minimum of the reflectance shifts toward higher values with h_{func} increasing, as it is reported in the inset of the figure 3.13b. In this case the RCWA simulated reflectance minima are not well reproduced by the vector model and $\partial\lambda/\partial h_{func}$= 12.7 nm$_\lambda$/nm$_{func}$. This mismatch could be ascribed to the fact the parameter d_z is considered constant in our calculations. This assumption well represent the grating case, where the total shift of the functionalization is ~15 nm, but not this one, where a huge shift of ~150 nm is registered.

	FWMH [nm]	$\dfrac{\partial\lambda}{\partial\eta_d}$ [nm/RIU]	$\dfrac{\partial\lambda}{\partial\eta_d FWMH}$ [1/RIU]	$\dfrac{\partial\lambda}{\partial h_{func}}$[nm$_\lambda$/nm$_{func}$]	$\dfrac{\partial\lambda}{\partial h_{func}FWMH}$[1/nm$_{func}$]
SPR m =1	6	660	110	1.77	0.295
SPR m = -2	3	625	208	0.9	0.3
Kretschmann	70	2.5×10^5	3570	12.7	0.18

Table 3.7 Overview of the FWMH, Sensitivity, and FOM parameters found using λ as sensing parameter.

In the table 3.7 we summarize the sensitivity parameters evaluated using the R_0 minima wavelength as sensing parameter. We also introduce the Full Width Medium Height (FWMH) parameter of the resonance. The FWMH is evaluated as the R_0 deep width at the medium of its amplitude value. Obviously, the sharper is the resonance, the smaller is the FWMH and more easy will be the SPR shift detection. This fact could be described evaluating the Figure of Merit (FOM) which is defined as the resonance sensitivity over its FWMH [16].

We can see from the table 3.7 that if only the sensitivity is considered, the Kretschmann is the best configuration since it has the highest sensitivity to η_d and h_{func}. Otherwise, if the FOM is taken into consideration, the Kretschmann configuration results the best choice for sensing η_d variations, while the grating becomes the most appropriate configuration for detecting h_{func} changes.

3.4.2 Incident angle sensitivity

In this section we will study the incident angle sensitivity of the grating and Kretschmann configurations. Exploiting the ϕ-angle in the grating configuration we will see that the θ-sensitivity parameter can be enhanced reaching very high values.

Common configuration: grating with $\phi=0°$.

In figure 3.14a, and 3.14b we report the curves of R_0 calculated as a function of θ for different values of η_d in the range 1 to 1.018 RIU, with a step of 0.003 RIU, calculated for the SPR $m=1$ and $m=-2$, respectively. In this case the grating is lighted by using $\lambda=635$ nm, $\phi=0°$ and TM polarization. As we can see the two resonances have an opposite behaviour. In fact the resonance shifts towards larger incident angles for SPR $m=1$, while it shifts towards lower angles for the SPR $m=-2$. In both cases these shifts as a function of η_d are well reproduced by the vector model (see the corresponding insets). The same resonances shift behaviour is found if the increasing of the functionalization thickness h_{func} is considered. The corresponding sensitivity parameters, the FWMH, and the FOM are reported in table 3.8.

We want to underline that, since the SPR $m=-2$ (θ_{-2}) shifts towards lower angles and the SPR $m=1$ (θ_1) shifts to higher angles, the angular difference between the two dips $\Delta\theta = \theta_{-2} - \theta_1$ varies more than the singular resonance for the same η_d variation. Effectively this method enhance the angular sensitivity by adding the sensitivity values of the two resonance, since $\partial\Delta\theta/\partial\eta_d = \partial\theta_{-2}/\partial\eta_d - \partial\theta_1/\partial\eta_d$. This very simple method is already discussed in literature by Cai [95] and it is referred as Double Dip Method (DDM).
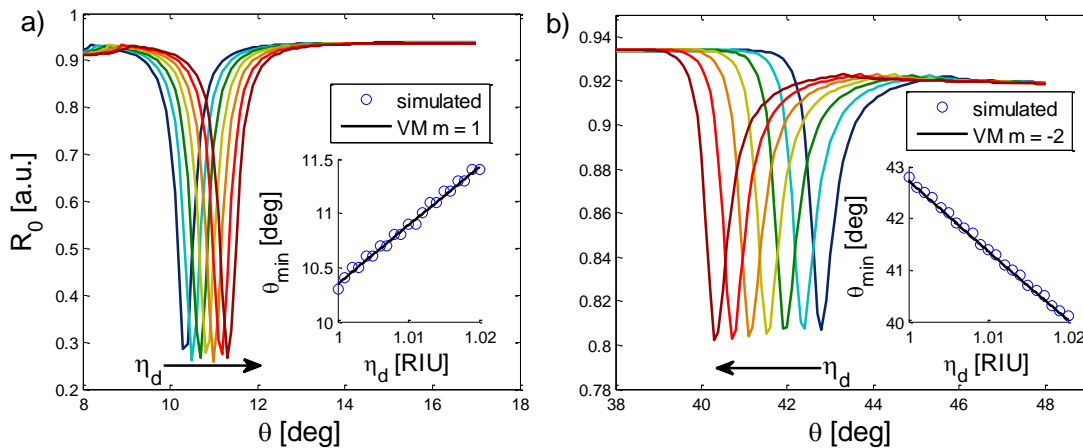

Figure 3.14 Grating configuration: (a),(b) R_0 as a function of θ calculated increasing η_d, the inset shows the minimum position as a function of η_d; both calculated with λ = 635 nm, ϕ = 0°, and in TM mode for the SPR $m=1$ and $m=-2$, respectively.
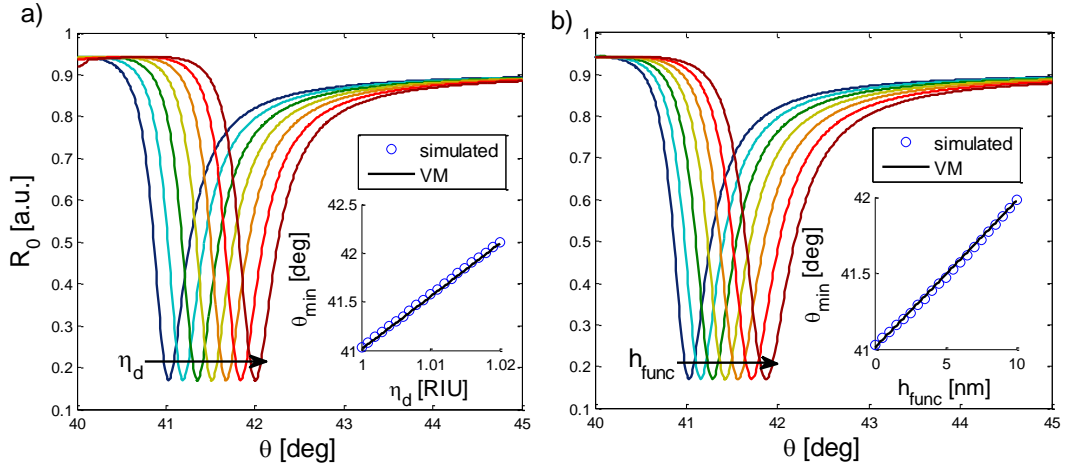
Kretschmann configuration:

Figure 3.15 Kretschmann configuration: (a) R_0 as a function of θ calculated increasing η_d, the inset shows the minimum position as a function of η_d, (b) R_0 as a function of θ calculated increasing h_{func}, the inset shows the minimum position as a function of h_{func}; both calculated with λ=633 nm and in TM mode.

In Figure 3.15a and 3.15b we report the R_0 curves as a function of θ calculated by increasing the parameter η_d and h_{func}, respectively. Both these figures were obtained by lighting the flat surface in the Kretschmann configuration a λ = 633 nm light in TM polarization mode. We can see that an increasing of the parameters η_d or h_{func} causes a resonance minimum shift towards higher incident angles likewise the m=1 SPR calculated in the grating configuration. The sensitivity we found in this configuration is reported in table 3.8 and its values are very similar to the one obtained for the SPR m=1.

Double Dip Azimuthally rotated method: grating with $\phi \neq 0°$.

Previously we exploited how the DDM can enhance the θ-sensitivity. Nevertheless another method to increase the θ-sensitivity has been studied by the Romanato [85]–[87]. Since this method is directly related to the azimuthal rotation of the grating respect to the light scattering plane we will call this method Double Dip Azimuthally Rotated Method (DDARM).
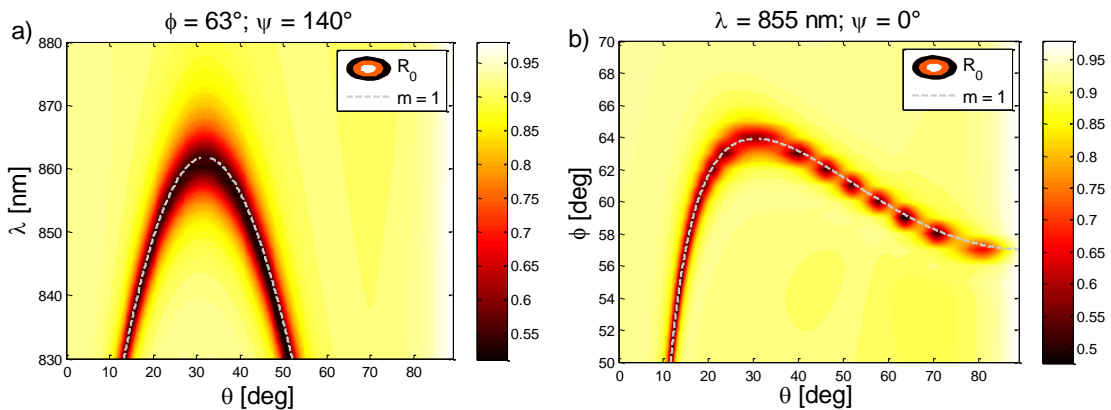

Figure 3.16 (a) R_0 as a function of θ and λ for ϕ=63° lighted with a polarization angle ψ=140°. (b) R_0 as a function of θ and ϕ lighted with λ=855 nm in TM polarization mode (ψ=0°). The grey dashed line refer to the VM calculations.

In figure 3.16a we report the R_0 map as a function of λ and θ for the grating in conical mounting configuration with ϕ=63° and a polarization angle ψ = 140°. The resonance is represented by a dark band in the map and it is well reproduced by the VM m=1 (grey dashed line). The resonance

assumes a parabolic shape of θ as a function of λ and therefore if a cross section of the parabola is considered for a fixed wavelength λ<860 nm, two R_0 minima at two different incident angles θ can be found. The light polarization angle (ψ = 140°) was chosen in order to obtain the same R_0 values of these minima.

In figure 3.16b we report the R_0 map as a function of θ and ϕ for the grating in conical mounting configuration with λ = 855 nm. Here we can see that the main difference with the map reported in figure 3.1b is that the resonance does not reach ϕ=90° and neither the coupling order changes its sign. This is due to the fact that the wavelength of the incident light is greater than the grating period (740 nm).

The sensitivity enhancement of this method relays on the fact that the entire parabolic resonance shape shifts towards higher values of lambda with the increasing of η_d or h_{func}. The effects of this shift is well explained by figure 3.17a and 3.17b where we report the curves of R_0 as a function of θ for λ=862 nm and ψ=140° obtained varying η_d and h_{func}, respectively. Since we are lighting the grating with λ>860 nm R_0 has one single dip both for η_d=1 RIU and h_{func}=0 nm. By increasing the parameter η_d or h_{func} two dips appear and then their angular difference increases.

We reported in the inset of the figures 3.17a and 3.17b the position of the minima (the ones at higher angular position) as a function of η_d and h_{func}, respectively. As we see the vector model well reproduces the resonances position, and the relation between θ_{min} and η_d (or h_{func}) is not linear. Being the sensitivity represented by the slope of these curves, it diverges approaching the condition where the two dips merge into a single one. This sensitivity behaviour as a function of the parameters η_d or h_{func} clearly depends on the fixed λ. For example, if we want to tune the high sensitivity region at higher values of η_d (h_{func}), we must increase the wavelength used. This behaviour of the resonance sensitivity typically appears when a parabolic resonance shape is exploited for sensing purpose. We will describe it in more details when we will discuss the azimuthal sensitivity.

Even if the sensitivity diverge we reported in table 3.5 the maxima an the minima values we found. In this case as FWMH we will use the width of the resonance considering its baseline values the one it assumes at θ=33°; nevertheless for a full description of the FOM problems in this parabolic resonance case the reader can look to the experimental results in section 4.3.
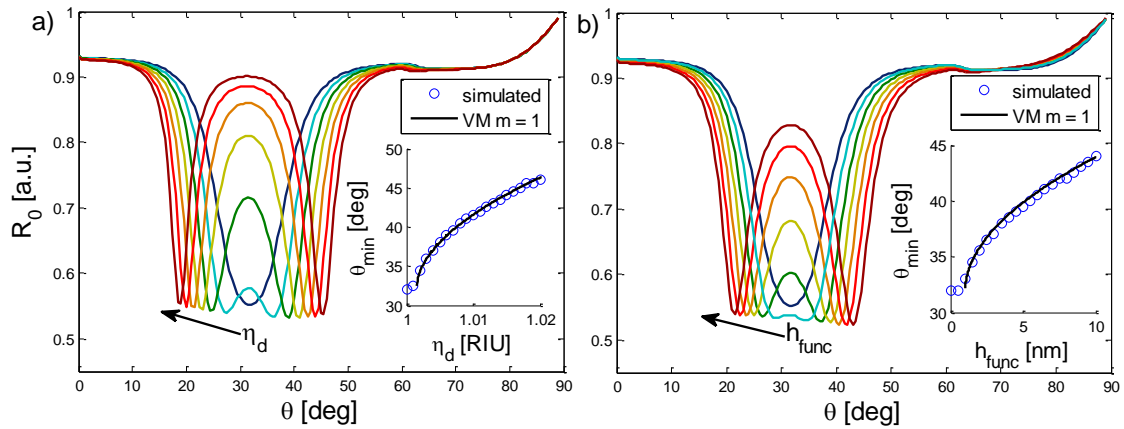
Figure 3.17 DDARM method: (a) R₀ curves as a function of θ calculated increasing η_d, the inset shows the minimum position at higher incident angle as a function of η_d, (b) R₀ curves as a function of θ calculated increasing h_{func}, the inset shows the minimum position at higher incident angle as a function of h_{func}; both were calculated with λ=862 nm and with ψ=140°.

Single Deep Azimuthally rotated method: grating with $\phi \neq 0°$.

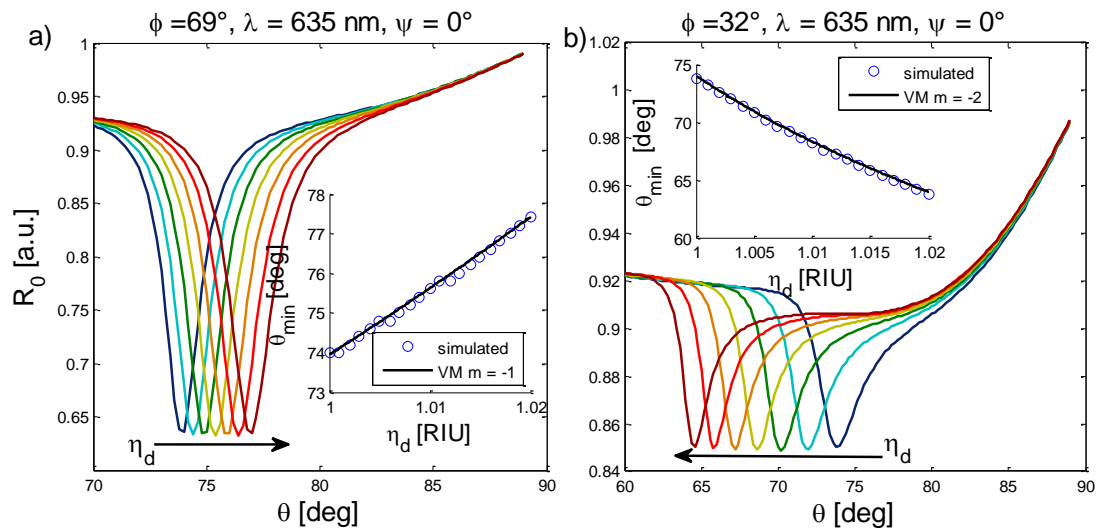**Figure 3.18 SDARM method: (a), (b) R₀ curves as a function of θ calculated increasing η_d, the insets show the minimum position at higher incident angle as a function of η_d, for the SPR m=-1 and m=-2, respectively.**

In figure 3.18a and 3.18b we report the R₀ curves as a function of the incident angle for increasing values of the parameter η_d for the SPR order m=-1 and m=-2, respectively. Also in this case the grating was azimuthally rotated respect to the scattering plane using ϕ=69° for the SPR m=-1 and ϕ=32° for m=-2. The insets of the figure show the relation between the simulated position of the resonance minimum and η_d. Also in this case an excellent agreement between the VM and the RCWA calculations can be noted. As we found for the case at ϕ=0°, the two resonances behave in two ways. For the SPR m=-1 the resonance angle increases with the increasing of η_d; on the contrary for the SPR order m=-2 the minimum angle position decreases with the increasing of η_d. We can also notice that the relation between the minima position and the η_d is not perfectly linear, in particular for the SPR m=-2 case. If the parameter h_{func} is

varied, instead of η_d, the resonance behaviour is the same, and the sensitivity values we found are reported in table 3.8.

The sensitivity enhancement obtained with this Single Deep Azimuthal Rotated Method (SDARM) is also based on the parabolic resonance shape that can be seen in figure 3.1. These resonances refers to the ∪ or ∩-shaped curves $\phi(\theta)$ that can be noticed for the SPR m=-1 and m=-2 if θ>60°. In this case only half of the parabolic curves is present since θ cannot exceed 90°, hence we are dealing with a single deep resonance. The resonance vertex has θ=90° and its ϕ angle depends on the plasmonic resonance order being 68° for m=-1 and 33° for m=-2. Since the resonance has a semi-parabolic shape its sensitivity can be enhanced by tuning the parameter ϕ assuming here the same role of λ in the DDARM. In this case a functionalization of the surface causes a shift upward (downward) of the azimuthal coordinate of the parabolic vertex for the SPR m=-2 (m=-1). By accurately fixing ϕ one can tune the angular sensitivity. Nevertheless the highest sensitivity configuration coincides with θ=90° but this configuration is experimentally unachievable.

	FWMH [deg]	$\frac{\partial\theta}{\partial\eta_d}$ [deg/RIU]	$\frac{\partial\theta}{\partial\eta_d FWMH}$ [1/RIU]	$\frac{\partial\theta}{\partial h_{func}}$[deg/nm]	$\frac{\partial\theta}{\partial h_{func}FWMH}$[1/nm]
SPR m=1	0.6	55	91.6	0.14	0.23
SPR m=-2	0.8	-135	-168	-0.18	-0.23
Kretschmann	0.4	54	135	0.10	0.25
DDARM Max	2.5	2000	800	3	1.2
DDARM Min	5	500	100	1	0.2
SDARM m=-1	2	175	87	0.80	0.4
SDARM m=-2	3	-500	-166	0.74	0.24

Table 3.8 Overview of the FWMH, Sensitivity, and FOM parameters found using θ as sensing parameter.

Table 3.3 summarized the sensitivity parameters we found for the four different configurations we simulated, considering θ as the sensing parameter.

As we can see, if ϕ=0° (first three rows), the η_d sensitivity for the SPR m=-2 is twice the one retrieved for both the SPR order m= 1 and Kretschmann configurations. The sensitivity to the parameter h_{func} is almost the same for all the three configurations.

A great improvement on the h_{func} and η_d sensitivity is obtained by using the DDARM in its region of sensitivity maximum. Here the sensitivity reaches values up to 2000 deg/RIU. Considering also the FOM, this method seems to be the most suitable for plasmonic detection.

Also by using the SDRAM the sensitivity can be three times greater respect to the grating measured at ϕ=0°.

Both in the DDARM and SDARM methods the ability to enhance and tune the sensitivity parameter is supported by the parabolic shape of the plasmonic resonance. This aspect will be deeply analysed in section 3.4.4 and experimentally in section 4.3.

3.4.3 Polarization sensitivity

Another parameter that can be considered for sensing purpose is the polarization angle as previously done by Romanato [28], [89], [90]. In this case the parameters λ, θ, ϕ will be fixed and the only varying parameter will be the polarization angle ψ.
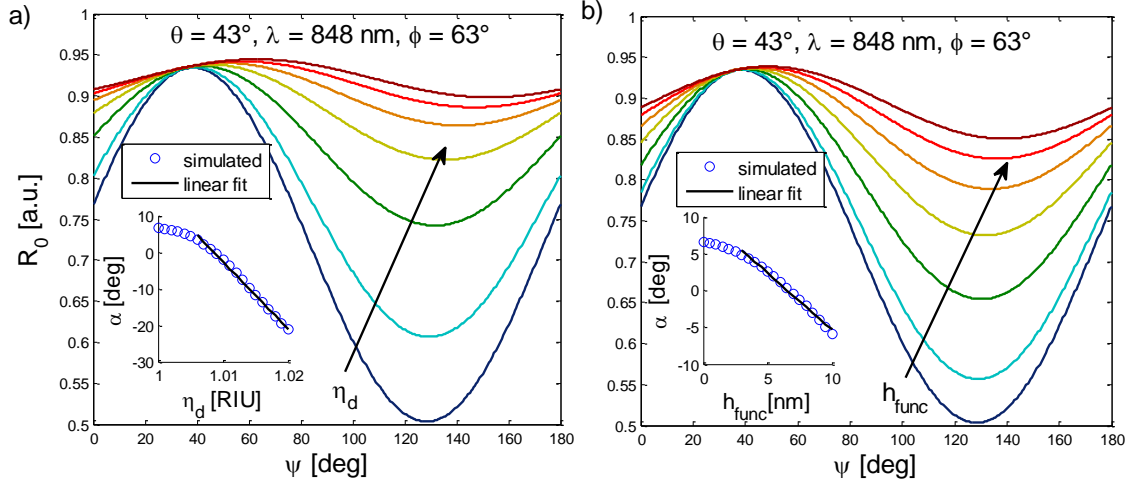
Figure 3.19: (a) R_0 curves as a function of ψ calculated increasing η_d, the inset shows the phase parameter α as a function of η_d, (b) R_0 curves as a function of ψ calculated increasing h_{func}, the inset shows the inset shows the phase parameter α as a function of h_{func}; both were calculated with λ=848 nm, θ=43°, and with ϕ=63°.

In figure 3.19a and 3.19b we will see how the curves of R_0 as a function of ψ are affected by the increasing of the parameters η_d and h_{func}, respectively. The incoming light parameters used are: λ=848 nm, θ=43° and ϕ= 63°. We notice that the shape of the curves is a classical harmonic function:

$$R_0 = A \sin\left(\frac{2\pi}{180}(\psi + \alpha)\right) + \delta \tag{3.7}$$

Where A represent the amplitude, δ the baseline, and α the phase of the reflectance oscillation. The relation between the curve phase α and the parameter η_d or h_{func} is reported in the insets of the figure 3.19a and 3.19b. In this case the VM cannot reproduce these curve since the incoming light polarizations is not considered in this model. Also in this case the relation is not linear and in order to evaluate the α-sensitivity parameter we fitted the RCWA results with a linear curve that will roughly reproduce the phase shift as a function of η_d or h_{func}. Usually for low values of η_d and h_{func} the α-sensitivity is almost 0 deg/RIU and then it increases. These initial parameters (λ=848 nm, θ=43° and ϕ= 63°) were chosen in reference to figure 3.16a by supposing that the initial grating condition η_d=1 RIU (h_{func}=0 nm) lies on the parabolic plasmonic resonance. The same analysis were performed considering different initial parameters belonging to this parabolic m=1 SPR. The phase sensitivity results are reported in table 3.9.

Nevertheless the polarization sensing method does not need to be performed necessarily when a parabolic shape of the resonance is present. In order to verify this we simulated the α-sensitivity for our grating when: λ=635 nm, θ=59.5° and ϕ= 74° as reported in figure 3.20. These parameters were chosen in reference to figure 3.1b in order to exploit the polarization behaviour of the order m=-1 SPR.
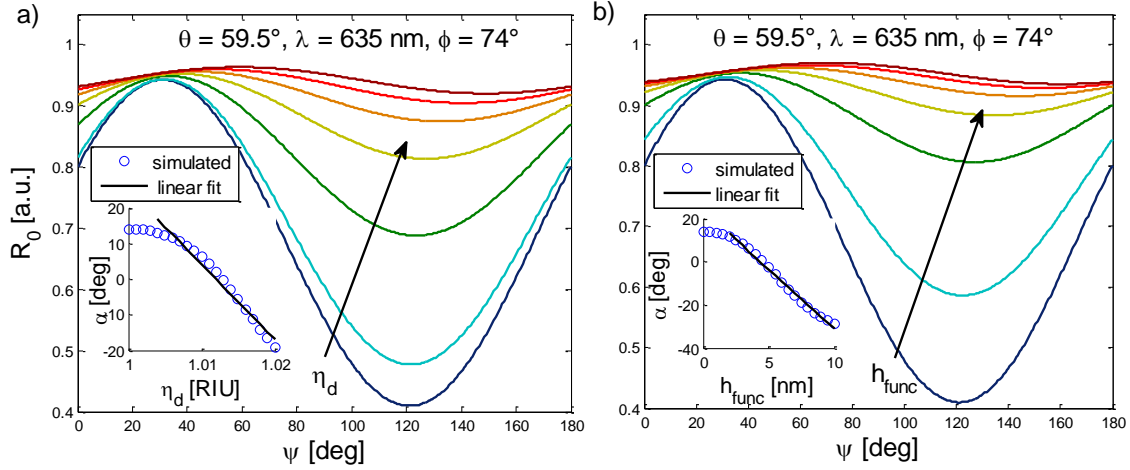
Figure3.20 (a) R_0 **curves as a function of** ψ **calculated increasing** η_d**, the inset shows the phase parameter** α **as a function of** η_d**, (b)** R_0 **curves as a function of** ψ **calculated increasing** h_{func}**, the inset shows the inset shows the phase parameter** α **as a function of** h_{func}**; both were calculated with** λ**=635 nm,** θ**=59.5°, and with** ϕ**=74°.**

In figure 3.20a and 3.20b we report the curves R_0 as a function of ψ for different values of η_d and h_{func}, respectively. From the insets of the figures 3.20a and 3.20b, that report α as a function of η_d and h_{func}, we can notice the same behaviour registered in the precedent case, even if this time the starting condition of the SPP excitation relays on the SPR m=-1 (see Figure 3.1b). Again, the behaviour of α is not linear as a function of the functionalization parameters η_d and h_{func} and a linear fit were used to roughly reproduce the resonance behaviour. Also in this case we studied different initial conditions applied to this sensing technique.

The other cases we studied were chosen, in reference to figure 3.1. We selected the pairs: θ=15.5° ϕ=54°, θ=51° ϕ=22°, and θ=64.5° ϕ=30°, always with λ=635 nm. The first pair refers to the order m=1 SPR while the last two pairs refers to the order m=-2 SPR. We found that the m=-2 SPR is not suited for this kind of sensing method, because the parameter α as a function of η_d and h_{func} is represented by a not-monotonic function. This implies that two different functionalization parameters produce the same phase preventing the discrimination between the two different surface conditions. For this reason we do not reported the results obtained for SPR m=-2 in table 3.9.

λ [nm]	ϕ [deg]	θ [deg]	m	$\frac{\partial\alpha}{\partial\eta_d}$ [deg/RIU]	$\frac{\partial\alpha}{\partial h_{func}}$[deg/nm]
848	63	20	1	-480	-0.29
856	63	24.5	1	-765	-0.43
860	63	32	1	-1380	-0.82
856	63	39.5	1	-1670	-1.16
848	63	43	1	-1830	-1.54
635	54	15.5	1	-144	-0.25
635	74	59.5	-1	-2100	-5.50

Table 3.9 Phase polarization sensitivity found for different configurations

This sensing technique is possible only if $\phi \neq 0°$ since the maximum excitation of the SPPs must not happen in the TM polarization mode. An analytical expression for the polarization angle that maximizes the excitation of the SPR resonance ψ_{opt} can be found in [28], [96] and it is:

$$tan(\psi_{opt}) = tan(\phi)\cos(\theta_{res}) \tag{3.8}$$

where θ_{res} is the angle where the SPR resonance happen. From this equation we can guess that a changes in the values of θ_{res}, due to a functionalization process, affect also the ψ_{opt} parameter which is proportional to α. This expression states also that if $\phi = 0°$ a change in the θ_{res} will not influence the ψ_{opt} parameter, hence this sensing method could be performed only if ϕ is exploited.

As we can see from table 3.9 the sensitivity increases with the increasing of the light incident angle. The sensitivity to the parameter η_d reaches the same values (1830 ÷ 2100 deg/RIU) even if the SPR coupling order m change from 1 (5-th row) to -1(7-th row). Otherwise the sensitivity to the parameter h_{func} is five time higher if m is varied from 1 to -1 going from a value of -1.54 deg/nm to -5.50 deg/nm, respectively. The FOM and FWMH of these resonance were not taken into consideration due to the harmonic shape of the function.

These results show that even if this method does not directly monitor the resonance position its sensitivity could be comparable with the one found by using the DDARM. An exceptional high sensitivity to the h_{func} parameter is found using the SPR m=-1 order.

3.4.4 Azimuthal angle sensitivity

The SPR shift can be analysed by monitor the ϕ angle once fixed the incident wavelength λ and θ [91]. In fact the resonance assumes a parabolic ⊂-shaped form if θ is considered as a function of ϕ, as we already seen in figure 3.1, both for the order m=1 and m=-2. Due to the parabolic resonance shape this detection method has almost the same features we analysed for the DDARM and SDARM methods.
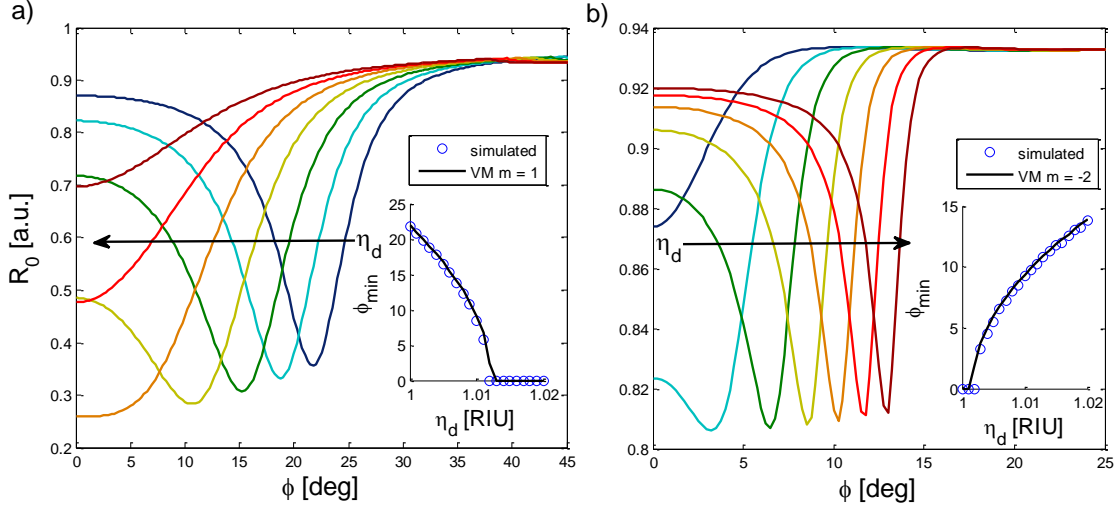

Figure 3.21 Azimuthal method: (a)and (b) R$_0$ curves as a function of ϕ calculated increasing η_d, the insets shows the minimum as a function of η_d, for the SPR m=1 and m=-2 respectively; both figures were calculated with λ=635 nm in TM polarization, and θ=11° for the SPR m=1 and 42.5° for the SPR m=-2.

In figure 3.21a and 3.21b we report the curves of R$_0$ as a function of the ϕ angle for different values of η_d and for the SPR m=1 and m=-2, respectively. We are lighting the grating with $\lambda = 635$ nm, and θ was set to 11° and 42.5° for the SPR m=1 and m=-2, respectively. Since in this case we assumed TM polarized light the curves result symmetric respect to ϕ=0°, hence we report only the positive ϕ angles. The insets of the two figures report the position of the resonance as a function of η_d. We can notice a nonlinear relation between azimuthal resonance position and η_d nevertheless the simulated points are excellently fitted by the VM.

Noticeably, for the SPR m=1, if η_d increases the azimuthal resonance position decreases, until the two dips merge into a single one. Conversely for the SPR m=-2 a single large minimum is initially present and then two dips appear with η_d increasing. The azimuthal position of these dips increases with the increasing of η_d. In both cases the modulus of the sensitivity $\partial\phi/\partial\eta_d$ diverge as the azimuthal resonance approaches ϕ=0°.

The same resonance behaviour is found if we increase the parameter h_{func}. These features of the resonances are very similar to the ones found for the DDARM and it is common when a parabolic shape resonance is exploited for sensing purpose. Also in this case in order to analyse the main features of this sensing method we reported in table 3.10 the maximum and minimum sensitivity values we simulated.

	FWMH [deg]	$\frac{\partial\phi}{\partial\eta_d}$ [deg/RIU]	$\frac{\partial\phi}{\partial\eta_d FWMH}$ [1/RIU]	$\frac{\partial\phi}{\partial h_{func}}$[deg/nm]	$\frac{\partial\phi}{\partial h_{func} FWMH}$[1/nm]
m =1 Max	3	-5750	-1920	-10.5	-3.5
m =1 Min	7.5	-1000	-133	-2	-0.27
m =-2 Max	1.5	3250	2170	3	2
m =-2 Min	2	500	250	1	0.5

Table 3.10 Overview of the FWMH, Sensitivity, and FOM parameters found using ϕ as sensing parameter

In the Table 3.10 we report the maximum and minimum values of sensitivity, we found by using this detection technique. As we can see the sensitivity along with the FOM reaches very high values, if considered in the region of the sensitivity maximum near ϕ=0°. The maximum sensitivity values reported are slightly higher than the one reported in Table 3.8 for the DDARM model. Also in this case for a complete discussion of the FOM and FWMH behaviour the reader should see section 4.3.

The features we will analyse hereinafter can be always applied when a parabolic resonance shape is found i.e. for the DDARM, for the SDARM, for this azimuthal case and even for the V-shaped resonance that can be seen in figure 3.11. We will take the azimuthal sensitivity as example since it is the main argument of this work. In particular we will see how it is possible to tune and enhance the sensitivity just by changing the light incident angle.
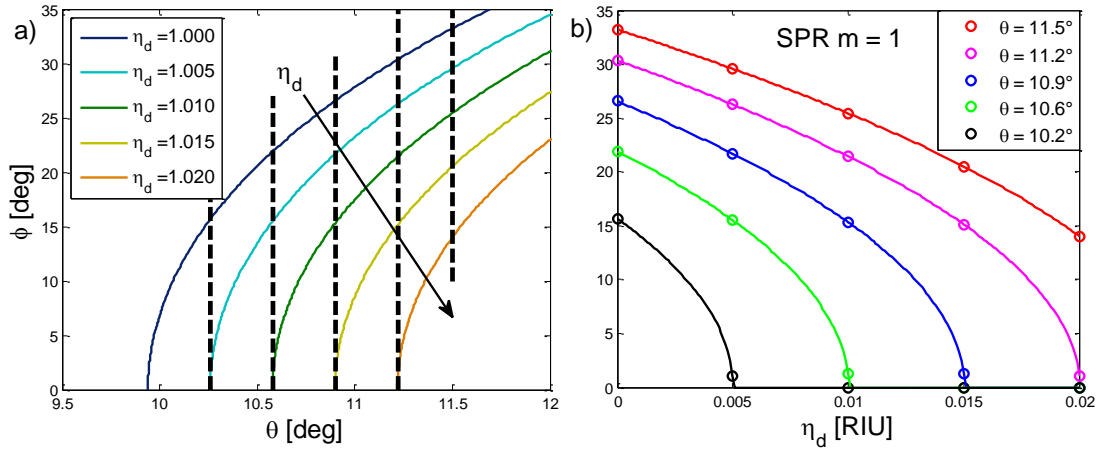

Figure 3.22 (a) Shift of the SPR m=1 curves in the θ, ϕ plane increasing the η_d. (b) ϕ resonance position calculated as a function of η_d for fixed incident angles.

We report in Figure 3.22a what happens to the SPR m = 1, calculated with the VM, in the plane θ, ϕ increasing the parameter η_d. As we can see, increasing η_d, the resonances curves shift to higher θ values respect to the curve having η_d=1, changing in this way the θ-coordinate of the vertex position. Fixed an incident angle θ (vertical black dashed lines) the ϕ-position of the resonance is represented by the intersection between the vertical black dashed lines and the resonance curves. The ϕ-resonance as a function of η_d are reported in figure 3.22b for the five different θ angles. If a measurement with θ = 11.5° is performed the ϕ-position of the resonance decrease augmenting the parameter η_d. Changing θ the ϕ-position of the resonance for each η_d conditions changes and as well as the azimuthal variation $\Delta\phi$ between two consecutive values of η_d. This variation is maximized when the fixed θ corresponds exactly the SPR parabola vertex. For example, if one consider the azimuthal variation between η_d=1.015 and η_d=1.020 for θ = 11.5° a $\Delta\phi$=-5° is achieved meanwhile if θ = 11.2° the $\Delta\phi$ is improved to -12°,

since θ=11.2° is the parabola vertex calculated for the η_d=1.020 SPR curve (brown line in figure 3.22a).

The azimuthal sensitivity parameter $S_\phi = \dfrac{\partial \phi}{\partial \eta_d}$ is related to the slope of the curves reported in figure 3.22b. As we can see the slope is always negative and tends to diverge as the ϕ-resonance approaches 0°.
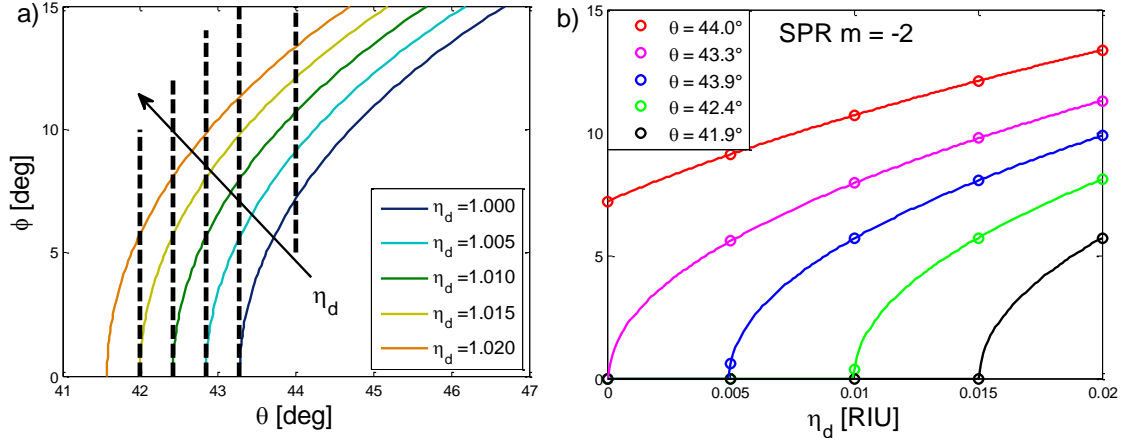

Figure 3.23 (a) Shift of the SPR m=-2 curves in the θ, ϕ plane increasing the η_d. (b) ϕ resonance position calculated as a function of η_d for fixed incident angles.

The behaviour for the SPR m=-2 is reported in figure 3.23a. In this case the VM resonances calculated in the plane θ, ϕ shift to the left with the increasing of the parameter η_d. This implies that the θ-coordinate of the parabolic vertex position decreases with the increasing of η_d, contrarily to what happen for the SPR m=1 case. The ϕ-resonance as a function of η_d are reported in figure 3.23b for the five different θ-angles (black dashed line in figure 3.23a). If a measurements with θ = 44.0° is performed the ϕ-position of the resonance increases augmenting the parameter η_d. Also in this case changing θ, the resonance ϕ-position for each η_d conditions changes as well as the azimuthal variation $\Delta\phi$ between each consecutive values of η_d. This variation is maximized when the fixed θ is exactly the SPR parabola vertex. For example, the azimuthal variation calculated considering η_d=1.000 and η_d=1.005 for θ = 44.0° is $\Delta\phi$=2°, while if θ=43.3° the $\Delta\phi$ is improved to 5.5°, since θ=43.3° is the parabola vertex calculated for the η_d=1.000 SPR curve (the dark blue curve in figure 3.23a).

The azimuthal sensitivity parameter S_ϕ is always positive and tends to diverge as the ϕ-resonance approaches 0°.

In conclusion, if a plasmonic resonance has a parabolic shape it can be used for enhance and tune the sensitivity. In the general case, the parabolic resonance could be approximated in its vertex by the following curve:

$$\rho(\sigma) \sim \rho_c + K(\sigma - \sigma_c)^2 + \mathcal{O}[(\sigma - \sigma_c)^4] \qquad (3.8)$$

where the parameter σ_c does not change as a consequence of a functionalization process while the parameter ρ_c is affected by the resonance. Fixed ρ, the resonance is monitored as a function of σ and the sensitivity $S_\sigma = \dfrac{\partial \sigma}{\partial \eta_d}$ can be maximized imposing $\sigma = \sigma_c$.

Method	ρ	σ
DDARM	λ	θ
SDARM	ϕ	θ
Azimuthal	θ	ϕ
--	λ	ϕ

Table 3.11 Different configurations where a parabolic resonance shape can be used.

In table 3.11 we report some different configurations where a parabolic resonance shape cab be used in order to enhance and tune the sensitivity. The one represented in the last row was not treated here but it is a possible configuration, since solving the VM as a function of λ and ϕ one can find a parabolic shape resonance.

Even if S_σ, in the case of parabolic resonance shape could diverge, this method applied to a functionalization event can produce a maximum shift of the resonance condition:

$$|\Delta\sigma|_{max} = \sqrt{\left|\frac{\Delta\rho}{K}\right|} \qquad (3.9)$$

where $\Delta\rho = \rho_{func} - \rho_{bare}$ and $\Delta\sigma = \sigma_{func} - \sigma_{bare}$ and the subscript bare and func represent the unmodified metallic surface and the functionalized metallic surface. If $K \to 0$ the parameter $|\Delta\sigma|_{max}$ diverges. Obviously it is not possible to reach $K{\sim}0$ conditions since some optical effect will prevent this i.e. the appearances of some Wood-Rayleigh modes.

If we consider the azimuthal method case the parameter $K{\sim}tan(\theta_c)$ directly depends on the θ-vertex position. We found through simulation that to detect a refractive index variation $\Delta\eta_d$=0.001 RIU, $\theta_c \geq$0.8 must be used and a maximum shift of the azimuthal resonance of 20° is calculated, reaching a sensitivity up to 2×10^4 deg/RIU.

4 Experimental Results

In this chapter we will see some main results we obtained in plasmonic sensors characterization. We will describe the two optical benches we used to excite the SPP for the grating and the Kretschmann configurations.

Afterwards we will characterize the grating transmittance parameter T_{tot} when the nanostructure is lighted in conical mounting configuration, and the parameter R_0 if the same nanostructured grating is mounted in Kretschmann configuration. Also the flat surface will be characterized in Kretschmann configuration and the experimental results will be compared with the simulated ones.

Then we will focus on the grating azimuthal sensitivity, changing the parameter η_d and h_{func}. The parameter η_d will be varied by using different water/glycerol solutions while for increasing the h_{func} parameter, functionalization layers of different thicknesses adsorbed onto the surface will be used.

Finally we will see the SPR shift produced when an antibody layer is immobilized onto the grating surface exploiting both the ϕ-sensitivity in the grating configuration and the θ-sensitivity in the Kretschmann configuration.

4.1   Experimental methods

In this section we describe the two optoelectronic benches we used to perform the characterization of the SPRs. We illustrate the optoelectronic components we used and the Labview$^{©}$ v8.6 implemented algorithms for the data acquisition.

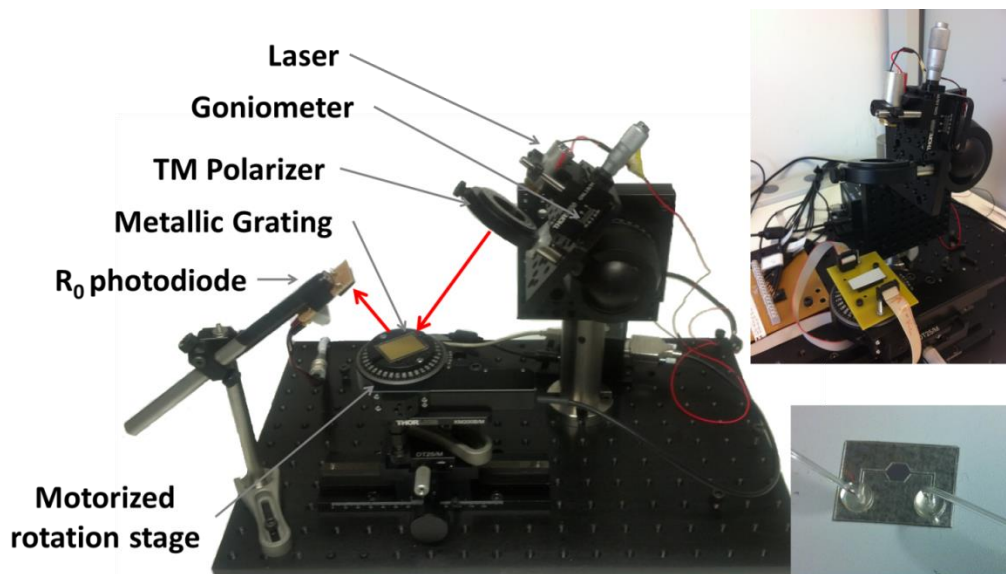### 4.1.1   Conical mounting configuration bench

Figure 4.1 Optoelectronic bench used for the excitation of the grating coupled SPR in conical mounting configuration, R_0 sensing configuration. Upper inset T_{tot} sensing configuration, Lower inset: grating with the microfluidic cell.

Figure 4.1 shows the opto-electronical bench for the conical mounting configuration [74]. This optical bench allows to change both θ and ϕ.

The light source is a solid-state laser diode (VHK model, Edmund Optics) with 635 nm wavelength. The incident angle θ is fixed using a rotation stage (SL 20 model, Thorlabs) with a full 360° angular sweep and a resolution of 2°. In order to accurately vary θ, the laser is mounted on a goniometer (GNL18 model, Thorlabs) with a range of 10° and a resolution of 10'.The laser beam is polarized in the Transverse Magnetic (TM) mode. In order to vary the ϕ-angle a motorized rotation stage (PRM1Z8 model, Thorlabs), mounted on a x-y translation stage (ThorlabsDT25/M, Edmund Optics 56-795) is used. The photodiodes we used is an Hamamatsu S1337 1010BR. We choose this photodiode because it has an high photosensitive area of 10 x 10 mm^2, an high photosensitivity of 0.4 A/W, and a low dark current 200 pA.

If we want to monitor the R_0 parameter the photodiode is mounted above the grating device as we can see from figure4.10. When the transmittance is monitored, a photodiode is mounted on a custom socket as can be seen in the upper right inset of figure 4.1. Measuring the two quantities simultaneously, does not bring any advantage in term of the SPR detection improvement since for a fixed θ the azimuthal resonance does not occur at the same ϕ as previously discussed in section 3.1. When the T_{tot} parameter is measured the grating substrate must be optimally coupled with the photodiode window through an optical matching oil (Cargille Immersion Oil Type A) with 1.51 refraction index. This allows the correct propagation of the Kretschmann ray from the polycarbonate substrate to the photodiode sensitive are, and hence the correct detection of the plasmonic resonance, as we analysed in section 3.3.

In order to read the transmitted light signal intensity the photodiodes are connected to a parameter analyzer (HP 4156B), which applies a constant bias of -2V to the photodiodes and acquires the modulated current. By using this instrumental configuration we obtain a linear relation between the measured current and the light intensity. We also used this optical bench to monitor the kinetic behaviour of the azimuthal signal when the grating surface is exposed to different liquid solutions. We achieved this by applying a microfluidic cell on the top of the grating surface (lower right inset of figure 4.1) and connecting it with a peristaltic pump in order to control the solution flux.

Our typical measurement consists in the acquisition of the current as a function of ϕ, with a fixed θ. The currents measured when the grating is present are normalized by the current measured when the laser directly hits the photodiode, in order to calculated T_{tot} or R_0 parameters. We implemented two software for measuring the SPR resonance. The first one is optimized for the acquisition of the complete resonance curve, acquiring the T_{tot} or R_0 parameters while ϕ is continuously varied through the motorized rotation stage. The second one is optimized for the measurement of the resonance kinetics due to functionalization modifications that occurs at the metal/dielectric interface. We will briefly describe the developed software by mean of their block diagrams and interface.

We report the block diagram of the first software in figure 4.2, left part, and a screenshot of the software in the right part. First of all, the users must insert the start (ϕ_s), and stop (ϕ_e) angles of the measurement. Then the angular velocity ω of the motorized stage and a parameter δ must be inserted; usually they are set to 1 deg/sec and 0.05 deg. When the procedure starts, the

software sets the motorized rotation stage at $\phi < \phi_s$ and then the rotation starts. When ϕ_s is reached, the motorized rotation stage completes its acceleration process, and its angular velocity is now constant. When the motorized rotation stage moves, we continuously measure its position ϕ_m, and if it satisfies the first condition block $|\phi_m - \phi_s| < \delta$, the current measurement starts. The current measurement ends when $|\phi_m - \phi_e| < \delta$. Hence δ defines the angular interval where the measurement starts and stops.
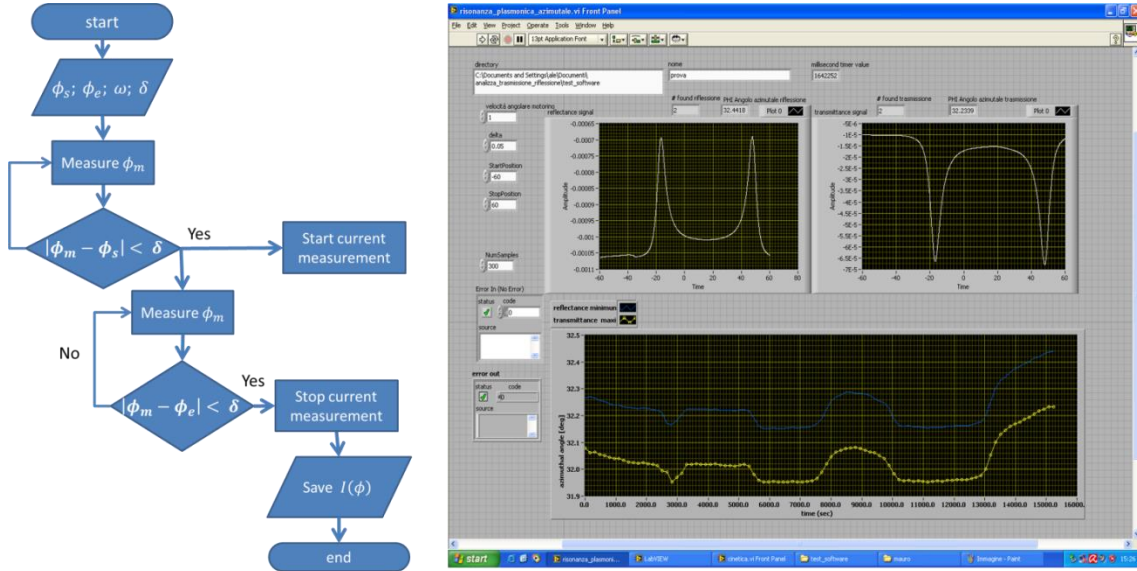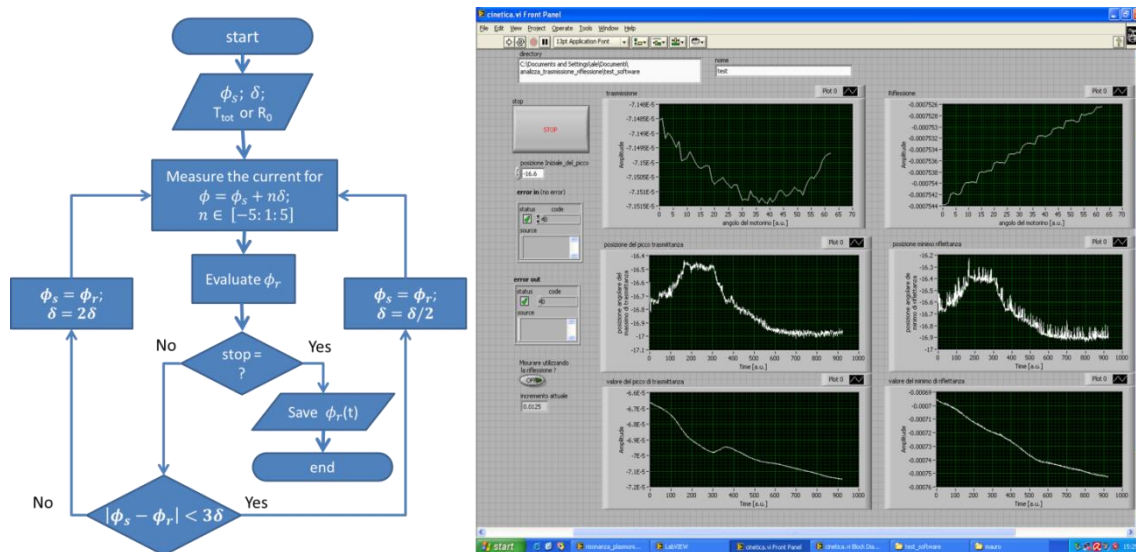

Figure 4.2 Block diagram and software interface for the acquisition of the complete resonance curve for the grating lighted in conical mounting configuration.

When the motorized rotation stage stops we retrieve the current measured from the parameter analyzer and we relate these values to the corresponding angular position, by using the following formula:

$$\phi = \phi_s + \frac{(\phi_e - \phi_s)}{N}[0:1:N-1] \qquad (4.1)$$

where N is the number of measurement performed by the parameter analyzer. Obviously, the angular sampling frequency depends on the angular velocity of the motorized stage, if the parameter analyzer one is fixed. For $\omega = 1$ deg/sec we obtain an angular sampling frequency of 25 samples/deg. The instrument sampling frequency is fixed because we decided to use for each measured current values an integration time of 20 ms which is equal to the power supply grid period. In this way we avoide to pick up the 50 Hz noise coming from external sources.

As we can see from the software panel in figure 4.2 the measurements are not symmetric respect to the zero of the motorized angle due to a sample misalignment respect to the scattering plane that occurs during its positioning onto the socket. Nevertheless this error is easily corrected exploiting the peak symmetry respect to ϕ=0°. A shift of the measured curve in order to obtain two opposite azimuthal peaks must be performed. The shape of the resonance could appear wrong, but this is due to the fact that the current is reported with its sign. If the modulus of the current is taken into consideration, the resonance appears as minima for the reflectance, and as maxima for the transmittance.

We have also taken into account the effect of a possible delay between the validation of the start and stop conditioning blocks and the effectively start and stop of the HP4156 measurement. Effectively this seem to be negligible for low ω as it is in our case but needs to be considered for $\omega > 5$ deg/sec.

We also include this software in a cycle that allows to repeat the measurement for the desired number of times. The resonances measured for each different acquisition are reported by yellow and blue curves reported in the lower panel of the software interface. The yellow and blue curves refer to the azimuthal resonance as a function of the acquisition time calculated by using the T_{tot} and R_0 signals, respectively. As already found in our simulation (section 3.1) a constant bias of 0.2° is found between the two measured resonance angles.

Figure 4.3 Block diagram and software interface for the acquisition of the SPR kinetics for the grating lighted in conical mounting configuration.

We developed a second software optimized for the kinetics measurement of the plasmonic resonance as a function of the time (Figure 4.3). This software records the azimuthal peak position meanwhile the condition of the metal/dielectric interface changes allowing to monitor the molecular adsorption (see figure 4.24 and following) or the bio-recognition process.

Initially the motor angle of the azimuthal resonance peak ϕ_s must be inserted and δ is fixed to0.2°. The motor moves at step of δ starting from an angular position of $\phi_s - 5\delta$ until it reaches $\phi_s + 5\delta$. In the meantime during the motor movement the current is measured producing a step like functions that could be seen in the two upper panels of the software interface. Then, from the measured currents and the motor angular sweep, the new angular resonance position ϕ_r is retrived. If the new resonance ϕ_r lies in the centre of the previous sampling interval ($|\phi_s - \phi_r| < 3\delta$), the parameter δ is halved; if not, it is doubled. This allows the software to follow the resonance if it is moving, and also to measure it accurately if a new stable condition of the surface is reached. Nevertheless δ could not exceed the value of 0.4° or be lower than 0.0125°. The software registers the resonance position and the current until the user stops the software execution. Moreover the users need to choose which parameter, R_0 or T_{tot}, will be used to evaluate the resonance since, as we previously seen, they have a slightly different azimuthal positions.

4.1.2 Kretschmann configuration bench

In figure 4.4 is reported a schematic of the Kretschmann bench we used [97], and in the inset its picture. The laser source is an Helium-Neon laser HLN100LR (Thorlabs) of 10 mW power. The laser spot is spatially filtered and polarized in the TM mode. The light enters into an NBK7 right angle prism which is mounted on a motorized rotation stage. The reflected light is collected by a photodiode (PDA-100-A-EC). The photodiode support is connected to another motorized stage which is coaxial with the prism one. When the prism stage moves of a step $\Delta\theta$ the photodiode stage moves of a $2\Delta\theta$ step in order to capture the reflected ray power. The flat surface is mounted on the hypotenuse of the prism and here it is optically coupled by using optical matching oil (Cargille Immersion Oil Type A) with 1.51 refraction index.
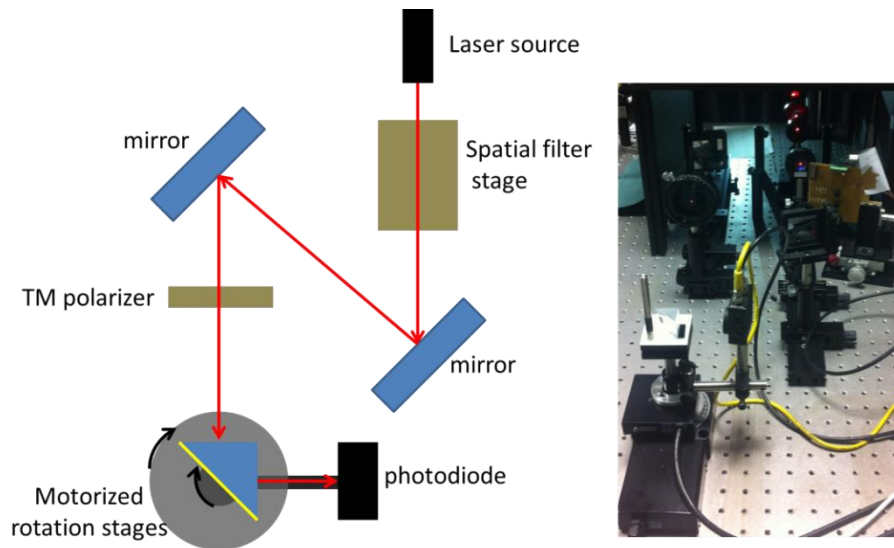
Figure 4.4 (left) schematic of the optoelectronic bench used for Kretschmann configuration, (right) picture of the optoelectronic bench.

The correct position of the prism relatively to the centre of the motorized rotation stage is ensured by the white socket that holds the prism. This socket minimizes the area of the metal/dielectric interface explored by the laser spot during an angular scan.
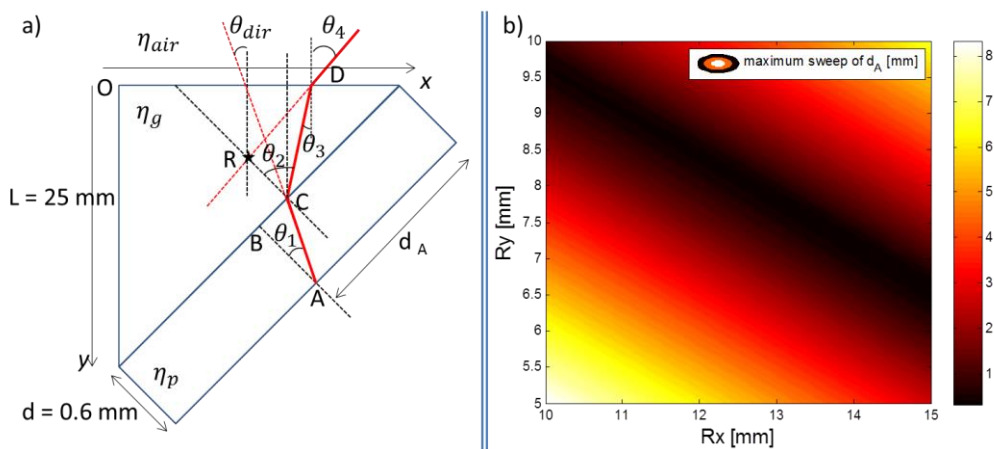

Figure 4.5 (a) Schematic of the ray propagation inside the prism and polycarbonate substrate, supposing that the prism rotation axis is R (star marked point) . (b) Maximum sweep of the parameter d_A as a function of the rotation axis position (R_x, R_y).

The calculus of optimal axis position in order to minimize the spot laser sweep (d_A) as a function of the prism angle was already treat by Qui [98] and we applied it to our case. The schematic of the prism along with the polycarbonate substrate is reported in figure 4.5a. For simplicity, we neglect the presence of the optical matching oil. Fixed the rotation axis position R=(R_x, R_y), marked in the figure4.5a with a star, and the angle of the motorized stage θ_4 it is possible to perform the geometrical ray tracing. In this way we can calculate the position of the point A as a function of θ_4. Our goal is to find the position R that minimizes the maximum sweep of d_A calculated for θ_4 going from -30° to 30° in step of 5°.

The results are reported in figure 4.5b where we can see that for some R_x and R_y the minimum sweep of d_A reaches 0.4 mm.
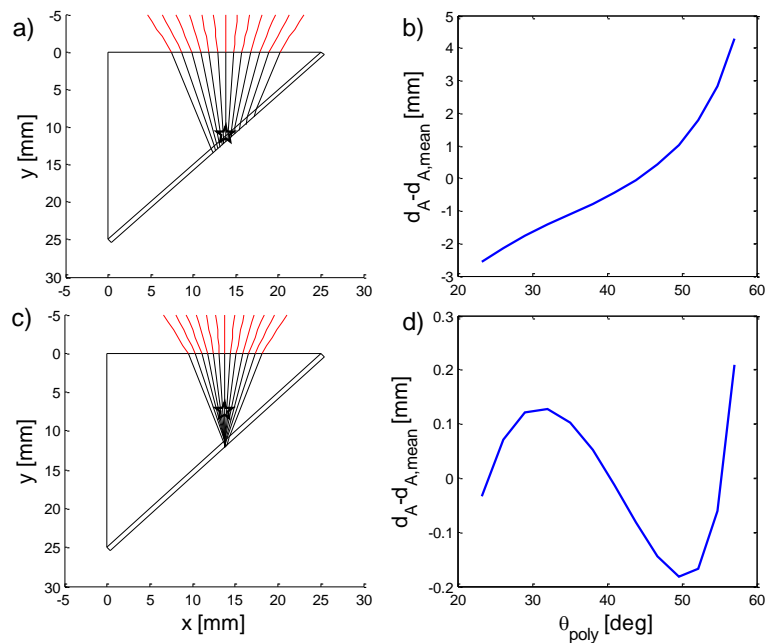

Figure 4.6 Ray tracing of the light inside the prism and polycarbonate substrate: (a) not optimized case R = (13.8,11) mm; (c) optimized case R = (13.8, 7.5) mm. Behaviour of the point A respect to its mean position: (b) not optimized, (d) optimized.

To see what happens during the prism rotation we graphically reproduce the ray tracing for two different positions of the rotation axis. In figure 4.6a R = (13.8, 11) mm was placed in a not optimized condition, on the prism hypotenuse. In the second case figure 4.6c, R = (13.8, 7.5) mm was placed in an optimized position. As we can see in figure 4.6c all the black rays inside the prism converge to almost the same point on the polycarbonate surface while for the figure 4.6a they are spread over all the interface. This is remarked in figure 4.6b and 4.6d where there is reported the sweep of d_A respect to its mean point, calculated by using the not optimized and the optimized prism rotation axis, respectively. As we can see for the optimized one a maximum sweep of 0.4 mm is found while for the not optimized one a sweep of 6.5 mm. This sweep reduction is a noticeable improvement.

By using the white socket, which ensures the correct position of the prism respect to the motor rotation axis, a huge shrink of the spot sweep is performed. We also tried to measure experimentally this improvement. We found that the maximum sweep of d_A goes from 6.5 mm

to 2 mm passing from the not optimized to the optimized rotation axis position. Nevertheless it is very difficult to define the spot position when the light experience the TIR condition, even if in this case we used the grating device in order to extract the ray and localize the spot.

The software used to characterize this type of resonance is reported in figure 4.7. The software is implemented straightforward following the reported block diagram. First of all the user needs to insert the start θ_s, and stop θ_e angles, along with the angular step δ of the measurement. Then the motorized stages set their positions and the photodiode current is measured. The software repeats this sequence until the motor angle θ_m reaches θ_e. Then it saves the photodiode measured currents as a function of the motor angle.
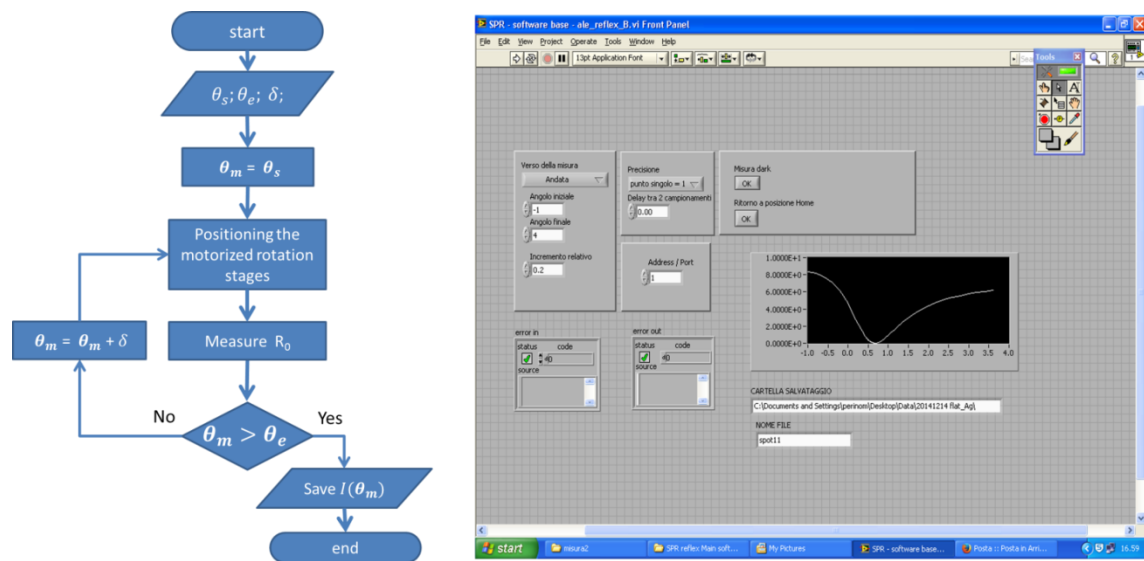

Figure 4.7 Block diagram and software interface for the acquisition of the SPR in Kretschmann configuration

4.1.3   Grating and flat surface, Atomic Force Microscope characterization

The surfaces we used were fabricated by Next Step Engineering s.r.l. a Spin-Off of the University of Padova specialized in design and fabrication of sensors based on plastic substrates.

The fabrication process is based on the replica molding process of the plastic substrate on a flat or nanostructured stamper. The plastic substrate consists in polycarbonate and the stamper used is fabricated through interferential lithography. The silver thin film deposition is made by a physical vapor deposition (PVD). Further fabrication details are omitted because they are intellectual property of the Spin-Off.
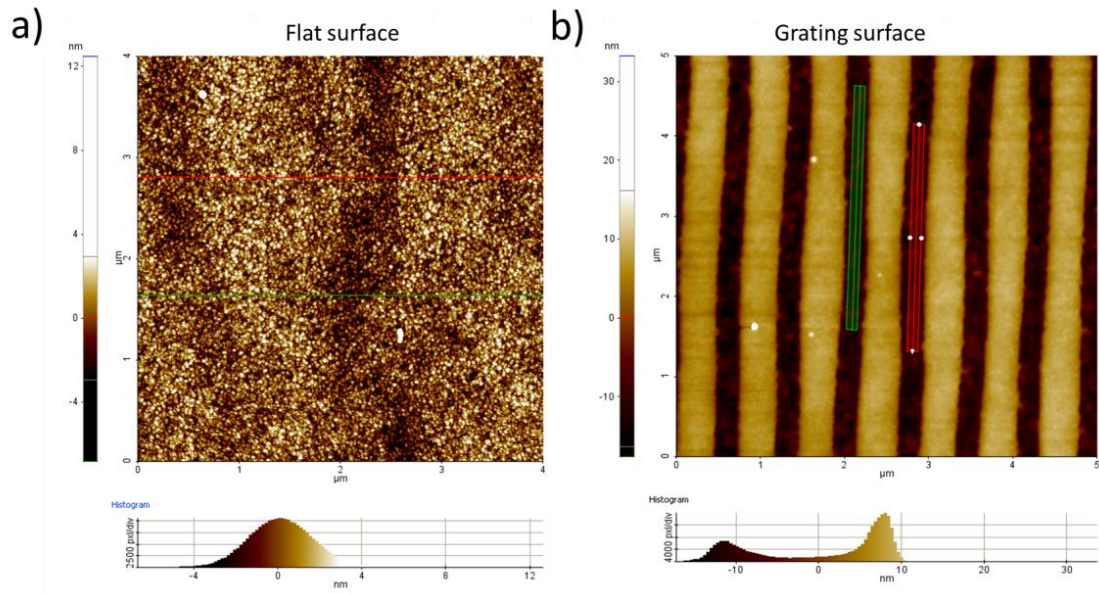
Figure 4.8 Atomic Force Microscope (AFM) characterization of (a) flat surface (b) grating surface

We have characterized the surface through the Atomic Force Microscope (AFM). As we can see from Figure 4.8a the flat surface has only one level which is represented by the Gaussian distribution of the pixel height (low inset of figure 4.8a). The surface roughness is 1.5 nm. The grating AFM characterization is reported in figure 4.8b. This time, the distribution of the pixel height (low inset of figure 4.8b) presents two separated maxima that corresponds to the valleys and peaks of the grating profile. The difference between the position of these two maxima represents the grating amplitude and it is almost 20 nm. Also the period can be roughly estimated and it is about 740 nm. Moreover, we can note that the lower maximum distribution is more spread than the higher one. This means that the valley roughness (1.5 nm) is greater than the peak one (0.5 nm).
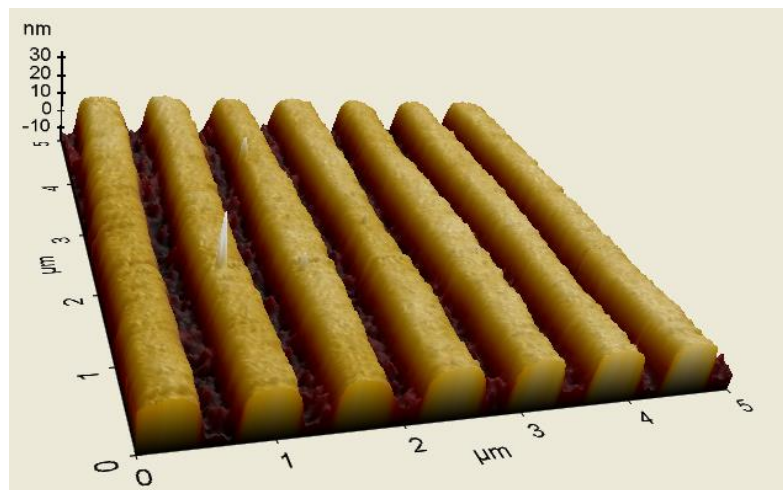

Figure 4.9 3D view of the grating profile.

In figure 4.9 we report a three dimensional view of our grating profile in order to provide a better view of our nanostructured surface profile.

4.2 SPR Characterization

In this section we will characterize the SPR in the grating and Kretschmann configuration. We will measure the grating parameter T_{tot} considering both air and water as dielectric buffer. And for each condition we will consider both the m=1 and m=-2 SPR. Then we will characterize, by means of the R_0 parameter, the SPR of a flat surface and nanostructured surface mounted in the Kretschmann configuration.

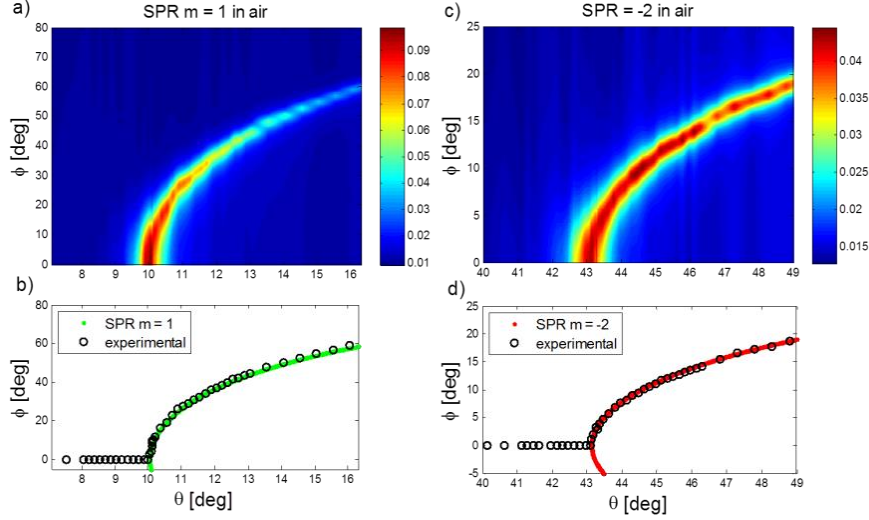### 4.2.1 Grating, T_{tot} in conical mounting configuration

Figure 4.10 (a) T_{tot} map as a function of θ and ϕ (b) azimuthal resonance as a function of θ for the SPR m=1, experimental (black circles), and VM (green dots). (c) T_{tot} map as a function of θ and ϕ (d) azimuthal resonance as a function of θ for the SPR m=-2, experimental (black circles), and VM (red dots). Both calculated for the grating exposed in air.

In Figure 4.10a and 4.10c we show the experimental values of T_{tot} for the grating in air, as a function of θ and ϕ for the m=1 and m=-2 SPR respectively. Figure 4.10b and 4.10d report the experimental azimuthal peak position as a function of θ (black circles) while the continuous lines report the vector model simulation. Both the resonances reported in these maps assume a parabolic shape as already discussed in section 3.1. Considering one of the two maps we can see that the transmittance map cross-section at ϕ=0° produces a maximum in transmittance at θ_c when it satisfies the condition:

$$Re(k_{spp}) = \eta_{air}k_0\sin(\theta_c) + mG \qquad (4.1)$$

The critical point $(\theta_c, 0)$ corresponds to the absolute maximum value of the transmittance map, as expected, since we are using a TM polarization mode. A cross section of the transmittance map at a fixed incident angle $\theta < \theta_c$ shows a maximum in transmittance at ϕ = 0°, whose intensity decreases as θ decreases.. A cross section of the transmittance maps at $\theta > \theta_c$ shows two maxima at $\phi = \pm\phi_r$. In the maps only $+\phi_r$ is reported since the maps are symmetric in ϕ. As we can notice the azimuthal peak intensity decreases as θ increases for the case SPR m=1 while it remains almost constant for the SPR m=-2.

For both the plasmonic orders the peaks behavior is well described by the vector model, i.e. no resonance occurs for $\theta < \theta_c$ and over this critical value two maxima are present at $\pm\phi_r$. Figure 4.10b and 4.10d also show that the experimental positions of the azimuthal maxima match the

ones calculated from the vector model with an excellent correlation factor of 0.9991 and 0.9996 for the SPR m=1 and m=-2, respectively. Nevertheless it is more difficult to find the correct grating geometry that well reproduces the experimental transmittance. This is due to the fact that changes in the grating cross section geometry affect the simulated transmittance values. A geometry that well reproduces the experimental values for the SPR m=1 both in air and in water is the trapezoidal one, reported in table 3.5 [74].
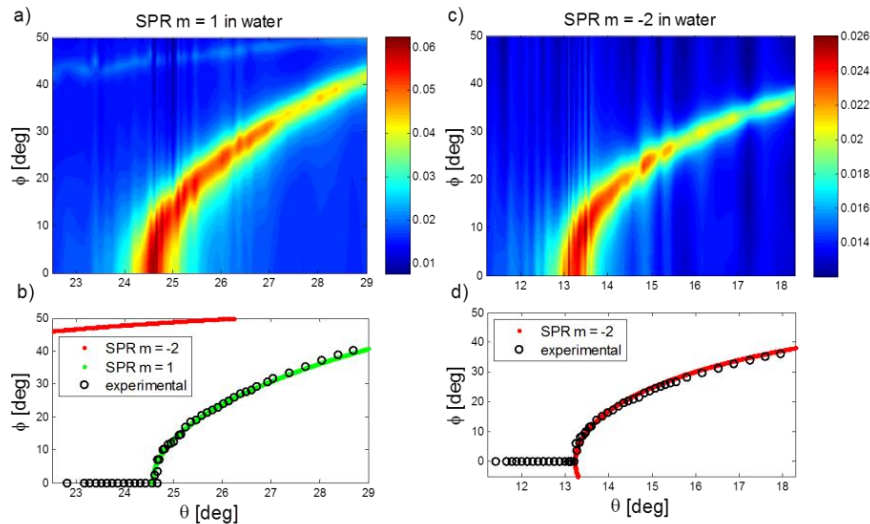

Figure 4.11 (a) T$_{tot}$ map as a function of θ and ϕ (b) azimuthal resonance as a function of θ for the SPR m=1, experimental (black circles), and VM (green dots). (c) T$_{tot}$ map as a function of θ and ϕ (d) azimuthal resonance as a function of θ for the SPR m=-2 experimental (black circles), and VM (red dots). Both calculated for the grating exposed in water.

In Figure 4.11a and 4.11c we show the experimental values of T$_{tot}$ as a function of θ and ϕ measured when the dielectric medium in contact with the grating is water (η_d=1.333), for the m=1 and m=-2 SPR, respectively. Figure 4.11b and 4.11d report the experimental azimuthal peak position as a function of θ (black circles) meanwhile the continuous lines report the results obtained from the vector model. In this case θ is the incident angle in water. This angle is retrieved from the one measured on the optical bench goniometer, just by applying the Snell law at the air/water interface.

Analogously to the air case, both resonances here assume the typical parabolic shape well described by the vector model. The correlation factors we found are 0.9991 and 0.9984 for the SPR m=1 and m=-2, respectively. Moreover we can see also a tail of the SPR m=-2 in figure 4.11a and 4.11b. In the T$_{tot}$ map this tail is represented by an enhancement in the transmittance located between 40° and 50° azimuthal degrees; while it is represented by the continuous red line in figure 4.11b.

In conclusion the grating we used produces SPRs that can be sensed both in air and water if only the incident angle is properly set [82], [99] and an excellent agreement with the VM is found for both cases.
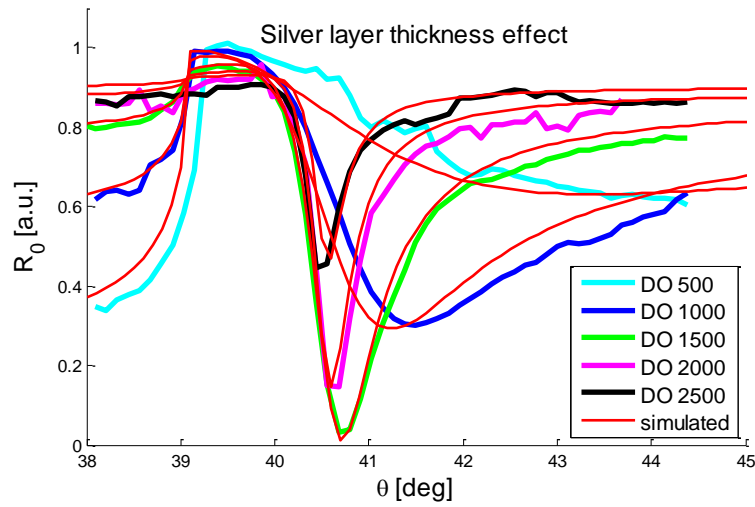
4.2.2 Flat, R_0 in Kretschmann configuration

Figure 4.12 R_0 as a function of θ measured for the flat surfaces having different metallic layer thickness (thick coloured curves: measurements, red curves: simulations), in Kretschmann configuration

In figure 4.12 we report R_0 as a function of θ measured for flat surfaces having different silver film thicknesses (thick coloured curves) along the simulated ones (red curves). The thickness of the film is described by the Optical Density (DO) parameter and the incident angle θ refers to the one inside the polycarbonate substrate. As expected the resonance shape and position is affected by the thickness and the behaviour of the experimental curves is well reproduced by the simulations. The device that produces the best minimum is the one with DO 1500. By simulation we also found the sequent corresponding table between the fabrication parameter DO and the film thicknesses.

OpticalDensity DO	500	1000	1500	2000	2500
Silver film thickness [nm]	13	24	37	50	61

Table 4.1 relation between the DO and the silver thickness

The minimum in the best configuration (DO 1500) appears for θ=40.7° which is almost the same angle we calculated in section 3.2.1

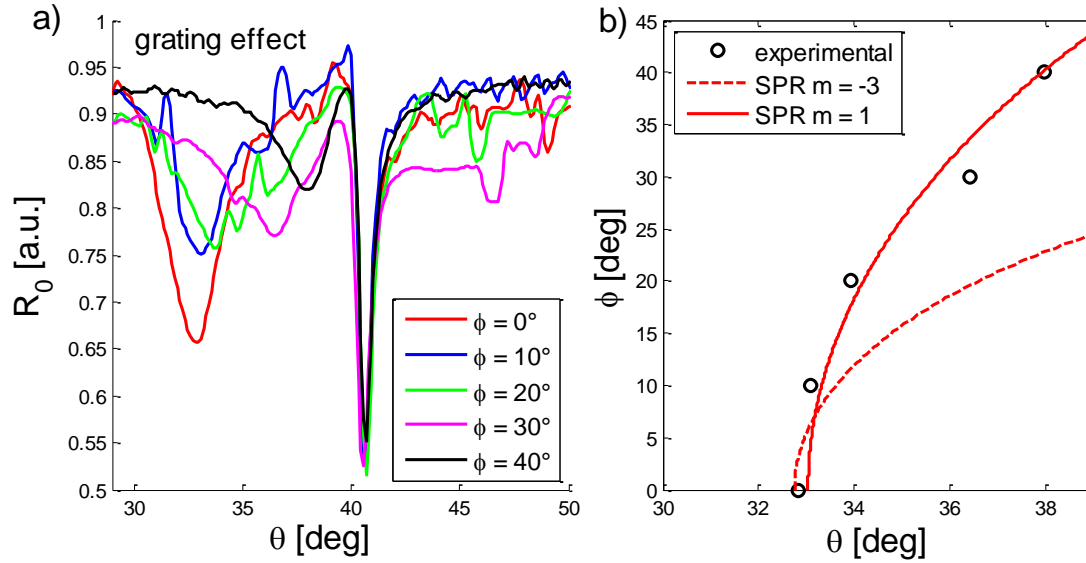### 4.2.3 Grating, R_0 in Kretschmann configuration

Figure 4.13 (a) R_0 as a function of θ measured for the grating surface mounted in Kretschmann configuration for different values of the azimuthal angle ϕ. (b) Measured minima (black circles) as a function of θ along with the VM calculated resonances (red lines)

In Figure 4.13a we report the curves R_0 as a function of θ, measured when a grating device with an optical density of 2500 is mounted in the Kretschmann configuration for five different ϕ angles. The minimum due to the excitation of the SPP at the silver/air interface appears for θ=41° and, as expected from simulations (section 3.2.2), and its angular position and intensity do not depend on the azimuthal angle. Nevertheless another deep is present before the Kretschmann one, and this is due to the excitation of a SPP at the polycarbonate/silver interface. This minimum shifts to higher θ as ϕ increases. Unfortunately the measured curves are quite noisy, but the minimum azimuthal positions as a function of θ (figures 4.13b) follow the SPR m=1, rather than the SPR m=-3 as predicted by the simulations reported in section 3.2.2. This suggests that the plasmonic coupling with SPR m=-3 is not as strong as predicted by the simulations. Nevertheless its weak presence could be hide by the curves noise.

As already anticipate the peak due to the grating is not subject to the surface modifications that happen at the air/metal interface and in this way it can be used as reference peak. A more complete and noise free study of this resonance need to be performed in order to completely characterize this behaviour.

4.3 Detection of bulk refractive index variations

Here we will study how a change in the buffer refractive index (η_d) affects the azimuthal position of the resonance. In order to achieve this goal we used different water/glycerol (Sigma Aldrich) solutions having different refractive index. We changed the solution into the microfluidic cell by using the peristaltic pump and then we measured the T$_{tot}$ parameter as a function of ϕ for fixed incident angles θ. The water/glycerol solution we used are reported in the following table 4.2. The refractive index of the different solutions were calculated using the values reported by Lide et Al. [100].

Solution #	Glycerol % wt	Milli-q %wt	η_d [RIU]	$\Delta\eta_d$ [RIU]
1	0	100	1,333	0,0000
2	2	98	1,3353	0,002
3	5	95	1,3388	0,006
4	10	90	1,3448	0,012
5	20	80	1,3572	0,024
6	30	70	1,3703	0,037
7	40	60	1,3841	0,051
8	50	50	1,39825	0,065
9	60	40	1,4129	0,080

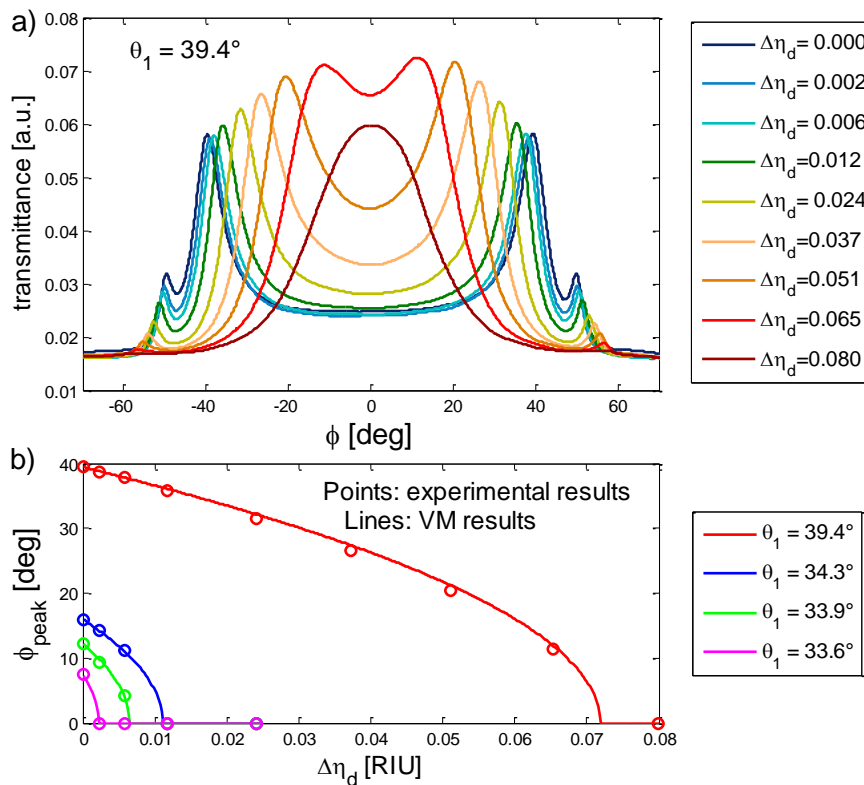**Table 4.2 Water/glycerol solution and their η_d**

Figure 4.14 (a) T$_{tot}$ as a function of ϕ measured for different η_d having fixed θ_1=39.4°; (b) ϕ-peak positions found for the different solutions changing the θ_1, lines and circles represent the VM and experimental results, respectively; all the results were obtained using the TM polarization mode and the SPR m=1.

In figure 4.14a we reported the curves T$_{tot}$ as a function of ϕ measured for the different solutions with θ_1= 39.4°. θ_1 is the incident angle of the light in air, before it passes through the

upper window of the microfluidic cell. This angle does not change with the parameter η_d. Since the light incident angle inside the liquid is subject to the snell law: $\theta = \text{asin}(\eta_{air} \sin(\theta_1)/\eta_d)$. All the simulations reported hereafter are corrected considering this effect. As we can see from the figure 4.14a the azimuthal peak position decreases as η_d increases. untill the two peaks merge into a single one for $\Delta\eta_d$ = 0.08 RIU. It can also be seen that the second weaker maximum, due to the SPR m=-2, has an opposite behaviour: the azimuthal peak position increases increasing η_d.

We perform the same measurements by using different incident angles θ_1 and the results are reported in figure 4.14b. As we can see the experimental azimuthal peaks (circles) as a function of the $\Delta\eta_d$ are well reproduced by the vector model (continuous line). Since the sensitivity of the method is described by $S_\phi = \partial\phi/\partial\eta_d$ it corresponds to the slope of the continuous curves reported in figure 4.14b. As can be noticed this parameter is negative in this case and it is not constant since it diverges as ϕ aproaches 0°, as previously illustred in section 3.4.4. We can also see that in order to tune and maximize the sensitivity parameter for a specific $\Delta\eta_d$, the parameter θ_1 must be changed exploiting the parbolic shape of the resonance.
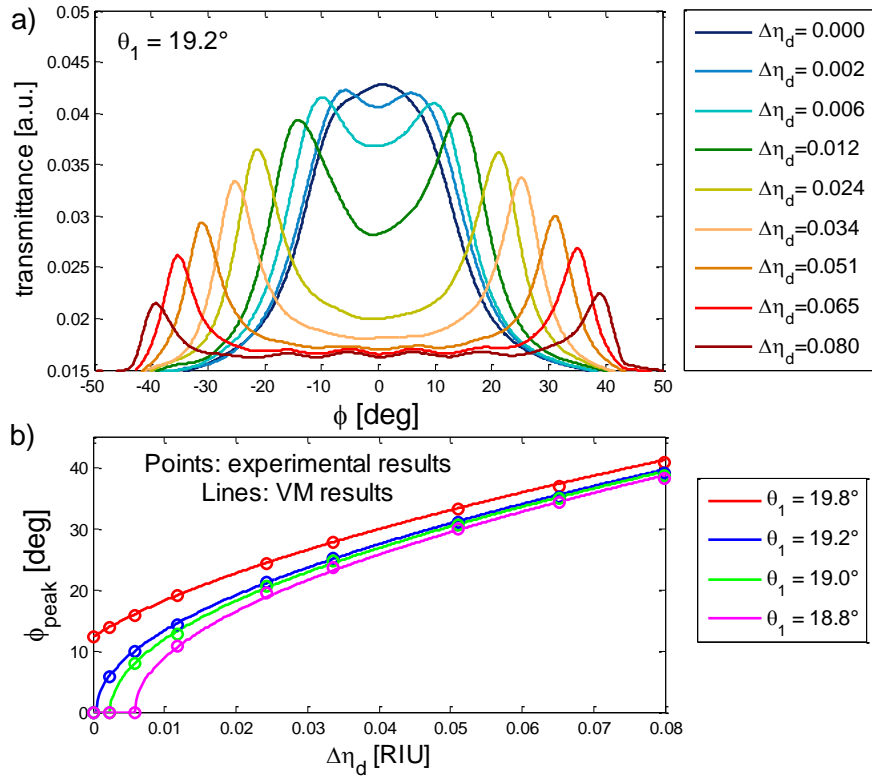

Figure 4.15 (a) T$_{tot}$ as a function of ϕ measured for different η_d having fixed θ_1=19.2°; (b) ϕ-peak positions found for the different solutions changing the θ_1, lines and circles represent the VM and experimental results, respectively; all the results were obtained using the TM polarization mode and the SPR m=-2.

We perform exactly the same experiment for the SPR m=-2. The curves T$_{tot}$ as a function of ϕ for different parameters η_d having θ_1= 19.2° are reported in figure 4.14a. As we can see in this case the azimuthal resonance peak position increases as η_d increases.

Also in this case we perform the same measurements by changing the θ_1 angle. The experimental position of the azimuthal peak (circles) with the vector model calculated ones are

reported in figure 4.14b. Also in this case S_ϕ is always positive and again it diverges as ϕ approaches 0°. Also in this case its values can be set just by changing the θ_1 angle.

Now we will analyse the sensitivity reached by this method and its Figure of Merit (FOM). We will define three different FOMs and we will discuss which one best describe the resonance proprieties. We will always compare our experimental results with the simulated behaviour.
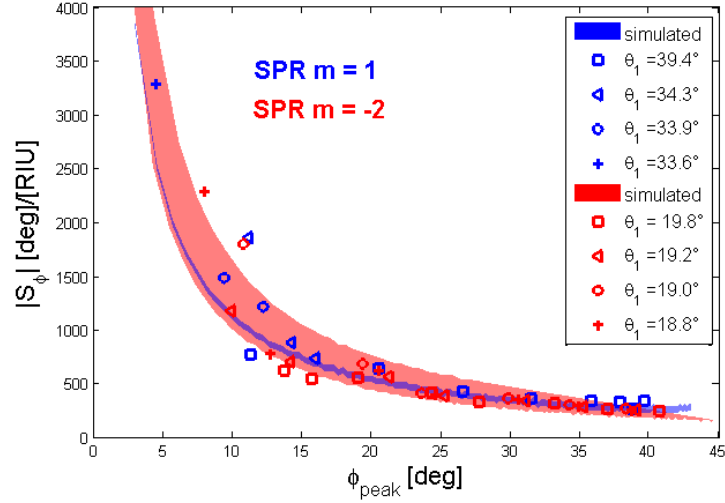

Figure 4.16 $\left|S_\phi\right|$ **plotted as a function of ϕ_{peak}. The marker represent the experimental points meanwhile the shades areas represent the interval values calculated from the simulation using different incident angles. Blue refers to the SPR m=1 and red to the SPR m=-2**

In figure 4.16 we report $\left|S_\phi\right|$ as a function of the ϕ angle. We perform this analysis since we noticed from figure 4.14b and 4.15b that if an azimuthal angle is taken into consideration the slope of the curves $\phi_{peak}(\eta_d)$ is almost the same regardless of the θ_1 used. In fact the curves $\phi_{peak}(\eta_d)$ are almost parallel since them cannot intersect each other. The markers represent the sensitivity values calculated by using the experimental results. The shaded areas represent the interval values of sensitivity as a function of ϕ_{peak}, we calculated by using the RCWA method for different θ_1 angles. The different θ_1 were obtained by solving the equations 4.1 for different values of η_d. For the SPR m=1, θ_1 ranges from 33° to 40° while for SPR m=-2 it goes from 14° to 19°. The blue colour refers to the SPR m=1 while the red one to the SPR m=-2. In the RCWA method the parameter η_d was varied in step of 0.0005 RIU in order to accurately retrieve the sensitivity parameters.

As we can see the simulated curves do not have a huge dependence on θ_1 since the shaded area are well confined in the plot. Nevertheless the sensitivity values of the SPR m=-2 appear more affected by the θ_1 variations respect to the SPR m=1 since the red shaded area is wider than the blue one. If an initial ϕ_{peak}=10° is set S_ϕ for the SPR m=-2 lays between 1000 deg/RIU and 1500 deg/RIU meanwhile for the SPR m=1 it is almost fixed to -1100 deg/RIU. This is due to the fact that the parabolic shape factor K introduced in eq. 3.8 varies quickly for the SPR m=-2 since for low values of θ_1 the vertex θ_c of the resonance parabola shifts to lower incident angles with the K parameter increasing.

The experimental sensitivity well agrees with the simulated one and in both cases it diverges approaching ϕ=0°. Hence, if we want to measure with an high sensitivity we need to have set an initial azimuthal resonance having $\phi_{peak} < 7°$. We also notice that the maximum experimental measured sensitivity reaches 3280 deg/RIU and 2280 deg/RIU for the SPR m=1 and m=-2, respectively. If the initial resonance angle is set to $\phi_{peak} > 20°$ the sensitivity has a value of 320 deg/RIU which slowly decreases with the increasing of ϕ_{peak}. Even if the sensitivity diverges at ϕ_{peak}=0° it is very difficult to set the resonance at this azimuthal angle since the amplitude of the peaks is very low and their position is strongly affected by small changes in θ_1.

In order to analyse the figure of merit of this azimuthal method, we define three different FOMs as follows:

$$FOM_0 = \frac{|S_\phi|}{FWMH_0}; \; FOM_b = \frac{|S_\phi|}{FWMH_b}; \; FOM_T = \frac{|S_\phi|\Delta T}{FWMH_0} \tag{4.2}$$

where S_ϕ is the azimuthal sensitivity, ΔT is the difference between the azimuthal peak transmittance and the transmittance at ϕ=0°. $FWMH_0$ is calculated considering the transmittance at ϕ=0° as the peak baseline while $FWMH_b$ is calculated by using the transmittance at ϕ=90° as the peak baseline.
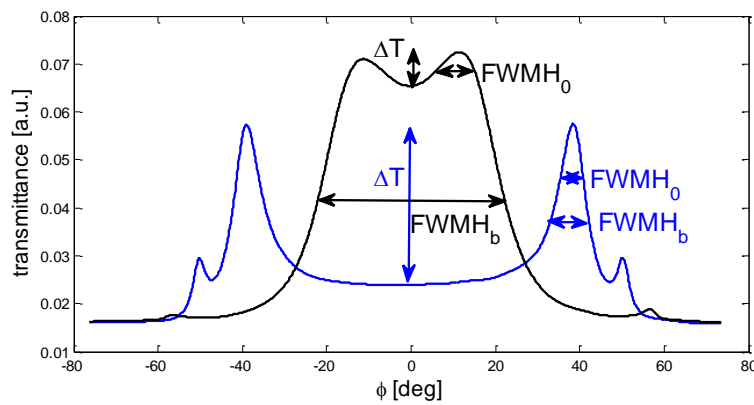

Figure 4.17 Schematic of the parameters used to calculate the FOMs and the two main cases that can appear.

Figure 4.17 shows a schematic of the two main cases that can appear and how we calculated the FWMH. In the first case, the blue one, the two azimuthal peaks are well split and the $FWMH_0$ is slightly lower than the $FWMH_b$ since the transmittance at ϕ = 0° is slightly higher than the one at ϕ=90°. In the second case, the black one, the resonance peaks approach to ϕ=0°. In this case the $FWMH_0$ is smaller than the $FWMH_b$ since the first one is related to the local azimuthal peak shape and not to the total shape of the resonance curve, as it happens for $FWMH_b$.

In figure 4.18a, 4.18b, and 4.18c we reported the values calculated for FOM_0, FOM_b, and FOM_T as a function of ϕ_{peak}. The points represent the values calculated from the experimental results, while the shaded areas report the simulated results changing the incident angle θ_1 as previously illustrated for the sensitivity case. The blue and red colours refer to the SPR m=1 and m=-2, respectively.

In these cases the shaded areas are confined, hence the simulated FOMs as a function of ϕ_{peak} do not depend on the θ_1 angle. Moreover the experimental behaviour is well reproduced by the simulations. FOM_0 starts from a values of 40 RIU^{-1} and grows up to 680 RIU^{-1} as ϕ approaches

0°. This parameter diverges as ϕ_{peak} approaches 0° for two reasons. The first one is that $|S_\phi|$ diverges and the second one is that the $FWMH_0$, for its definition, tends to 0° as ϕ_{peak} approaches 0°. Since it is at the denominator of FOM_0 it contributes to its divergence.

The FOM_b parameter starts from 35 RIU^{-1} and grows up to 90 RIU^{-1} as ϕ_{peak} approaches 0°. We can see that these values are lower than FOM_0 and this is due to the fact that for definition $FWMH_0 < FWMH_b$. The biggest difference between these two parameters is found at ϕ_{peak} approaching 0° since the $FWMH_0$ tends to 0° while $FWMH_b$ reaches an almost constant values of 30°. Still this parameter diverges for ϕ=0° because $|S_\phi|$ diverges. We can also notice some discontinuities of the curves around ϕ=15°~20°. These are due to the fact that here the peaks merge and we effectively jump from a situation described by the blue curve, to a situation described by the black curve of figure 4.17. This implies a discontinuous decreases in the $FWMH_b$ even though this discontinuity has not an important physical meaning.
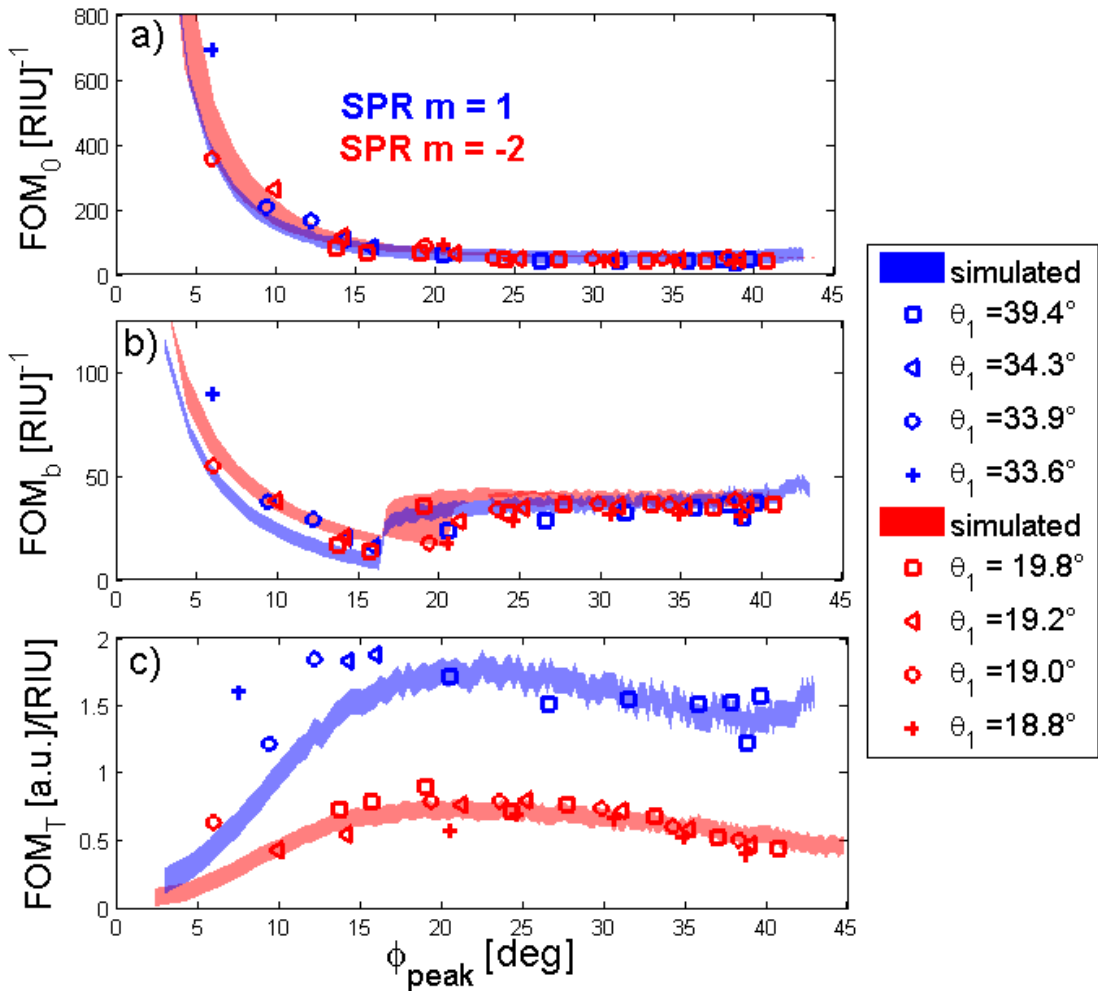

Figure 4.18 (a) FOM_0, (b) FOM_b, (c) FOM_T, plotted as a function of ϕ_{peak}. The marker represent the experimental points meanwhile the shades areas represent the interval values calculated from the simulation using different incident angles. Blue refers to the SPR m=1 and red to the SPR m=-2

The most interesting parameter FOM_T is reported in figure 4.18c. It is calculated by multiplying the FOM_0 with ΔT. This parameter tends to 0 a.u./RIU as ϕ_{peak} approaches 0° and it removes the divergence caused from both the parameter $|S_\phi|$ and $FWMH_0$. In detail FOM_T=0 a.u./RIU

when ϕ_{peak} = 0° and then it increases reaching a maximum at ϕ_{peak}=20° for both the plasmonic orders. After this maximum it slowly decreases as ϕ_{peak} increases. This parameter is the one that correctly describes the azimuthal behaviour of the plasmonic resonance. This is due to the fact that the parameter ΔT takes into account how challenging is the SPR detection when ϕ_{peak} approaches 0°. The FOM_T parameter for the SPR m=1 ($\sim$1.7 a.u./RIU at its maximum) is higher than the one for the SPR m=-2 ($\sim$0.7 a.u./RIU at its maximum) since the first resonance is better than the second one. The experimental behaviour is well reproduced by the simulated data even if for the SPR m=1 a shift to lower angles of the maximum seems to appear.

From this analysis we can conclude that if a peak starting position is chosen in the 10°<ϕ_{peak}<20° interval $|S_\phi|$ is higher than 500 deg /RIU and the parameter FOM_T has already reached at least the 50 % of its maximum value. Obviously the SPR order has to be chosen on the base of the experimental needs e.g. if the functionalization process is expected to increase (decrease) the SPR coupling momentum then m=1 (m=-2) must be prefer since in this case the azimuthal angle resonance shifts to lower values, increasing in this way the method sensitivity.

We suspect that FOM_T is the most correct parameter to apply in the study of the plasmonic resonance sensitivity when it is enhanced by exploiting a parabolic shape resonance. Nevertheless more studies need to be done in order to confirm this.

The resolution of this method depends on the accuracy of the bench azimuthal angle positioning. In our case, it is related to the motorized rotation stage, being 0.01°. Considering this value, we obtain a minimum resolution of 5×10^{-6} RIU, which is only fifty times larger than the lowest reported resolution, i.e., 10^{-7} RIU [25].

4.4   Detection of Alkanethiols Self Assembled Monolayers

In this section we will see how the same azimuthal method, applied for sensing different η_d values, can be adopted for sensing different Self Assembly Monolayer (SAM) adsorbed onto the metallic grating surface. These SAMs are dielectric layers with the same refractive index η_d=1.45 but with a different thickness. By using them we will evaluate the sensitivity of the azimuthal method respect to h_{func}. We will measure this sensitivity considering both air and water as the dielectric medium. In air we will sense the azimuthal shift produced by SAM created by different alkanethiols molecules. In water we will monitor the adsorption onto the grating surface of the 6-mercapto-1-hexanol molecules taking advantage of our microfluidic setup.

4.4.1   Functionalization protocols

To create different type of SAM onto the grating surface we used five different types of molecules. For the air sensitivity test we used alkanethiols molecules with different number of methylene groups in their chain. These molecules are known in literature to form SAM with different thickness [20], [82], [91], [101].This affect the SPP coupling constant since the thicker is the SAM the greater is the SPP coupling momentum.

In particular we dipped five different grating samples into 1 mM ethanol solution of exanethiols (C6), octanethiols (C8), dodecanethiols (C12), and octadecanethiols (C18). The chemical formula of these molecule is CN = $CH_3(CH_2)_{N-1}SH$, where N is the number of carbon atoms in their chain. The thiol group S-H, known as head of the molecule, is the one that allows the link with the metal layer losing its hydrogen atom and becoming an S-Ag group. The CH_3 is the methyl terminal group which is the one in contact with the buffer medium; $(CH_2)_{N-1}$ are the methylene groups contained in the chain as schematically reported in figure 4.19.
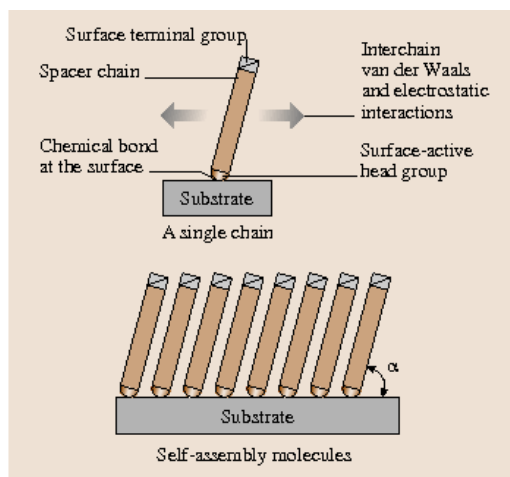

Figure 4.19 Schematic of a SAM [102]

In order to test the sensibility in water we use another molecule: the 6-mercapto-1-hexanol or MCH. Its chemical formulae is $SH(CH_2)_5CH_2OH$. Again its head is a thiol and the tail is a primary alcohol group. In order to functionalize the surface we used the MCH diluted in10 mM solution of milli-q water.

We will refer to the surface without functionalization as bare condition.

4.4.2 Incident angle sensitivity

We start our evaluation of the SAM by measuring the shift of the transmittance peak as a function of the light incident angle due to the C12 surface functionalization.
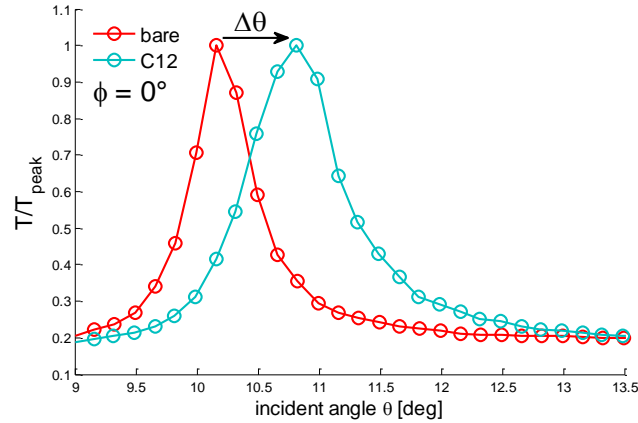

Figure 4.20 T_{tot}/T_{peak} **as a function of** θ **measured for the bare grating (red) and C12 (cyan) surface condition.**

In figure 4.20 we report the grating transmittance normalized at the peak value as a function of θ for the bare grating condition and for the C12 functionalized grating. As we can see a shift of the peak towards higher incident angles is measured and its value is 0.6°, which is consistent with the increasing of the SPP coupling momentum introduced by the functionalization.

4.4.3 Azimuthal sensitivity

In the previous section We proved the correct functionalization behaviour measured as a function of θ, now we will focus onto the azimuthal sensing method [91].
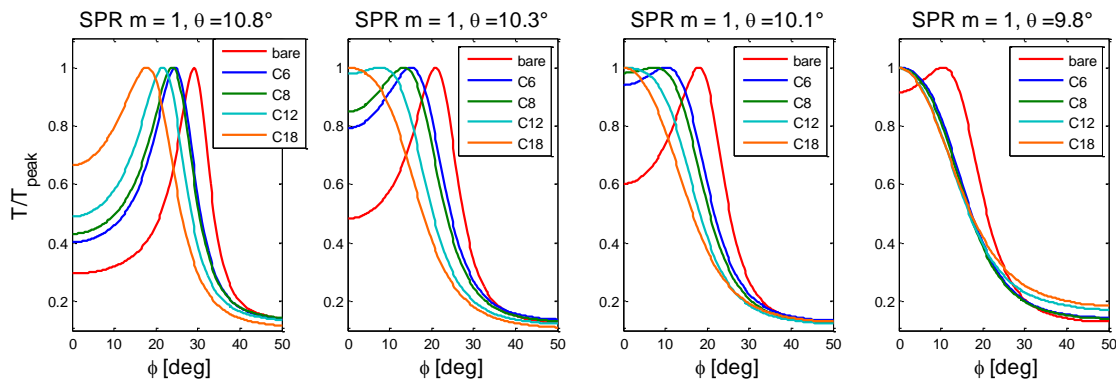

Figure 4.21 T_{tot}/T_{peak} **as a function of** ϕ **measured for the five different conditions of the surface for four different incident angles.**

In figure 4.21 we report the T_{tot} normalized at the peak transmittance as a function of ϕ measured for four different θ and exploiting the SPR $m=1$. Only the $\phi>0°$ part of the curves is reported since they are symmetric respect to $\phi= 0°$. The curves reported are obtained taking the media of five different grating samples measured for each grating condition. The bare condition is the one with no adsorbed molecules on the surface and it coincide with the grating immersed in pure ethanol nevertheless its peaks are the same ones of the air exposed grating.

As we already seen for glycerol/water solution case, the incident angle allows us to change the azimuthal shift between the different conditions. As we can see, for θ= 10.8° an azimuthal peak $\phi \neq 0°$ can be detected for all the five different conditions, while, for θ= 10.3°, only an azimuthal peak at ϕ=0° can be seen for the C18 condition. Taking this particular case the shift between the C12 condition and the C18 goes from 3.88° for θ= 10.8° to 7.55° for θ = 10.3° doubling its value. Similar considerations can be performed for θ= 10.1° where the C12 condition produces a single peak, and for θ= 9.8° where the C8 and C6 azimuthal peaks are merged at ϕ=0°.

The azimuthal peak position for the four different incident angles and for all the five conditions measured are reported in figure 4.23a. It is obvious that when two functionalization conditions have one single peak at ϕ=0° it is impossible to distinguish them by this azimuthal method.

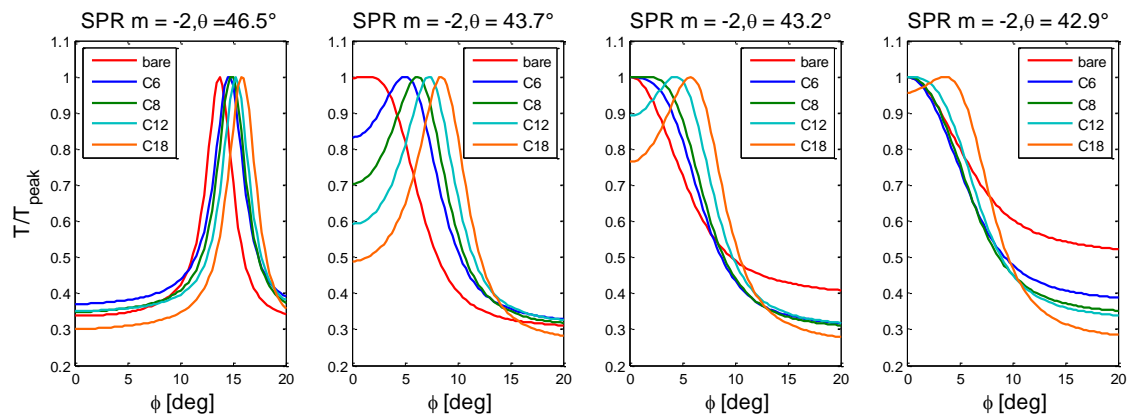We perform the same experiment taking into consideration the m=-2 SPR condition.

Figure 4.22 T_{tot}/T_{peak} as a function of ϕ measured for the five different conditions of the surface for four different incident angles.

In figure 4.22 we report the T_{tot} normalized at the peak transmittance as a function of ϕ measured for four different θ and for the m=-2 SPR. Only the ϕ>0° part of the curves is reported since they are symmetry respect to ϕ= 0°.

Also in this case the figure 4.22 well shows how different θ affects the shift between the conditions. For θ=46.5° all the surface conditions have an azimuthal peak ϕ > 0°, meanwhile for θ = 43.7° the bare conditions shows a peak slightly above ϕ=0°. In this case the shift between the C6 and bare condition is amplified from 0.98° to 3.99° by using the bare optimized incident angle. Decreasing again the incident angle also the C6 and the C12 conditions has only a maximum at ϕ = 0°. The azimuthal peak position and the incident angle for all the five conditions measured are reported in figure 4.23b.
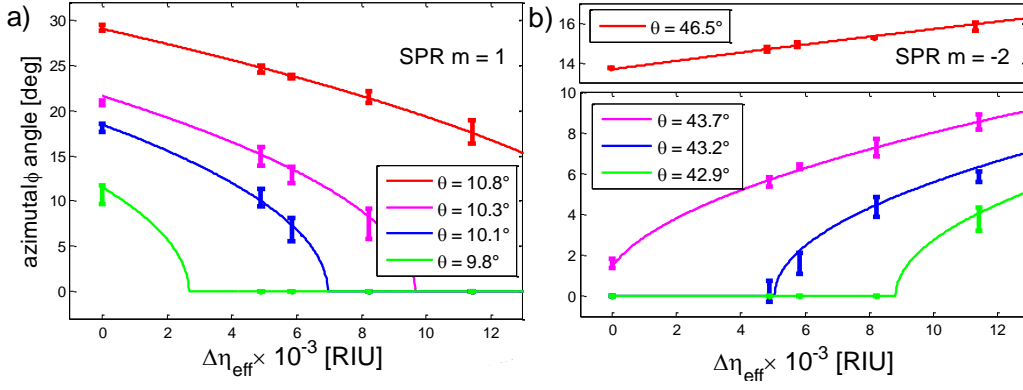
Figure 4.23 Comparison between experimental data (points with error bars) and Vector Model simulations (solid lines) for the peak azimuthal angles as a function of the refractive effective index variation. Values of $\Delta\eta_{eff}$ =(0, 4.9,5.8,8.2,11.4)$\times 10^{-3}$ correspond to the different surface grating conditions. (a) SPR order m=1; (b)SPR m=-2.

In Figure 4.23a and 4.23b we show the azimuthal angle position of the SPR, for various incident angles, as a function of the effective refractive index variations $\Delta\eta_{eff}$ for $m = 1$ and $m = -2$, respectively. The continuous lines correspond to the VM simulation results, while the experimental points are reported with their error bars for each grating condition. The parameter $\Delta\eta_{eff}$ only affects the SPP coupling constant modifying eq. 1.24 into:

$$k_{spp} = k_0 \sqrt{\frac{\left(1 + \Delta\eta_{eff}\right)^2 \varepsilon_m}{\left(1 + \Delta\eta_{eff}\right)^2 + \varepsilon_m}} \tag{4.3}$$

$\Delta\eta_{eff}$ takes into account the modifications introduced by the surface functionalization on the SPR behaviour. Hence the different surface conditions are represented in the x–axis by the different values of $\Delta\eta_{eff}$. For reference, $\Delta\eta_{eff}$ is set to 0 RIU for the bare grating, while it was calculated for the other conditions by using the effective medium approximation model as previously illustrated in eq. 3.5 and in the following one.

$$\eta_{eff} = \eta_d + \frac{2h_{func}}{d_z}(\eta_{func} - \eta_d) \tag{4.4}$$

To perform the calculations we used 0.6 nm, 0.9 nm, 1.5 nm, and 2.2 nm as the thickness values h_{func} for the four different SAMs and η_{func}=1.45 RIU; these values are similar to the one reported in [82]. For the plasmon penetration length d_z we used 160 nm. It is evident that the sensitivity parameter is defined in this case as $S_\phi = \partial\phi/\partial\eta_{eff}$ and corresponds to the slope of these curves. Its experimental values as a function of θ are shown in table 4.3. Considering now figure 4.23a for $m = 1$, we see that the curves slope is always negative and tends to diverge as ϕ approaches 0°. In the same way we can notice that the sensitivity for $m = -2$ is always positive and diverges for $\phi = 0°$ as already seen for the measurements performed by using the glycerol/water solutions.

	SPR m = 1		SPR m = -2
$\theta\ [deg]$	$S_\phi\ [deg]/[RIU]$; C6-Bare	$\theta\ [deg]$	$S_\phi\ [deg]/[RIU]$; C18-C12
10.8	-930	46.5	180
10.3	-1220	43.7	390
10.1	-1570	43.2	460
9.8	-2180	42.9	1180

Table 4.3 Sensitivity measured at different incident angles.

In table 4.3 we report the experimental sensitivity values calculated by using the surface condition pairs that allow the sensitivity evaluation for each incident angle tested. These pairs correspond to the C6 and the bare condition for m = 1, and to the C18 and the C12 conditions for m = −2. A clear sensitivity enhancement of a factor 2.4 is reached for m = 1, while it grows up to 6.5 for m = −2 SPR. The sensitivity reaches values up to 2180 deg/RIU, and 1180 deg/RIU in the two cases, being twenty times higher than the 80 deg/RIU evaluated using the incident angle shift reported in figure 4.20, which is a noticeable improvement.

Regarding the sensitivity in water we measured the kinetic adsorption of the MCH molecules onto the silver metal layer.
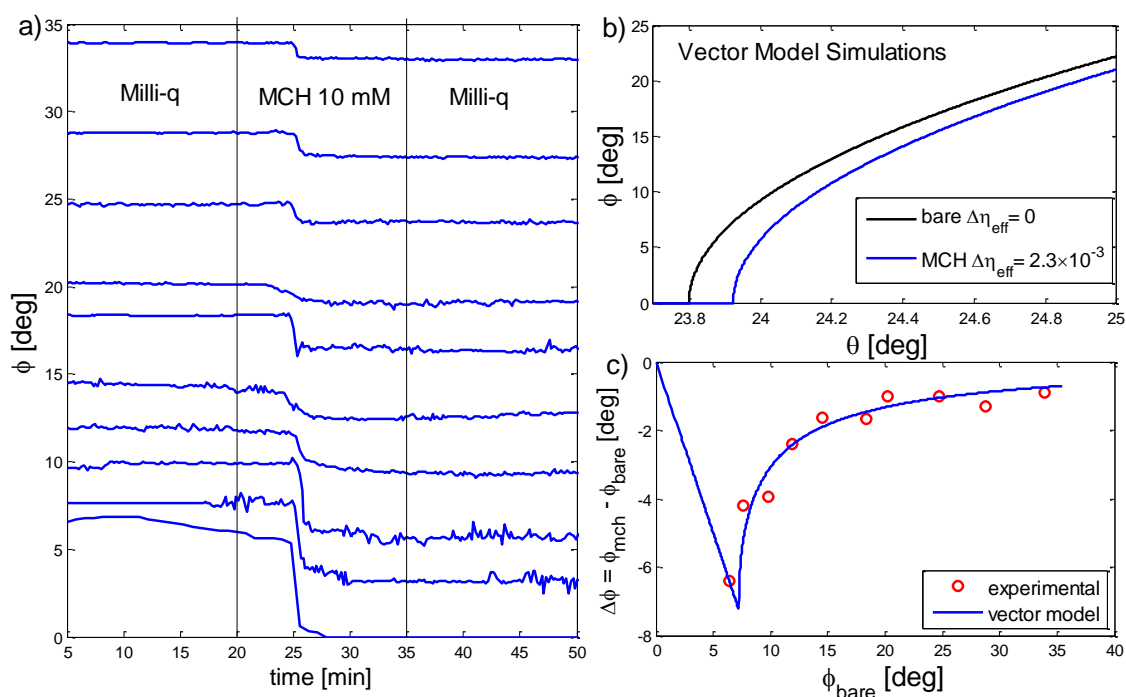

Figure 4.24 (a) Azimuthal peak as a function of the time. (b) Vector model simulation for the two measured surface. (c) Azimuthal angle variations $\Delta\phi$ as a function of the initial peak condition ϕ_{bare}

In figure 4.24a we report the azimuthal peak as a function of the time. For the first 20 minutes we fluxed milli-q water inside the microfluidic cell. Then we changed the solution with the 10 mM MCH one and we waited 15 minutes, then we fluxed again milli-q water. All the process were performed having a fixed flux of 50 µL/min. After the introduction of the MCH solution the azimuthal peak position dropped. This is due to the fact that the molecules present in the solutions have quickly formed a SAM on the silver surface. When we inserted again the milli-q water the ϕ angle did not change again confirming that the decrease of the resonance azimuthal

position was due to the SAM formation rather than a change of the MCH refractive index solution.

In figure 4.19b we report the two azimuthal resonances one for the bare grating condition and one for the MCH grating condition calculated by using a $\Delta\eta_{eff}$= 2.3 x 10^{-3} RIU. In figure 4.19c we report the $\Delta\phi = \phi_{MCH} - \phi_{Bare}$ plotted as a function of the ϕ_{Bare} condition. The red circles refers to the experimental values and can be calculated by measuring the height of the azimuthal steps reported in figure 4.19a while the continuous line refer to the VM calculations that can be retrieved by the curves reported in figure 4.19b.

Also in this case we can see a good agreement between the experimental points and the vector model predicted behaviour. As usual we also notice that $\Delta\phi$ increases as ϕ_{Bare} approaches to 6°. For ϕ_{Bare} <6° the parameter $\Delta\phi$ decreases because the functionalization condition always produces a peak at ϕ=0°.

4.5 Detection of an antibody layer

In the previous section we illustrated how to implement an azimuthal sensing method to evaluate both the change in the buffer refractive index (η_d) and in the SAM formation. Here we want to apply this method to detect the surface variations induced by two subsequent functionalization processes. The first one will produce a cross link SAM by using a carboxymethyl-polyethylene glycol-thiol (PEG). This SAM will exposed a carboxylic group that will be modified in order to immobilized an antibody layer exploiting the ammine groups available on the antibody surface. We will study how the concentration of the PEG and the presence of the antibody will affect the resonance both in the Kretschmann and grating configurations.

4.5.1 Functionalization protocols

In order to perform this experiment we used a drop casting method. The drops (30 µL) were applied on our device by means of a socket (Grace Bio-Labs ProPlate® microarray system, 64). The carboxymethyl-PEG-Thiol with a molecular weight of 3400 Dalton were purchased by (laysanBio). We used N-(3-Dimethylaminopropyl)-N'-ethylcarbodiimide (EDC) and sulfo-N-Hydroxysuccinimide (s-NHS) in MES buffer (sigma Aldrich) in order to activate the carboxylic group of the PEG and link it to an ammine group of the antibody anti (E. Coli) (Virostat).

For the antibodies immobilization, the surface was immersed in a 1 mM PEG/milli-q solution overnight and then rinsed with milli-qwater and dried under nitrogen flux. The PEG carboxylic group was activated through EDC and sulfo-NHS 5 mM each in MES buffer pH 6 for 15 minutes (MES buffer: 0.1M 2-(N-morpholino) ethanesulfonic acid (MES), 0.5M NaCl).After the activation the surface were again rinsed with milli-q water and dried under nitrogen flux.

The anti E. coli antibody at the concentration of 1 mg/mL is then applied to the surface through a printing buffer: Na_2PO_4 0.1 M, NaCl 0.3 M, Triton X-100 0,01%, pH 7.2. Then surface, with the immobilized antibodies, is rinsed in milli-q water and dried in air.

We functionalized our devices as reported in these schemes of table 4.4:

PEG study		Antibody study	
	Orange spot →PEG 1 mM Yellow spot →PEG 0.1 mM or 0.5 mM Cyan spot →milli-q		Orange spot→PEG 1 mM Yellow spot →PEG + Ab Cyan spot →milli-q

Table 4.4 schematic of the functionalization protocols.

Our standard device is a rectangular array of spots, where only the internal ones were used. For the measurements in Kretschmann configuration we will used a flat surface while for the one in grating configuration we will used the nanostructured surface. We will report different test referring to different devices. For each test the experimental points report the average value of the plasmonic resonance position performed over all the same coloured spots.

4.5.2   Incident angle sensitivity (Kretschmann configuration)

We will start by analysing the signals we obtained in the Kretschmann configuration.
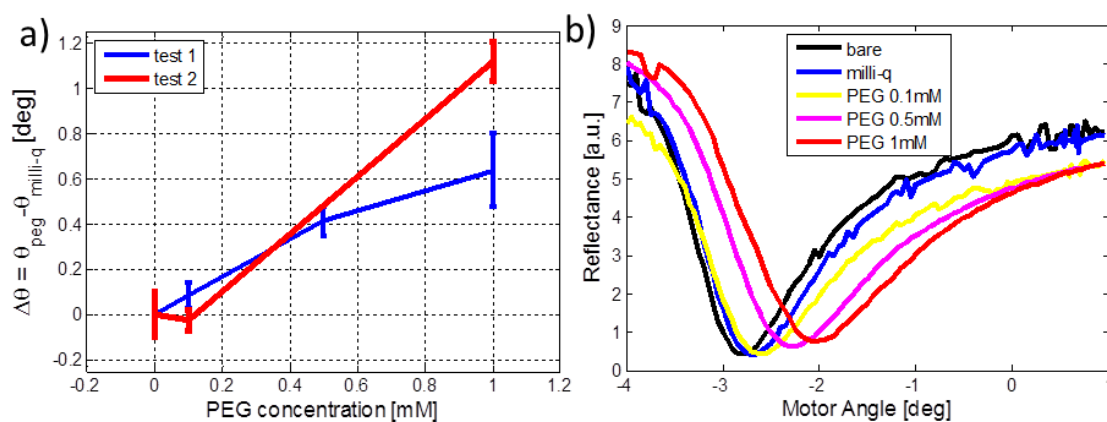

Figure 4.25 (a) Angular shift of the plasmonic resonance respect to the milli-q plotted as a function of the PEG concentration. (b) R_0 as function of the motor angle for the different PEG concentrations

In Figure 4.25a we report the average shift of the SPR from the milli-q condition as a function of the Peg concentrations. In figure 4.25b we report the parameter R_0 as a function of the motorized angle obtained in the first test. As we can notice from figure 4.25a an angular shift up to 1.1° for the SPR minimum position is obtained increasing the PEG concentration. Nevertheless we can also noticed that a huge difference of 0.5° is found between the two test regarding the same 1mM concentrations. In figure 4.25b we can also see how the plasmonic response is affected by the PEG functionalization. Besides the shift of the resonance minimum we notice a slight enhancement of its value. Unfortunately, we cannot increase the PEG concentration to 10 mM because this will damage the silver metal layer. Since we want to create a SAM over the silver layer a 1 mM PEG/milli-q solution will be used in the antibodies immobilization test.

Figure 4.26 (a) Angular shift of the plasmonic resonance respect to the milli-q plotted as a function of the surface condition. (b) R_0 as function of the motor angle for the different surface conditions.

In Figure 4.26a we reported the results obtained for four different functionalization tests. The y-axis reports the shift from the SPR position in the milli-q spot respect to the SPR position measured for the other two surface cases i.e. surface with PEG and antibodies ($\Delta\theta = \theta_{func} - \theta_{milli-q}$); meanwhile the x-axis label represents the spot condition. As we can see always the

110

1mM PEG induced a shift between 0.6° and 1.1° as previously noticed; but not always the antibodies seem to bind with the PEG i.e. the shift between PEG and PEG+antibodies is 0.4° for the first and second tests, while it is almost undetectable for the third and fourth test. In figure 4.22b we report the parameter R_0 as a function of the motorized angle, for the three different surface conditions measured in the second test.

The antibodies sometimes do not produce the expected resonance shift. This behaviour suggests that the antibodies immobilization protocol we used needs to be tuned in order to ensure the results reliability. Another uncertainty factor is the use of silver as metal, in fact it is more instable than gold which is the standard in this type of application.

4.5.3 Azimuthal angle sensitivity

The same experimental test were performed by using the grating configuration.

Figure 4.27(a) Angular shift of the plasmonic resonance respect to the milli-q plotted as a function of the concentration. (b) T_{tot}/T_{peak} as function of ϕ for the different PEG concentrations

In Figure 4.27a we report the average position of the azimuthal SPR respect to the milli-q condition as a function of the PEG concentrations. In figure 4.27b we report the parameter T_{tot} normalized at the peak transmittance as a function of the azimuthal angle for the different PEG concentrations, as obtained in the first test. A noticeable shift of the transmittance maximum is registered as a function of the PEG concentration. As we can notice from figure 4.27a, an angular shift up to 5° of the SPR maximum position is obtained increasing the PEG concentration. Since the metal layer we used is silver, it is not possible to further increase the PEG concentration up to 10 mM; for this reason in the next test we will used the 1mM PEG/milli-q solution in order to form the initial SAM.

In Figure 4.28a we report the results obtained for four different functionalization tests. As in the previous case, the y-axis reports the difference between the average functionalized SPR position and the milli-q, meanwhile the x-axis labels represent the condition of the spot. As we can see the 1mM PEG induced a shift between 3.5° and 5°. Also in this case, not always the antibodies seem to bind with the PEG layer as we can see for the test 3. The shifts between PEG and PEG+antibody reaches 3° for the second test while it is almost 1° for the first and fourth test. Regarding the third test we cannot detect a clear shift induced by the antibodies. In figure 4.28b

we report the parameter R_0 as a function of the azimuthal angle, for the three different grating surface conditions measured in the second test.
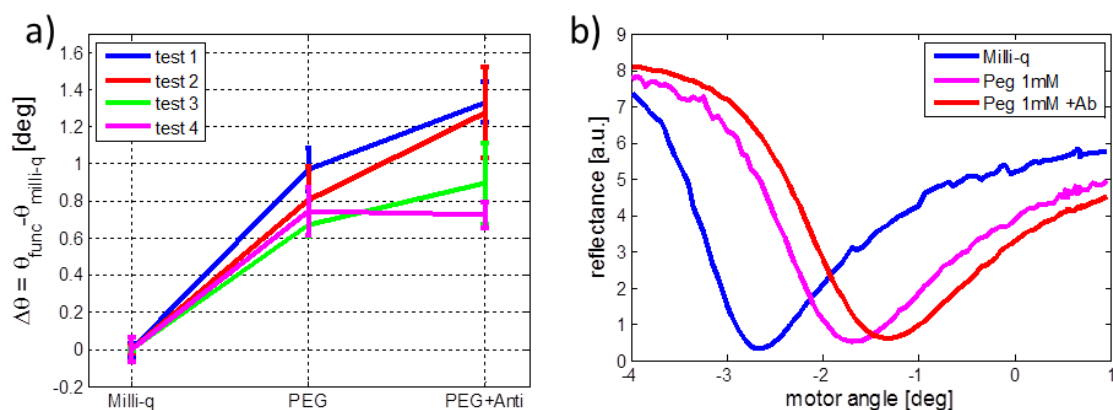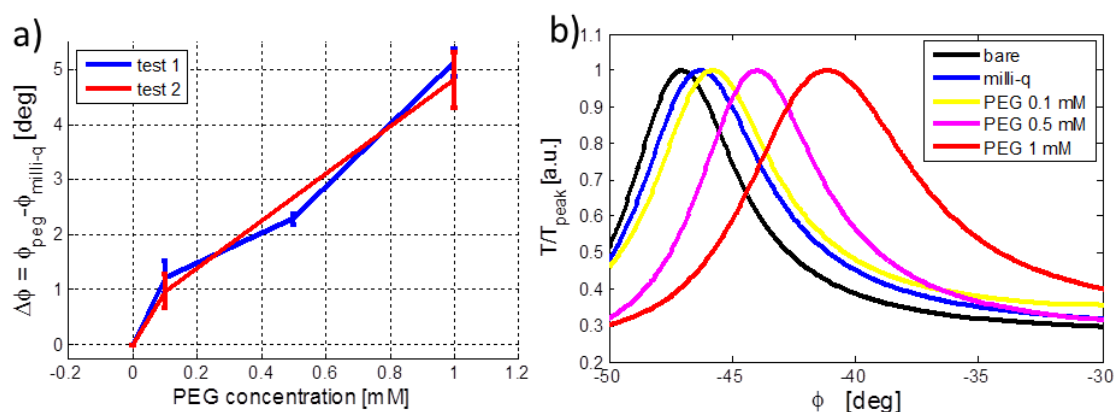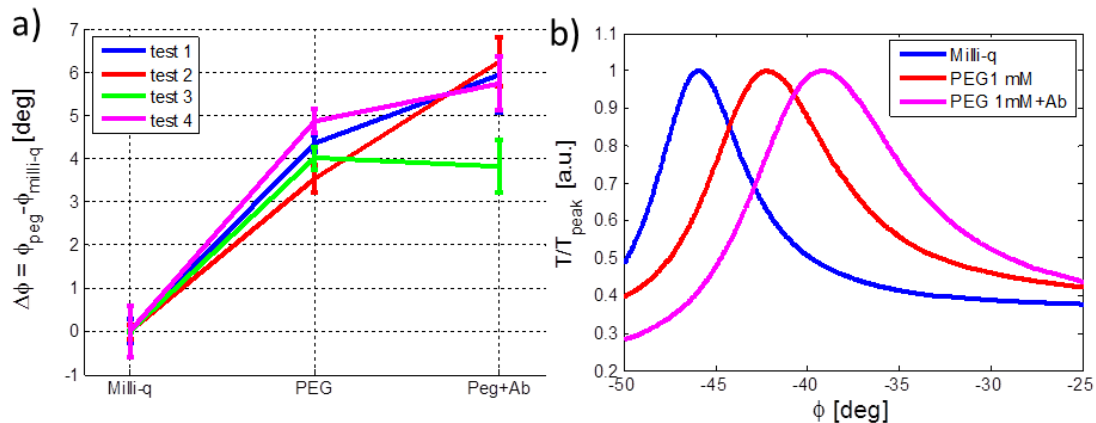

Figure 4.28(a) Angular shift of the plasmonic resonance respect to the milli-q plotted as a function of the surface condition. (b) R_0 T_{tot}/T_{peak} as a function of ϕ for the different surface conditions.

In the following table we summarized the shift obtained between the milli-q treated spots and the ones with the PEG and antibodies both for the Kretschmann and the grating configuration.

	Kretschmann $\Delta\theta_K$[deg]	Grating $\Delta\phi_G$[deg]	Ratio $\Delta\phi_G/\Delta\theta_K$
$\left\|SPR_{PEG} - SPR_{milli-q}\right\|$	$0.6 \div 1.1$	$3.5 \div 5$	$4.5 \div 5.8$
$\left\|SPR_{Ab} - SPR_{milli-q}\right\|$	$1 \div 1.5$	$5 \div 6.5$	$4.3 \div 5.0$

Table 4.5 Comparison between the shift variations found in Kretschmann and Grating configuration and the ration of their shift.

As we can see from table 4.5 the ratio of the shifts calculated by using the two configuration is between 4.3 and 5.5. This is consistent with our simulation since the sensitivity of the Kretschmann configuration is 54 deg/RIU (see table 3.8) while the sensitivity for the azimuthal configuration having an initial peak at 48° is almost 240 deg/RIU (see figure 4.16). The ratio between these two sensitivities is 4.4 which is in the range of the experimental one. Hence similar functionalizations of the two surface types similarly affect the SPP coupling constant. Moreover comparing the two different detection techniques i.e. the Kretschmann one and the azimuthal one we retrieved almost the same information:

- The shifts caused by the PEG functionalization always produces a SPR shift but its value could be subject to huge variations: from 0.6° to 1.1° for the Kretschmann configuration and from 3.5° to 5° for the grating configuration.
- The antibody binding protocol needs to be tuned in order to improve the reliability of the method since in some cases we have not detected any plasmonic resonance variation.

5 Conclusions

In this work we showed how different excitation and detection methods of the Surface Plasmon Resonance phenomenon can be exploited for general sensing purposes. We reached this goal by using both simulations and experimental measurements.

Regarding the simulations, we implemented three different methods: the Rigorous Coupled Wave Analysis, the Chandezon, and the Finite Element method. We compared their results and briefly discussed their properties and applications. Nevertheless another simpler method was analysed: the vector model. By using these tools we were able to compute the intensities of all the light rays diffracted by a periodic, one or two dimensional, nanostructured surface. We also showed how the vector model well reproduces the simulated resonances even if it did not provide qualitative information about their shape.

Applying these simulations methods to the nanostructured surface in conical mounting configuration we noticed that the plasmonic resonance has a fixed parabolic shape and hence there are no great benefits in having a two dimensional periodic surface instead of a one dimensional grating. The result we found adding a further periodicity dimension is that the azimuthal position of the plasmonic vertex ϕ_c can be different from 0°. We have also shown how the relative intensities of the resonances can be changed by adding some features inside the periodic cell.

Through the simulation methods we analyzed what happens in the Kretschmann configuration when a grating is considered. In this case two SPPs seem to be excited. The first one it is related to the metal/air interface and its excitation does not depend on the grating itself since this plasmon is excited exploiting the Kretschmann excitation scheme. The second one is related to the SPP at the metal/polycarbonate interface and it is excited through the grating. This SPP is not affected by the refractive index variation at the silver/air interface, hence it can be used as a reference in a Kretschmann measurements. The presence of these two plasmonic resonances were also experimentally confirmed.

Furthermore we depicted the link between Kretschmann and grating configuration. The rays transmitted by the grating when it is lighted in conical mounting configuration did not carry the same amount of information. We saw that only two rays are significant: the baseline ray and the Kretschmann ray and we generalized this aspect for both the SPR m=1 and m=-2 orders.

The simulations were used also for the evaluation of the bulk sensitivity to the buffer refractive index η_d, and functionalization thickness h_{func} parameters. In particular we analyzed the sensitivity considering as sensing parameters the wavelength, the incident angle, the polarization angle and the azimuthal angle. We also showed that an almost parabolic shape of the plasmonic resonance allows a sensitivity enhancement and we revealed the main common features of this detection method taking the azimuthal case as example.

Experimentally we optimized two optical benches for the detection of the SPR. One for the grating in conical mounting configuration and the other for the Kretschmann configuration. We

implemented the measurement software and performed the calculations for the optimization of the prism position.

Through the conical mounting configuration bench we experimentally studied in detail the azimuthal resonance detection method. Initially we showed its parabolic resonance shape measuring the SPR m=1 and m=-2 both in air and in water. Then we applied the method for enhance and tune the sensitivity of both the η_d, and h_{func} parameters. The first one was investigated by using different glycerol/water solutions meanwhile the second one was investigated by using SAM formed by different molecules. In both cases we reached a maximum angular sensitivity slightly greater than 2000 deg/RIU which is a state of the art value for the plasmoinc resonance based methods. The resolution reaches 5×10^{-6} RIU which is only fifty times larger than the lowest resolution value largely accepted by the scientific community. In addition to the sensitivity we also studied the figure of merit of the method. We found that FOM_T is the best parameter suitable for its description because it takes into account that the closer are the resonances, the higher is the sensitivity, but the hardest is their detection.

Finally we saw how both the Kretschmann and grating configurations report the same information when similar functionalization process is applied on the metallic surface. Nevertheless an higher angular shift was recorded in the grating conical mounting configuration hence the sensitivity this case is higher than the Kretschmann one.

Further research on the SPR excitation needs to be done in order to improve the sensitivity and the detection/excitation method. Key features in this research field, already chased by several groups all over the world, are the development of high throughput, reliable, and portable detection benches as well as the integration of this technique with other ones such as fluorescence and Raman spectroscopy, scanning probe microscopy, and electrochemistry. Another field that could introduce several improvements in the art of the plasmonic sensing could be the development of special metamaterials that allows an engineering of the metallic dielectric constant and the handling of the diffracted rays output angle. Moreover the applications and improvements that can outcome from the plasmonic field are limitless and could have a huge impact on the everyday life since the control of the light at the nanoscale seems nowadays to be the building block for the next technological revolution.

6 Acknowledgements

I would like to thank everyone that helped me through this PhD experience, especially my supervisor, Prof. Alessandro Paccagnella and my colleagues Alessandro De Toni, Elisabetta Pasqualotto, Giulio Rosati, and Matteo Scaramuzza and the Master thesis students Alessandro Zanuoli, Federico Carlesso and Silvia Guggia.

Moreover I acknowledge Prof. Nikolay Zheludev and Fedotov Vassili for the fruitful period I spent with their group at the Optoelectronic Centre of the Southampton university. The Veneto Nanotech group headed by Erica Cretaio for their precious contribution on the implementation of the functionalization processes, the Luxor Laboratories headed by Maria Guglielmina Pelizzo for the access to the Kretschmann configuration bench.

I cannot forget my parents and all my family for the support they gave me and also all my friends, the old ones, from the mountains, and the new ones of the Padova Rugby 555.

And finally I would like to thank Alessandra for always share with me the beautiful and sad moments.

Thank you all...

7 Bibliography

[1]   R. W. Wood, "A suspected case of the Electrical Resonance of Minute Metal Particles for Light-waves. A New Type of Absorption," *Proc. Phys. Soc. London*, vol. 18, no. 1, pp. 166–182, Mar. 1902.

[2]   U. FANO, "The Theory of Anomalous Diffraction Gratings and of Quasi-Stationary Waves on Metallic Surfaces (Sommerfeld's Waves)," *J. Opt. Soc. Am.*, vol. 31, no. 3, p. 213, Mar. 1941.

[3]   A. Otto, "Excitation of nonradiative surface plasma waves in silver by the method of frustrated total reflection," *Zeitschrift für Phys.*, vol. 216, no. 4, pp. 398–410, Aug. 1968.

[4]   E. Kretschmann and H. Raether, "Radiative Decay of Non Radiative Surface Plasmons Excited by Light," *Zeitschrift für Naturforsch.*, vol. 23a, pp. 2135–2136, 1968.

[5]   D. Hornauer, H. Kapitza, and H. Raether, "The dispersion relation of surface plasmons on rough surfaces," *J. Phys. D. Appl. Phys.*, vol. 7, no. 9, pp. L100–L102, Jun. 1974.

[6]   J. G. Gordon and J. D. Swalen, "The effect of thin organic films on the surface plasma resonance on gold," *Opt. Commun.*, vol. 22, no. 3, pp. 374–376, Sep. 1977.

[7]   B. Liedberg, C. Nylander, and I. Lunström, "Surface plasmon resonance for gas detection and biosensing," *Sensors and Actuators*, vol. 4, pp. 299–304, 1983.

[8]   B. Liedberg, C. Nylander, and I. Lundström, "Biosensing with surface plasmon resonance — how it all started," *Biosens. Bioelectron.*, vol. 10, no. 8, pp. i–ix, Jan. 1995.

[9]   J. Homola, S. S. Yee, and G. Gauglitz, "Surface plasmon resonance sensors: review," *Sensors Actuators B Chem.*, vol. 54, no. 1–2, pp. 3–15, 1999.

[10]   X. D. Hoa, a G. Kirk, and M. Tabrizian, "Towards integrated and sensitive surface plasmon resonance biosensors: a review of recent progress.," *Biosens. Bioelectron.*, vol. 23, no. 2, pp. 151–60, Sep. 2007.

[11]   K. S. Phillips and Q. Cheng, "Recent advances in surface plasmon resonance based techniques for bioanalysis," in *Analytical and Bioanalytical Chemistry*, 2007, vol. 387, pp. 1831–1840.

[12]   J. Homola, "Surface plasmon resonance sensors for detection of chemical and biological species.," *Chem. Rev.*, vol. 108, no. 2, pp. 462–93, Feb. 2008.

[13]   S. Scarano, M. Mascini, A. P. F. Turner, and M. Minunni, "Surface plasmon resonance imaging for affinity-based biosensors.," *Biosens. Bioelectron.*, vol. 25, pp. 957–966, 2010.

[14]   I. Lundström, "From a Laboratory Exercise for Students to a Pioneering Biosensing Technology," *Plasmonics*, vol. 1, no. 11, 2014.

[15]   S. A. Maier, *Plasmonics: Fundamentals and applications*. 2007, pp. 1–223.

[16] J. Homola, *Surface Plasmon Resonance Based Sensors*. 2006.

[17] R. B. M. Schasfoort and A. J. Tudos, *Handbook of surface plasmon resonance*, vol. 240. 2008, p. xxi, 403 p.

[18] A. P. F. Turner, "Biosensors: sense and sensibility.," *Chem. Soc. Rev.*, vol. 42, pp. 3184–96, 2013.

[19] U. Jönsson, L. Fägerstam, B. Ivarsson, B. Johnsson, R. Karlsson, K. Lundh, S. Löfås, B. Persson, H. Roos, and I. Rönnberg, "Real-time biospecific interaction analysis using surface plasmon resonance and a sensor chip technology.," *Biotechniques*, vol. 11, pp. 620–627, 1991.

[20] L. Jung, C. Campbell, and T. Chinowsky, "Quantitative interpretation of the response of surface plasmon resonance sensors to adsorbed films," *Langmuir*, vol. 7463, no. 17, pp. 5636–5648, 1998.

[21] E. J. Zeman and G. C. Schatz, "An accurate electromagnetic theory study of surface enhancement factors for silver, gold, copper, lithium, sodium, aluminum, gallium, indium, zinc, and cadmium," *J. Phys. Chem.*, vol. 91, no. 3, pp. 634–643, Jan. 1987.

[22] B. D. Gupta and R. K. Verma, "Surface Plasmon Resonance-Based Fiber Optic Sensors: Principle, Probe Designs, and Some Applications," *J. Sensors*, vol. 2009, pp. 1–12, 2009.

[23] Y. Fu and X. Zhou, "Plasmonic Lenses: A Review," *Plasmonics*, vol. 5, no. 3, pp. 287–310, Jun. 2010.

[24] H. Kim, J. Park, S.-W. Cho, S.-Y. Lee, M. Kang, and B. Lee, "Synthesis and dynamic switching of surface plasmon vortices with plasmonic vortex lens.," *Nano Lett.*, vol. 10, no. 2, pp. 529–36, Feb. 2010.

[25] M. Piliarik and J. Homola, "Surface plasmon resonance (SPR) sensors: approaching their limits?," *Opt. Express*, vol. 17, no. 19, pp. 16505–16517, 2009.

[26] N. J. Tao, S. Boussaad, W. L. Huang, R. a. Arechabaleta, and J. D'Agnese, "High resolution surface plasmon resonance spectroscopy," *Rev. Sci. Instrum.*, vol. 70, no. 12, p. 4656, 1999.

[27] R. Slavík and J. Homola, "Ultrahigh resolution long range surface plasmon-based sensor," *Sensors Actuators B Chem.*, vol. 123, no. 1, pp. 10–12, Apr. 2007.

[28] G. Ruffato and F. Romanato, "Grating-coupled surface plasmon resonance in conical mounting with polarization modulation," *Opt. Lett.*, vol. 37, no. 13, p. 2718, 2012.

[29] G. Granet and L. Li, "Convincingly converged results for highly conducting periodically perforated thin films with square symmetry," *J. Opt. A Pure Appl. Opt.*, vol. 8, no. 6, pp. 546–549, Jun. 2006.

[30] S. Y. Wu, H. P. Ho, W. C. Law, C. Lin, and S. K. Kong, "Highly sensitive differential phase-sensitive surface plasmon resonance biosensor based on the Mach-Zehnder configuration.," *Opt. Lett.*, vol. 29, pp. 2378–2380, 2004.

[31]   H. Bai, R. Wang, B. Hargis, H. Lu, and Y. Li, "A SPR aptasensor for detection of avian influenza virus H5N1.," *Sensors (Basel).*, vol. 12, no. 9, pp. 12506–18, Jan. 2012.

[32]   R. L. Caygill, G. E. Blair, and P. a Millner, "A review on viral biosensors to detect human pathogens.," *Anal. Chim. Acta*, vol. 681, no. 1–2, pp. 8–15, Nov. 2010.

[33]   Z. Altintas, Y. Uludag, Y. Gurbuz, and I. E. Tothill, "Surface plasmon resonance based immunosensor for the detection of the cancer biomarker carcinoembryonic antigen.," *Talanta*, vol. 86, pp. 377–83, Oct. 2011.

[34]   Z. Altintas and I. Tothill, "Biomarkers and biosensors for the early diagnosis of lung cancer," *Sensors Actuators B Chem.*, vol. 188, pp. 988–998, Nov. 2013.

[35]   J. Wei, Y. Mu, D. Song, X. Fang, X. Liu, L. Bu, H. Zhang, G. Zhang, J. Ding, W. Wang, Q. Jin, and G. Luo, "A novel sandwich immunosensing method for measuring cardiac troponin I in sera," *Anal. Biochem.*, vol. 321, no. 2, pp. 209–216, Oct. 2003.

[36]   Y. Yanase, T. Hiragun, T. Yanase, T. Kawaguchi, K. Ishii, and M. Hide, "Application of SPR Imaging Sensors for detection of individua living cell reaction and clinical diagnosisof Type I allergy," *Allergol. Int.*, vol. 62, no. 2, pp. 163–9, Jun. 2013.

[37]   K. Hegnerová, M. Bocková, H. Vaisocherová, Z. Krištofiková, J. Říčný, D. Řípová, and J. Homola, "Surface plasmon resonance biosensors for detection of Alzheimer disease biomarker," *Sensors Actuators B Chem.*, vol. 139, no. 1, pp. 69–73, May 2009.

[38]   T. F. McGrath, J. Buijs, a. C. Huet, P. Delahaut, C. T. Elliott, and M. H. Mooney, "Assessment of a multiplexing high throughput immunochemical SPR biosensor in measuring multiple proteins on a single biosensor chip," *Sensors Actuators B Chem.*, vol. 186, pp. 423–430, Sep. 2013.

[39]   E. Mauriz, a Calle, J. J. Manclús, a Montoya, and L. M. Lechuga, "Multi-analyte SPR immunoassays for environmental biosensing of pesticides.," *Anal. Bioanal. Chem.*, vol. 387, no. 4, pp. 1449–58, Feb. 2007.

[40]   R. Yatabe, T. Onodera, and K. Toko, "Fabrication of an SPR sensor surface with antifouling properties for highly sensitive detection of 2,4,6-trinitrotoluene using surface-initiated atom transfer polymerization." *Sensors (Basel).*, vol. 13, no. 7, pp. 9294–304, Jan. 2013.

[41]   H. Bao, T. Wei, X. Li, Z. Zhao, H. Cui, and P. Zhang, "Detection of TNT by a molecularly imprinted polymer film-based surface plasmon resonance sensor," *Chinese Sci. Bull.*, vol. 57, no. 17, pp. 2102–2105, Apr. 2012.

[42]   S. Wang, E. S. Forzani, and N. Tao, "Detection of heavy metal ions in water by high-resolution surface plasmon resonance spectroscopy combined with anodic stripping voltammetry.," *Anal. Chem.*, vol. 79, no. 12, pp. 4427–32, Jun. 2007.

[43]   J. D. Wright, J. V. Oliver, R. J. M. Nolte, S. J. Holder, N. a. J. M. Sommerdijk, and P. I. Nikitin, "The detection of phenols in water using a surface plasmon resonance system with specific receptors," *Sensors Actuators B Chem.*, vol. 51, no. 1–3, pp. 305–310, Aug. 1998.

[44] M. Shimomura, Y. Nomura, W. Zhang, M. Sakino, K.-H. Lee, K. Ikebukuro, and I. Karube, "Simple and rapid detection method using surface plasmon resonance for dioxins, polychlorinated biphenylx and atrazine," *Anal. Chim. Acta*, vol. 434, no. 2, pp. 223–230, May 2001.

[45] D. Zhang, Y. Yan, Q. Li, T. Yu, W. Cheng, L. Wang, H. Ju, and S. Ding, "Label-free and high-sensitive detection of Salmonella using a surface plasmon resonance DNA-based biosensor.," *J. Biotechnol.*, vol. 160, no. 3–4, pp. 123–8, Aug. 2012.

[46] V. Hodnik and G. Anderluh, "Toxin detection by surface plasmon resonance.," *Sensors (Basel).*, vol. 9, no. 3, pp. 1339–54, Jan. 2009.

[47] J. Keegan, R. O'Kennedy, S. Crooks, C. Elliott, D. Brandon, and M. Danaher, "Detection of benzimidazole carbamates and amino metabolites in liver by surface plasmon resonance-biosensor.," *Anal. Chim. Acta*, vol. 700, no. 1–2, pp. 41–8, Aug. 2011.

[48] S. Rebe Raz, M. G. E. G. Bremer, W. Haasnoot, and W. Norde, "Label-free and multiplex detection of antibiotic residues in milk using imaging surface plasmon resonance-based immunosensor.," *Anal. Chem.*, vol. 81, no. 18, pp. 7743–9, Sep. 2009.

[49] K. Narsaiah, S. N. Jha, R. Bhardwaj, R. Sharma, and R. Kumar, "Optical biosensors for food quality and safety assurance-a review.," *J. Food Sci. Technol.*, vol. 49, no. 4, pp. 383–406, Aug. 2012.

[50] M. Moharam and T. Gaylord, "Rigorous coupled-wave analysis of planar-grating diffraction," *JOSA*, vol. 71, no. 7, 1981.

[51] M. Moharam, E. Grann, D. Pommet, and T. Gaylord, "Formulation for stable and efficient implementation of the rigorous coupled-wave analysis of binary gratings," *JOSA A*, vol. 12, no. 5, p. 1068, 1995.

[52] M. G. Moharam, D. A. Pommet, and E. B. Grann, "Stable implementation of the rigorous coupled-wave analysis for surface-relief gratings : enhanced transmittance matrix approach," vol. 12, no. 5, pp. 1077–1086, 1995.

[53] P. Götz, T. Schuster, K. Frenner, S. Rafler, and W. Osten, "Normal vector method for the RCWA with automated vector field generation.," *Opt. Express*, vol. 16, no. 22, pp. 17295–301, Oct. 2008.

[54] T. Schuster, J. Ruoff, N. Kerwien, S. Rafler, and W. Osten, "Normal vector method for convergence improvement using the RCWA for crossed gratings CONVERGENCE IMPROVEMENT," vol. 24, no. 9, pp. 2880–2890, 2007.

[55] J. Chandezon, M. T. Dupuis, G. Cornet, and D. Maystre, "Multicoated gratings: a differential formalism applicable in the entire optical region," *Journal of the Optical Society of America*, vol. 72. p. 839, 1982.

[56] L. Li, "Multilayer-coated diffraction gratings: differential method of Chandezon et al. revisited," *JOSA A*, vol. 11, no. 11, pp. 2816–2828, 1994.

[57]   L. Li, J. Chandezon, G. Granet, and J. Plumey, "Rigorous and efficient grating-analysis method made easy for optical engineers," *Appl. Opt.*, vol. 38, no. 2, pp. 304–313, 1999.

[58]   L. Li, "New formulation of the Fourier modal method for crossed surface-relief gratings," *J. Opt. Soc. Am. A*, vol. 14, no. 10, p. 2758, Oct. 1997.

[59]   G. Granet, "Analysis of diffraction by surface-relief crossed gratings with use of the Chandezon method: application to multilayer crossed gratings," *JOSA A*, vol. 15, no. 5, 1998.

[60]   M. G. Moharam, "Coupled-Wave Analysis Of Two-Dimensional Dielectric Gratings," in *1988 Los Angeles Symposium--O-E/LASE '88*, 1988, pp. 8–11.

[61]   P. Lalanne, "Improved formulation of the coupled-wave method for two-dimensional gratings," *Journal of the Optical Society of America A*, vol. 14. p. 1592, 1997.

[62]   S. Essig and K. Busch, "Generation of adaptive coordinates and their use in the Fourier Modal Method," *Opt. Express*, vol. 18, no. 22, pp. 839–846, 2010.

[63]   Jian-Ming Jin, *The Finite Element Method in Electromagnetics*, II. IEEE, Electrical & Electronics Engr, 2002, p. 780.

[64]   P. Lalanne and G. M. Morris, "Highly improved convergence of the coupled-wave method for TM polarization," *J. Opt. Soc. Am. A*, vol. 13, no. 4, p. 779, Apr. 1996.

[65]   L. Li, "Use of Fourier series in the analysis of discontinuous periodic structures," *JOSA A*, vol. 13, no. 9, pp. 1870–1876, 1996.

[66]   N. van der Aa, "Diffraction grating theory with RCWA or the C method," *Prog. Ind. Math. ECMI 2004*, pp. 1–5, 2006.

[67]   L. Li, J. Chandezon, G. Granet, and J. P. Plumey, "Rigorous and efficient grating-analysis method made easy for optical engineers.," *Appl. Opt.*, vol. 38, pp. 304–313, 1999.

[68]   L. Li and J. Chandezon, "Improvement of the coordinate transformation method for surface-relief gratings with sharp edges," *J. Opt. Soc. Am. A*, vol. 13, no. 11, p. 2247, Nov. 1996.

[69]   J. J. D. Joannopoulos, S. Johnson, J. N. J. Winn, and R. R. D. Meade, *Photonic crystals: molding the flow of light*. 2008, p. 286.

[70]   M. Veith, K. Müller, S. Mittler-Neher, and W. Knoll, "Propagation and deflection of guided modes in planar waveguides via grating rotation," *Appl. Phys. B*, vol. 4, pp. 1–4, 1995.

[71]   D. Kim, "Effect of the azimuthal orientation on the performance of grating-coupled surface-plasmon resonance biosensors," *Appl. Opt.*, 2005.

[72]   F. Romanato, L. Hong, H. Kang, and C. Wong, "Azimuthal dispersion and energy mode condensation of grating-coupled surface plasmon polaritons," *Phys. Rev. B*, vol. 77, no. 24, p. 245435, Jun. 2008.

[73] S. Park, H. Won, G. Lee, S. Song, C. Oh, and P. Kim, "Grating-assisted emission of surface plasmons," *J. Korean Phys. Soc*, vol. 46, no. 2, pp. 492–497, 2005.

[74] M. Perino, E. Pasqualotto, M. Scaramuzza, a. De Toni, and a. Paccagnella, "Characterization of Grating Coupled Surface Plasmon Polaritons Using Diffracted Rays Transmittance," *Plasmonics*, Apr. 2014.

[75] A. D. Rakic, A. B. Djurišic, J. M. Elazar, and M. L. Majewski, "Optical Properties of Metallic Films for Vertical-Cavity Optoelectronic Devices," *Appl. Opt.*, vol. 37, no. 22, p. 5271, Aug. 1998.

[76] U. Schröter and D. Heitmann, "Grating couplers for surface plasmons excited on thin metal films in the Kretschmann-Raether configuration," *Phys. Rev. B*, vol. 60, no. 7, pp. 4992–4999, 1999.

[77] I. R. Hooper and J. R. Sambles, "Surface plasmon polaritons on narrow-ridged short-pitch metal gratings in the conical mount," vol. 20, no. 5, pp. 836–843, 2003.

[78] C. Alleyne, A. Kirk, R. McPhedran, P. Nicorovici, and D. Maystre, "Enhanced SPR sensitivity using periodic metallic structures," *Opt. Lett.*, vol. 15, no. 13, pp. 8163–8169, 2007.

[79] K. Byun, S. Kim, and D. Kim, "Grating-coupled transmission-type surface plasmon resonance sensors based on dielectric and metallic gratings," *Appl. Opt.*, vol. 46, no. 23, pp. 5703–5708, 2007.

[80] S. Park, G. Lee, S. H. Song, C. H. Oh, and P. S. Kim, "Resonant coupling of surface plasmons to radiation modes by use of dielectric gratings.," *Opt. Lett.*, vol. 28, no. 20, pp. 1870–1872, 2003.

[81] J. Yoon, S. H. Song, and J.-H. Kim, "Extraction efficiency of highly confined surface plasmon-polaritons to far-field radiation: an upper limit.," *Opt. Express*, vol. 16, no. 2, pp. 1269–1279, 2008.

[82] B. K. Singh and A. C. Hillier, "Surface Plasmon Resonance Enhanced Transmission of Light through Gold-Coated Diffraction Gratings," vol. 80, no. 10, pp. 3803–3810, 2008.

[83] W.-H. Yeh and A. C. Hillier, "Use of dispersion imaging for grating-coupled surface plasmon resonance sensing of multilayer Langmuir-Blodgett films.," *Anal. Chem.*, vol. 85, no. 8, pp. 4080–6, Apr. 2013.

[84] B. K. Singh and A. C. Hillier, "Surface plasmon resonance imaging of biomolecular interactions on a grating-based sensor array.," *Anal. Chem.*, vol. 78, no. 6, pp. 2009–18, Mar. 2006.

[85] F. Romanato, K. H. Lee, H. K. Kang, G. Ruffato, and C. C. Wong, "Sensitivity enhancement in grating coupled surface plasmon resonance by azimuthal control," *Opt. Lett.*, vol. 17, no. 14, pp. 12145–12154, 2009.

[86] K. H. Lee, F. Romanato, H. K. Kang, and C. C. Wong, "Polarization optimization for a full sensitivity in azimuthal grating coupled surface plasmon resonance," *Sensors Actuators B Chem.*, vol. 148, no. 1, pp. 181–185, Jun. 2010.

[87] A. Meneghello, A. Antognoli, A. Sonato, G. Zacco, G. Ruffato, E. Cretaio, and F. Romanato, "Label-free efficient and accurate detection of Cystic Fibrosis causing mutations using an azimuthally rotated GC-SPR platform," *Anal. Chem.*, vol. 86, pp. 11773–11781, 2014.

[88] A. Sonato, D. Silvestri, G. Ruffato, G. Zacco, F. Romanato, and M. Morpurgo, "Quantitative control of poly(ethylene oxide) surface antifouling and biodetection through azimuthally enhanced grating coupled-surface plasmon resonance sensing," *Appl. Surf. Sci.*, vol. 286, pp. 22–30, Dec. 2013.

[89] G. Ruffato, E. Pasqualotto, a. Sonato, G. Zacco, D. Silvestri, M. Morpurgo, a. De Toni, and F. Romanato, "Implementation and testing of a compact and high-resolution sensing device based on grating-coupled surface plasmon resonance with polarization modulation," *Sensors Actuators B Chem.*, vol. 185, pp. 179–187, Aug. 2013.

[90] E. Pasqualotto, G. Ruffato, a. Sonato, G. Zacco, D. Silvestri, M. Morpurgo, a. De Toni, and F. Romanato, "Plasmonic platforms for innovative surface plasmon resonance configuration with sensing applications," *Microelectron. Eng.*, vol. 111, pp. 348–353, Nov. 2013.

[91] M. Perino, E. Pasqualotto, M. Scaramuzza, a. De Toni, and a. Paccagnella, "Enhancement and control of surface plasmon resonance sensitivity using grating in conical mounting configuration," *Opt. Lett.*, vol. 40, no. 2, p. 221, Jan. 2015.

[92] R. Gordon, D. Sinton, K. L. Kavanagh, and A. G. Brolo, "A new generation of sensors based on extraordinary optical transmission.," *Acc. Chem. Res.*, vol. 41, pp. 1049–1057, 2008.

[93] M. Perino, E. Pasqualotto, a De Toni, D. Garoli, M. Scaramuzza, P. Zilio, T. Ongarello, a Paccagnella, and F. Romanato, "Development of a complete plasmonic grating-based sensor and its application for self-assembled monolayer detection.," *Appl. Opt.*, vol. 53, no. 26, pp. 5969–76, Sep. 2014.

[94] a. Karabchevsky, O. Krasnykov, I. Abdulhalim, B. Hadad, a. Goldner, M. Auslender, and S. Hava, "Metal grating on a substrate nanostructure for sensor applications," *Photonics Nanostructures - Fundam. Appl.*, vol. 7, no. 4, pp. 170–175, Dec. 2009.

[95] D. Cai, Y. Lu, K. Lin, P. Wang, and H. Ming, "Improving the sensitivity of SPR sensors based on gratings by double-dips method (DDM)," *Opt. Express*, vol. 16, no. 19, pp. 14597–14602, 2008.

[96] F. Romanato, K. H. Lee, G. Ruffato, and C. C. Wong, "The role of polarization on surface plasmon polariton excitation on metallic gratings in the conical mounting," *Appl. Phys. Lett.*, vol. 96, no. 11, p. 111103, 2010.

[97] P. Zuppella, E. Pasqualotto, S. Zuccon, F. Gerlin, A. J. Corso, M. Scaramuzza, A. De Toni, A. Paccagnella, and M. G. Pelizzo, "Palladium on plastic substrates for plasmonic devices.," *Sensors (Basel).*, vol. 15, no. 1, pp. 1138–47, Jan. 2015.

[98] P. Qi, Y. Li, and J. Zhong, "Optimized angle scanning method for array sample detection in surface plasmon resonance biosensor," vol. 51, no. 9, pp. 1245–1250, 2012.

[99] B. Turker, H. Guner, S. Ayas, O. O. Ekiz, H. Acar, M. O. Guler, and A. Dâna, "Grating coupler integrated photodiodes for plasmon resonance based sensing.," *Lab Chip*, vol. 11, no. 2, pp. 282–7, Jan. 2011.

[100] D. R. Lide, G. Baysinger, and L. I. Berger, *CRC Handbook of Chemistry and Physics*. 1985.

[101] L. Jung and C. Campbell, "Sticking Probabilities in Adsorption from Liquid Solutions: Alkylthiols on Gold," *Phys. Rev. Lett.*, vol. 84, no. 22, pp. 5164–5167, May 2000.

[102] B. Bhushan, *Handbook Nanotechnology*. Spinger-Verlag Berlin Heidelberg New York, 2003, p. V.

List of abbreviations and acronyms

Ab	Antibodies
ATR	Attenuated Total internal Reflection
C6	exanethiols
C8	octanethiols
C12	dodecanethiols
C18	octadecanethiols
CM	Chandezon Method
DDARM	Double Dip Azimuthal Rotated Method
DDM	Double Dip Method
DO	Optical Density
FEM	Finite Element Method
FOM	Figure Of Merit
FWMH	Full Width Medium Height
LOD	Limit Of Detection
GCSPR	Grating Coupling Surface Plasmon Resonance
MCH	6-mercapto-1-hexanol
PEG	carboxymethyl-PolyEthylene Glycol-thiol
RCWA	Rigorous Coupled Wave Analysis
R_0	Zero Order Reflectance
RIU	Refractive Index Unit
SAM	Self-Assembled Monolayer
SDARM	Single Dip Azimuthal Rotated Method
SPP	Surface Plasmon Polariton
SPR	Surface Plasmon Resonance
TIR	Total Internal Reflection
TE	Transverse Electric
TM	Transverse Magnetic
T_{tot}	Total grating Transmittance
VM	Vector Moedel